IMPACT OF SAHARAN DUST AEROSOLS ON RADIATION AND CLOUDS OVER THE TROPICAL EAST ATLANTIC OCEAN

ABDULLA AL MAMUN

A DISSERTATION SUBMITTED TO THE FACULTY OF GRADUATE STUDIES IN PARTIAL FULFILLMENT OF THE REQUIREMENTS FOR THE DEGREE OF
DOCTOR OF PHILOSOPHY

GRADUATE PROGRAM IN PHYSICS AND ASTRONOMY
YORK UNIVERSITY
TORONTO, ONTARIO

September 2017

Abstract

Aerosols affect the atmospheric processes by interacting with shortwave (SW) and longwave (LW) radiations and also by modifying the cloud microphysics (direct and indirect effects respectively). This study investigates the direct and indirect effects of Saharan dust aerosols, and the subsequent perturbations of the radiation budget and tropical convection by using the Weather Research and Forecasting model coupled with Chemistry module (WRF-Chem). Simulations are conducted for July 1-31, 2010 over two-way nested domains in the tropical East Atlantic Ocean.

Results show that the interactions of dust particles with the SW and LW radiations enhance the heating rates in the atmosphere and primarily affect the upwelling SW radiation at the top of the atmosphere, and downwelling SW and LW radiations at the surface. Dust induced lower level heating increases the stability of the lower troposphere. As a result, convection is inhibited below the dust layers and enhanced in the levels inside and above the dust layers. Dust particles acting as the cloud condensation nuclei (CCN) lead to enhanced condensation and produce numerous cloud droplets with reduced droplet sizes. Consequently, slower collision coalescence among the cloud droplets affects the droplet autoconversion rate and reduces the rain production. However, there is no evidence of the suppression of accumulated precipitation at the surface that would otherwise increase the cloud lifetime.

The net radiative forcing of dust is positive inside the atmosphere, and negative at the surface, and top of the atmosphere. Due to the overall positive radiative feedback from the cloud, the magnitudes of the forcing at surface and top of the atmosphere become weaker in the presence of clouds.

Acknowledgements

It is a great pleasure for me to convey my sincere gratitude to my supervisor Professor Yongsheng Chen for his continuous support and knowledgeable guidance in last 4 years. I would also like to take this opportunity to express my deepest sense of honor to my ex-supervisor Professor John (Jack) C. McConnell, who passed away in July 2013. I am very much grateful to my supervisory committee members Professor Jim Whiteway and Dr. Leiming Zhang for their valuable comments and suggestions throughout my study. Special thanks to Professor Whiteway for ensuring my research funding following the unexpected death of Professor McConnell.

Many thanks to Ms. Marlene Caplan and Professor Tom Kirchner in the Physics and Astronomy graduate program for their helpful advices and various personal initiatives regarding the administrative matters.

I am also grateful to all the members of my research group, especially to Mr. Jianyu Liang for helping me to become familiar with the WRF-Chem model and also providing other technical assistance to perform the simulation experiments. Furthermore, I thank all of my friends especially Mr. Zahidur Rahman and Mr. Syed Islam for their valuable suggestions, encouragements, and sacrifices. At last, I would like to thank my parents and wife for their love, patience, and support over the years.

Table of Contents

Abstract..... ii

Acknowledgements..... iii

Table of Contents..... iv

List of Tables..... vii

List of Figures..... viii

1. Introduction

1.1 Research Background and Motivation..... 1

1.2 Current Understanding of the Dust-Cloud-Radiation Interactions……..... 3

1.2.1 Direct Effect of Dust…….. 4

1.2.2 Indirect Effects of Dust…….. 7

1.2.3 Dust Effects on Convection…… 10

1.3 Dissertation Outline…….. 10

2. Saharan Dust Climatology

2.1 Observation Variables and Datasets..... 12

2.2 Aerosol Climatology over the East Atlantic Ocean..... 16

2.3 Aerosol Characterization over the East Atlantic Ocean…… 21

2.4 Warm and Dry Air Anomalies of the Saharan Air Layer …… 24

2.5 Statistical Analysis of the Climate Data…… 29

2.5.1 Empirical Orthogonal Function (EOF) Analysis……..... 30

2.5.2 Singular Value Decomposition (SVD) Analysis……. 36

3. Numerical Model Description and Validation

3.1 Model Description..... 43

3.2 Model Configuration..... 44

3.2.1 Aerosol Model: MADE-SORGAM Scheme……... 45

3.2.2 Radiation: RRTMG Scheme…… 46

3.2.3 Cloud Microphysics: Morrison Scheme…….. 48

3.3 Model Set-up and Simulation Design……... 49

3.4 Model Validation…….. 54

4. Radiative Effects of the Saharan Dust

4.1 Absorption and Scattering Properties of the Saharan Dust..... 61

4.2 Clear-Sky Radiative Forcing of the Saharan Dust..... 68

4.3 Dust Effects on Atmospheric Heating Rates and Temperature..... 73

4.4 Dust Effects on Surface Heat Fluxes and Cloud Cover……. 77

4.5 Dust Direct Effect with Cloud Feedback…….. 81

5. Saharan Dust Effects on Cloud Microphysics

5.1 Dust vs. Other Aerosols: Results from the Sensitivity Tests…… 85

5.2 Dust Effects on Cloud Microphysics……..... 87

5.3 Dust Effects on Precipitation Properties and the Moisture Budget……. 93

5.4 Dust Effects on the Surface Convergence and Buoyancy…… 99

5.5 Net Dust Radiative Forcing: Direct and Indirect Effects…… 103

6. Conclusion

6.1 Summary …..... 106

6.2 Future Work..... 112

Bibliography..... 113

List of Tables

Table 2.1	Dataset versions and the spatial resolutions of the data from various observation platforms used in this study.	16
Table 2.2	Correlation coefficients (at 95% confidence level) between the expansion coefficients associated with different modes of the coupled SVD decomposition of AOD (left field) and atmospheric temperature (right field) in the first six AIRS retrieval levels.	39
Table 2.3	Same as table 2.2, but the expansion coefficients are associated with the SVD decomposition of AOD (left field) and specific humidity (right field).	41
Table 3.1	Summary of the physical parameterization schemes used in this study.	44
Table 3.2	Details of the WRF-Chem model simulation experiments used in this study.	52
Table 4.1	Radiative forcing of the Atmosphere, Surface, and top of the atmosphere with (All sky) and without the cloud feedback (clear sky).	83
Table 4.2	Domain averaged mean (0Z July 01 to 18Z July 31, 2010; 0-25°N, 20-50°W) changes in atmospheric and surface variables by the Saharan dust aerosols, considering only the dust direct effect.	83
Table 5.1	Spatially and temporally averaged changes in atmospheric and surface variables by the Saharan dust aerosols, considering both dust direct and indirect effects. Results are averaged over 2.5-12°N, 30-40°W and 0Z July 06 -18Z July 13 for the finer resolution runs (I04), and over 0-25°N, 20-50°W and 0Z July 01 - 18Z July 31 for the coarser resolution runs (I36).	101
Table 5.2	Spatially and temporally averaged radiative forcing of the Atmosphere, Surface, and top of the atmosphere with (All sky) and without the cloud feedback (clear sky), considering both dust direct and indirect effects. Radiative forcing are calculated from the radiative fluxes averaged over 2.5-12°N, 30-40°W; 0Z July 06 -18Z July 13 for the finer resolution runs (I04), and over 0-25°N, 20-50°W; 0Z July 01 - 18Z July 31 for the coarser resolution runs (I36).	105

List of Figures

Figure 2.1	Scatter plot showing the comparison of the monthly mean AODs from MODIS-Aqua, MODIS-Terra, MISR-Terra, and CALIOP against the AERONET AOD. Individual points represent the monthly mean AOD measurements at the Cape Verde Island (16.73°N, 22.94°W) during 2003-2012. The Pearson correlation coefficient (*r*) values are shown inside the parentheses.	17
Figure 2.2	June-August AOD climatology (averaged through 2003 to 2012) over the downstream of the Sahara desert from a) MODIS-Aqua, b) MODIS-Terra, c) MISR-Terra, and d) CALIOP. Abscissa and ordinate represent the longitude and latitude respectively. Rectangles indicate the domain chosen for the multiyear dust climatology study and the analysis of the correlations of AOD anomalies with the temperature and humidity anomalies.	18
Figure 2.3	Monthly mean AOD time series for the time period 2003-2012 from the MODIS-Aqua, MODIS-Terra, MISR-Terra, and CALIOP datasets. AOD data are averaged over the study domain (0-25°N, 20-50°W).	18
Figure 2.4	Climatological (2003-2012) mean AOD over the domain (0-25°N, 20-50°W) for individual calendar months from the MODIS-Aqua, MODIS-Terra, MISR-Terra, and CALIOP datasets, and their mean.	20
Figure 2.5	Inter-annual variability of the monthly mean AOD anomalies in July (relative to the climatological July mean over 2003-2012) retrieved from the MODIS-Aqua, MODIS-Terra, MISR-Terra, and CALIOP datasets.	20
Figure 2.6	Monthly mean coarse mode and fine mode AOD time series averaged over the domain (0-25°N, 20-50°W) for the time period 2003-2012. AODs are calculated from the MODIS-Aqua, and MODIS-Terra FMF, and AOD datasets.	22
Figure 2.7	Monthly mean Angstrom Exponent (AE) time series averaged over the domain (0-25°N, 20-50°W) for the time period 2003-2012. AE data are taken from the MODIS-Aqua, MODIS-Terra, and MISR-Terra datasets. AERONET AE time series for the Cape Verde Island (16.73°N, 22.94°W) is also shown.	23
Figure 2.8	Horizontal distributions of July climatological (2003-2012) mean MODIS-Aqua AOD at 550 nm (left panel), AIRS-Aqua temperature (*T*; middle panel), and AIRS-Aqua specific humidity (*q*; right panel) at 850 hPa.	25
Figure 2.9	Climatological (2003-2012) July mean a) vertical temperature (*T*) profiles in high (0-25°N, 20-30°W), moderate (0-25°N, 30-40°W), and the low (0-25°N, 40-50°W) dust regions of the domain, and the b)	26

deviation of these profiles from the domain averaged profile. Data are taken from the monthly mean AIRS-Aqua dataset.
Figure 2.10 Climatological (2003-2012) July mean a) vertical specific humidity (q) profiles in high (0-25°N, 20-30°W), moderate (0-25°N, 30-40°W), and the low (0-25°N, 40-50°W) dust regions of the domain, and the b) deviation of these profiles from the domain averaged profile. Data are taken from the monthly mean AIRS-Aqua dataset. 27
Figure 2.11 Monthly mean anomalies of MODIS-Aqua AOD at 550 nm (blue), and AIRS-Aqua temperature (T) at 850 hPa (brown) for a) high (0-25°N, 20-30°W), b) moderate (0-25°N, 30-40°W), and the c) low (0-25°N, 40-50°W) dust regions of the domain during Jan 2003-Dec 2012. Correlation coefficient (r) values are shown inside the parentheses, where 'NaN' indicates no statistical significance. 28
Figure 2.12 Monthly mean anomalies of MODIS-Aqua AOD at 550 nm (blue), and AIRS-Aqua specific humidity (q) at 925 hPa (brown) for a) high (0-25°N, 20-30°W), b) moderate (0-25°N, 30-40°W), and the c) low (0-25°N, 40-50°W) dust regions of the domain during Jan 2003-Dec 2012. Correlation coefficient (r) values are shown inside the parentheses. 29
Figure 2.13 EOF patterns of the a) 1st, b) 2nd, and c) 3rd modes of AOD decomposition. Abscissa and ordinate represent the longitude and latitude respectively. The amplitudes are normalized by the largest (absolute) value corresponding to each mode. AOD data are taken from the monthly mean AODs at 550 nm from the MODIS-Aqua dataset over 2003-2012. Fraction of the total variance for each mode are shown inside the parentheses. 31
Figure 2.14 Principal Component (PC) time series of the a) 1st, b) 2nd, and c) 3rd modes of AOD decomposition. The amplitudes are normalized by the largest (absolute) value corresponding to each mode. AOD data are taken from the monthly mean AODs at 550 nm from the MODIS-Aqua dataset over 2003-2012. Fraction of the total variance for each mode are shown inside the parentheses. 31
Figure 2.15 Same as figure 2.13, but for the temperature (T). The temperature data are taken from the monthly mean temperature at 850 hPa from the AIRS-Aqua dataset over 2003-2012. 32
Figure 2.16 Same as figure 2.14, but for the temperature (T). The temperature data are taken from the monthly mean temperature at 850 hPa from the AIRS-Aqua dataset over 2003-2012. 32
Figure 2.17 Same as figure 2.13, but for the humidity (q). The humidity data are taken from the monthly mean specific humidity at 925 hPa from the AIRS-Aqua dataset over 2003-2012. 34
Figure 2.18 Same as figure 2.14, but for the humidity (q). The humidity data are taken from the monthly mean specific humidity at 925 hPa from the AIRS-Aqua dataset over 2003-2012. 34

Figure 2.19 Correlation maps between the time series of grid point AOD anomalies (left data field) and the principal components of the temperature (right data field) corresponding to the a) 1st, b) 2nd, and c) 3rd modes of EOF decomposition of temperature. Abscissa and ordinate represent the longitude and latitude respectively. The temperature data are taken from the monthly mean temperature at 850 hPa from the AIRS-Aqua dataset over 2003-2012. Only the statistically significant values (at 95% confidence level) are shown on the map. 35

Figure 2.20 Same as figure 2.19, but for the correlations between the grid point AOD anomalies (left data field) and the principal components of the humidity (*q*; right data field). The humidity data are taken from the monthly mean specific humidity at 925 hPa from the AIRS-Aqua dataset over 2003-2012. 35

Figure 2.21 Heterogeneous correlation maps between the coupled SVD decomposition of AOD (left data field) and temperature (right data field) corresponding to the a) 1st, b) 2nd, and c) 3rd modes. Abscissa and ordinate represent the longitude and latitudes respectively. The temperature data are taken from the monthly mean temperature at 850 hPa from the AIRS Aqua dataset over 2003-2012. Only the statistically significant values (at 95% confidence level) are shown on the map. The Squared Covariance Fraction (SCF) values are shown inside the parentheses. 37

Figure 2.22 Time evolutions of the expansion coefficients of AOD (blue) and temperature (red) from the SVD analysis of AOD-T corresponding to the a) 1st, b) 2nd, and c) 3rd modes. The amplitudes are normalized by the largest (absolute) value corresponding to each mode. The Squared Covariance Fraction (SCF) values are shown inside the parentheses. Correlation coefficients (*r*) are also shown, where 'NaN' indicates no statistical significance. 38

Figure 2.23 Same as figure 2.21, but for the coupled SVD decomposition of AOD (left data field) and specific humidity (right data field). The specific humidity data are taken from the monthly mean specific humidity at 925 hPa from the AIRS-Aqua dataset over 2003-2012. 39

Figure 2.24 Same as figure 2.22, but for the coupled SVD decomposition of AOD (blue) and the specific humidity (red). The specific humidity data are taken from the monthly mean specific humidity at 925 hPa from the AIRS-Aqua dataset over 2003-2012. 40

Figure 3.1 Distribution of the Saharan dust aerosols (indicated by the MISR-Terra AOD) for July 2010, and the geographical locations of the parent (d01; indicated by the solid magenta lines) and nested (d03; indicated by the dashed magenta lines) domains for the model simulations. 50

Figure 3.2 WRF-Chem version 3.6.1 modeling system flowchart for this study. 51

Figure 3.3 Time and domain averaged (0Z July 01 to 18Z July 31, 2010, and 0-25°N, 20-50°W) vertical profiles of the a) temperature (*T*) from the 55

WRF-Chem simulations including dust (D36B and I36B), NCEP analyses and the AIRS datasets, and the b) temperature biases (ΔT), calculated with respect to the AIRS dataset.

Figure 3.4 Time and domain averaged (0Z July 01 to 18Z July 31, 2010, and 0-25°N, 20-50°W) vertical profiles of the a) water vapor mass mixing ratio (q) from the WRF-Chem simulations including dust (D36B and I36B), and the AIRS datasets, and the b) water vapor mass mixing ratio biases (Δq), calculated with respect to the AIRS dataset. 56

Figure 3.5 Domain averaged (0-25°N, 20-50°W) Cloud Liquid Water Path (LWP) time series from the WRF-Chem simulations including dust (D36B and I36B), and the measurements from the MODIS instrument on Terra and Aqua satellites. Individual data points represent daily mean values through July 1-31, 2010. 57

Figure 3.6 Domain averaged (0-25°N, 20-50°W) Precipitation rate (P) time series from the WRF-Chem simulations including dust (D36B and I36B), and measurements from the TRMM, and GPCP datasets. Individual data points represent daily mean values through July 1-31, 2010. 58

Figure 3.7 Time and domain averaged (0Z July 01 to 18Z July 31, 2010, and 0-25°N, 20-50°W) vertical profiles of the a) total dust mass mixing ratio (D), and the b) dust extinction (β) coefficient at 550 nm, and 532 nm from the WRF-Chem simulations including dust (D36B and I36B), and the CALIPSO dataset respectively. 59

Figure 4.1 Time averaged (0Z July 01 to 18Z July 31, 2010) horizontal distributions of the column mass densities (g/m2) of the a) atiken mode (D_{c1}), b) accumulation mode (D_{c2}), c) coarse mode (D_{c3}), and the d) total (D_c) dust aerosols. All the data are taken from the outputs of the simulation D36B. 62

Figure 4.2 Vertical profiles of the time and domain averaged (0Z July 01 to 18Z July 31, 2010; 0-25°N, 20-50°W) a) dust mass mixing ratio (D; μg/kg) for the atiken mode ($\times 10^{-1}$), accumulation mode, and the coarse mode dust aerosols from D36B, b) aerosol absorption coefficients (β_a; km-1) from D36A (dashed lines) and D36B (solid lines), and c) aerosol scattering coefficients (β_s; km-1) from D36A (dashed lines) and D36B (solid lines) at different shortwave wavelengths. 63

Figure 4.3 Time averaged (0Z July 01 to 18Z July 31, 2010) horizontal distributions of the absorption (abs), scattering (scatt), and total dust AOD at different shortwave (SW) wavelengths. Abscissa and ordinate represent the longitude and latitude respectively. Dust AODs are calculated from the difference between the AODs from the dust-laden (D36B) and the dust-free (D36A) runs. 65

Figure 4.4 Same as figure 4.3, but the data correspond to the experiment D36DRY. 66

Figure 4.5 Time averaged (0Z July 01 to 18Z July 31, 2010) horizontal distributions of the total dust AOD at different longwave wavelengths. Abscissa and ordinate represent the longitude and latitude respectively. 67

Dust AODs are calculated from the difference between the AODs from the dust-laden (D36B) and the dust-free (D36A) runs.

Figure 4.6 Schematic diagram of the time and domain averaged (0Z July 01 to 18Z July 31, 2010; 0-25°N, 20-50°W) radiative flux components (W/m^2) for the clear sky condition. All the data are taken from the outputs of the experiment D36. 69

Figure 4.7 Time and domain averaged (0Z July 01 to 18Z July 31, 2010; 0-25°N, 20-50°W) horizontal distributions of the a) shortwave, b) longwave, and c) net (shortwave + longwave) radiative forcing (W/m2) of the atmosphere (ATM) for the clear sky condition. All the data are taken from the outputs of the experiment D36. 70

Figure 4.8 Same as figure 4.7, but for the surface (SUR). 71

Figure 4.9 Same as figure 4.7, but for the top of the atmosphere (TOA). 72

Figure 4.10 Instantaneous (12 Z, July 12, 2010) distributions of the a) total dust mass mixing ratio (D; µg/kg), dust induced changes (B-A) of the atmospheric heating rates (K/day) due to the b) shortwave (ΔH_{SW}), c) longwave (ΔH_{LW}), and d) net radiation (ΔH_{NET}). All the data are taken from the outputs of the experiment D36DRY. 73

Figure 4.11 Mean vertical profiles (averaged over 0Z July 01 to 18Z July 31, 2010, and the respective regions) of the atmospheric heating rates (K/day) due to the shortwave (H_{SW}), longwave (H_{LW}), and net radiation (H_{NET}) in the high (0-25°N, 20-30°W; figures a-c), moderate (0-25°N, 30-40°W; figures d-f), and low (0-25°N, 40-50°W; figures g-i) dust regions. All the data are taken from the outputs of the experiment D36. 75

Figure 4.12 Monthly mean (0Z July 01 to 18Z July 31, 2012) distributions of the a) Dust mass mixing ratio (D; µg/kg), b) atmospheric temperature (T; K) without dust (D36A), and the c) dust induced temperature changes (ΔT; D36B-D36A) at different altitudes corresponding to the different model levels. All the data are taken from the experiment D36 with every 6 hour simulation outputs covering the domain: 0-25°N, 20-50°W. 77

Figure 4.13 Monthly mean (0Z July 01 to 18Z July 31, 2010) horizontal fields of the Sensible heat fluxes (SH; W/m2) a) without dust (D36A), b) with dust (D36B), and c) their difference (D36B-D36A). Heat fluxes are calculated from the accumulated values at the end of the simulation (18Z, July 31, 2010). 78

Figure 4.14 Same as figure 4.13, but for the latent heat fluxes (LH). 78

Figure 4.15 Mean vertical profiles (averaged over 0Z July 01 to 18Z July 31, 2010, and the respective regions) of the cloud fractions (fraction of the grid cells with cloud mass mixing ratio higher than or equal to 1e-6 g/kg; C_F) without (D36A) and with dust (D36B), and their difference (D36B-D36A) for the high (0-25°N, 20-30°W; figures a-b), moderate (0-25°N, 30-40°W; figures c-d), and low (0-25°N, 40-50°W; figures e-f) dust regions. All the data are taken from the outputs of the experiment D36. 80

Figure 4.16 Schematic diagram of the time and domain averaged (0Z July 01 to 18Z July 31, 2010; 0-25°N, 20-50°W) radiative flux components (W/m^2) for all sky condition. All the data are taken from the outputs of the experiment D36. 82

Figure 5.1 Time and domain averaged (0Z July 01 to 18Z July 10, 2010, and 10-25°N, 20-40°W) vertical profiles of the a) Cloud droplet number concentration (C_N), and b) Cloud water mass mixing ratio (C_M) from the sensitivity tests. 86

Figure 5.2 Time and domain averaged (0Z July 06 to 18Z July 13, 2010, and 2.5-11.5°N, 30-40°W) vertical profiles of the a) Cloud water number concentration (C_N) from the Dust-Free (I04A) and Dust-laden (I04B) runs, and the b) dust induced changes (I04B-I04A) of the Cloud water number concentration (ΔC_N). 88

Figure 5.3 Time and domain averaged (0Z July 06 to 18Z July 13, 2010, and 2.5-11.5°N, 30-40°W) vertical profiles of the a) Cloud water mass mixing ratio (C_M) from the Dust-Free (I04A) and Dust-laden (I04B) runs, and the b) dust induced changes (I04B-I04A) of the Cloud water mass mixing ratio (ΔC_M). 88

Figure 5.4 Cloud droplet size distributions (droplet radius; C_r) from the dust-free (I04A) and the dust-laden (I04B) runs. 89

Figure 5.5 Time averaged (0Z July 06 to 18Z July 13, 2010) horizontal distributions of the Cloud Liquid Water Path (LWP) a) without dust (I04A), b) with dust (I04B), and the c) dust induced changes (I04B-I04A). 91

Figure 5.6 Percentage contributions (normalized) to the total Cloud Liquid Water Path (LWP) from discrete size bins. All the data correspond to the experiment I04. 91

Figure 5.7 Mean vertical profiles (0Z July 06 to 18Z July 13, 2010, and 2.5-11.5°N, 30-40°W) of the a) Cloud fractions (fraction of the grid cells with cloud mass mixing ratio higher than or equal to 10^{-6} kg/kg; C_F) from I04A and I04B, and b) their difference (ΔC_F). 92

Figure 5.8 Mean vertical profiles (0Z July 06 to 18Z July 13, 2010, and 2.5-11.5°N, 30-40°W) of the a) raindrop number concentrations ($R_N \times 10^3$; #/kg of air) from I04A and I04B, and b) their difference($\Delta R_N \times 10^3$; #/kg of air). 94

Figure 5.9 Mean vertical profiles (0Z July 06 to 18Z July 13, 2010, and 2.5-11.5°N, 30-40°W) of the (a) rain water mass mixing ratio ($R_M \times 10^{-6}$; kg/kg of air) from I04A and I04B, and b) their difference ($R_M \times 10^{-6}$; kg/kg of air). 94

Figure 5.10 Mean vertical profiles (0Z July 06 to 18Z July 13, 2010, and 2.5-11.5°N, 30-40°W) of the a) raindrop evaporation rate (E_R x10^{-9}; kg kg-1s-1) from I04A and I04B, and b) their difference (ΔE_R x10^{-9}; kg kg-1s-1). 96

Figure 5.11 Conditionally averaged (considering only the precipitating grid cells over the domain: 2.5-11.5°N, 30-40°W) explicitly resolved precipitation rate time series. All the data correspond to the experiment I04. 97

Figure 5.12 Time averaged (0Z July 06 to 18Z July 13, 2010) horizontal distributions of the dust induced changes (I04B-I04A) of the a) water vapor evaporation rate from the surface (mm/day), b) accumulated precipitation rate at the surface (mm/day), c) vertically integrated zonal moisture flux (mm/day), and d) vertically integrated meridional moisture flux (mm/day). All the data correspond to the experiment I04. 98

Figure 5.13 Histograms of the buoyancy (ms-1) distributions for model levels a) 1-10 (0 – 0.8 km), and b) 11-20 (0.8 – 3.2 km). All the data correspond to the experiment I04. 100

Figure 5.14 Schematic diagram of the time and domain averaged (0Z July 01 to 18Z July 31, 2010; 0-25°N, 20-50°W) radiative flux components (W/m^2) for direct + indirect effects in all sky condition. All the data correspond to the experiment I36. 104

Chapter 1: Introduction

1.1 Research Background and Motivation

North Africa is the largest source of the dust aerosols in the world [e.g., *Huang et al.*, 2010; *Rodríguez et al.*, 2011]. Dust plumes released from the Sahara desert in North Africa can affect the regional climate and hydrological cycle [*Zhu et al.*, 2007]. Saharan dust plumes often travel westward across the Atlantic Ocean and form a warm and dry air layer in the troposphere. This unique dust-laden air is commonly referred as the Saharan Air Layer in the literature [SAL; e.g., *Prospero and Carlson*, 1972; *Dunion and Velden*, 2004; *Evan et al.*, 2006]. Numerous studies have recognized the importance of the SAL in the tropical east Atlantic climate. For example, some studies reported a significant correlation between the Saharan dust activity and the Sea Surface Temperature (SST), where higher dust anomalies are associated with cooler SST [*Lau and Kim*, 2007; *Evan et al.*, 2008; *Foltz and McPhaden*, 2008]. Based on several case studies on Tropical Cyclones (TC) and hurricane genesis, *Dunion and Velden* [2004] demonstrated that the SAL suppresses the TC activity by inhibiting tropical deep convection. In addition, the SAL can play a significant role in the evolution of the African Easterly Jet (AEJ) and the African Easterly Wave (AEW). While some studies suggest that SAL intensifies the AEW [e.g., *Jones et al.*, 2004; *Grogan et al.*, 2015], other studies indicate that the SAL weakens the growth of AEW [e.g., *Sun et al.*, 2009; *Jury and Santiago*, 2010].

The main focus of the present study is not the SAL itself, rather the Saharan dust aerosols that it is composed of. As dust is the primary constituent of the SAL, it is important to identify the role of the dust in the SAL's characteristics (e.g., maintaining the warm and dry nature during

its transport across the Atlantic Ocean) which influences the aforementioned tropical activities. However, the potential role of dust and various pathways by which the SAL affect these atmospheric processes are not very well understood [e.g., *Braun*, 2010; *Grogan et al.*, 2016]. This is not only due to the uncertainties in our knowledge of the physical and chemical properties of dust, but also due to our lack of understanding of the interactions of dust with radiation, cloud, and moisture. The primary objective of this study is to advance our understanding of the impacts of dust on radiation, cloud, and precipitation through both remote sensing and the numerical simulation data. Our study domain is chosen over the tropical east Atlantic Ocean that encompasses the path of the Saharan dust plumes.

Studying the effect of dust on radiative fluxes has been an active area of research in the past few decades. However, there are large uncertainties in the magnitude of the dust radiative effects owing to the complex interaction of dust particles with longwave and shortwave radiation in different ambient conditions. In addition, the wide range of chemical composition, size distribution, and number concentrations of dust particles make it difficult to correctly estimate the radiative forcing of dust. On the other hand, much less effort has been made to investigate the influence of dust on cloud microphysical processes, possibly due to the lower hygroscopicity of fresh dust particles. Nevertheless, most of the previous studies on dust effects on radiation and clouds employ either the radiative transfer model or the cloud resolving model to investigate the radiative and microphysical effects separately [e.g., *Stephens et al.*, 2004; *Zhu et al.*, 2007; *Perrone et al.*, 2012]. Most of these models focus only on very short timescales (hours to days) and do not include all the processes in the atmosphere, as well the feedback between the radiation and cloud microphysics. Coupled meteorology-chemistry-aerosol models are therefore vital tools for investigating a relatively complete

representation of the dust effects. One such model is the mesoscale Weather Research and Forecasting model (WRF) which can be coupled with the Chemistry module (WRF-Chem). In this study, we use the WRF-Chem model to investigate both radiative and cloud microphysical effects of the Saharan dust including the feedbacks of these effects. The WRF-Chem model not only treats the coupled radiative-microphysical processes but also includes the prognostic dust distributions driven by the model's meteorological field. Advancements of the computational resources allow us to simulate the coupled dust-radiation-cloud effects in finer resolution and longer timescales (e.g., months). In addition to the simulation data, monthly mean climatological satellite observation data over 10 years (2003-2012) are also used to examine the covariability of the Saharan dust activity with the temperature and moisture anomalies over the tropical east Atlantic Ocean.

Following section presents a brief summary of the current understanding of the dust-cloud-radiation interactions based on a survey of the recent literature.

1.2 Current Understanding of the Dust-Cloud-Radiation Interactions

Mineral dust aerosols contribute a significant fraction of the total global aerosol burden, and play an important role in climate studies [*Buseck and Pósfai*, 1999; *Textor et al.*, 2006]. As for any type of atmospheric aerosols, the effects of dust on climate are commonly classified into three major categories: direct effect, semi-direct effect, and the indirect effects. Dust particles interact directly with both shortwave (SW) and longwave (LW) radiations (direct effect), change the cloud cover through evaporation of cloud droplets (semi-direct effect), and modify the cloud and precipitation properties through serving as the Cloud Condensation Nuclei [indirect effects; e.g., *Choobari et al.*, 2014]. The semi-direct effect of dust is beyond the scope of this study, therefore we only focus on the direct and indirect effects of dust.

Following sub-sections highlight the key progress in the understanding of the interactions of dust aerosols with radiation and clouds. In addition, dust effects on the atmospheric convection is also discussed.

1.2.1 Direct Effect of Dust

The direct effect of dust is linked to the interactions of dust particles with both shortwave (SW) and longwave (LW) radiative fluxes. It varies both temporally and spatially [e.g., *Shell and Somerville*, 2007]. The interaction of the dust particles with radiation is more complex than that of the other fine aerosols as they scatter and absorb both shortwave and longwave radiations [*Mallet et al.*, 2009; *Choobari et al.*, 2014]. In clear sky conditions, aerosol direct radiative effects in the shortwave spectrum is strongly dependent on the aerosol optical properties (size, chemical composition etc.), underlying surface albedo, and the solar zenith angle [e.g., *Boucher et al.*, 1998]. The optical properties of dust determine its Single Scattering Albedo (SSA), the ratio between the scattering and the total (absorption + scattering) extinction of light, and it is the most important factor that controls the shortwave radiative forcing [*Forster et al.*, 2007]. Likewise, the longwave forcing depends on the vertical profiles of dust, atmospheric temperature, underlying surface emissivity, and the atmospheric transmission [*Haywood et al.*, 2005; *Forster et al.*, 2007]. In addition to these factors, aerosol heating rates and the direct radiative effects in the longwave spectrum are also reported to be sensitive to the vertical distribution of the moisture [*Perrone et al.*, 2012].

Both the sign and magnitude of the direct radiative forcing are the important parameters for climate studies. The radiative forcing is calculated from the radiative fluxes at the top of the atmosphere and at the surface. The radiative fluxes are obtained from the radiative transfer

model which utilizes the idealization or measurement of the aforementioned physical and optical properties of dust and atmosphere. Uncertainties in these variables have a large impact on the heating rates and the radiative forcing [*Shell and Somerville*, 2007; *Perrone et al.*, 2012]. For example, *Shell and Somerville* [2007] calculated the global radiative forcing in two extreme cases (corresponding to the measurements) of the dust absorption. They found that increasing the dust single scattering albedo (SSA) from 0.85 to 0.97 lead to the global average shortwave forcing at the top of the atmosphere of dust becoming more than doubled while the shortwave forcing at the surface being halved. In addition to the measurement uncertainties, dust particle properties are also highly variable in time and space [*Sokolik et al.*, 2001; *Shell and Somerville*, 2007], leading to the uncertainty in the net radiative forcing of dust. Nevertheless, most previous studies indicate that dust aerosols have overall positive radiative heating rate (both shortwave and longwave combined) inside the dusty atmospheric layer [*Zhu et al.*, 2007; *Mallet et al.*, 2009; *Zhao et al.*, 2013; *Vinoj et al.*, 2014]. For example, *Mallet et al.* [2009] reported instantaneous perturbations in solar heating rates comprised between +4 K/day to +7 K/day within the dusty layer over the West Africa during a major dust storm. Corresponding longwave effects include the atmospheric cooling ranging from -0.10 to -0.20 K/day within the dusty layer and warming of +4 K/day to +9 K/day at the surface. The longwave warming in the boundary layer is due to the increase in downwelling flux that enhances the atmospheric absorption in the lower atmosphere [*Zhu et al.*, 2007]. However, the magnitudes of the regional and seasonal mean atmospheric heating rates (especially the LW) are lower than those found during the dust events. *Zhu et al.* [2007] estimated the radiative forcing of the Saharan dust over the tropical east Atlantic Ocean during the summer season (June-August). They found that the dust induced heating rate perturbations off the

Sharan coast at the peak dust altitude are +0.4 K/day and -0.5 K/day for the shortwave and longwave respectively.

The net radiative forcing by dust, which is typically calculated at the top of the atmosphere and the surface is the difference between the dust-laden and dust-free net (shortwave + longwave) radiative fluxes. Over the bright surfaces (e.g., desert) with high surface albedo, the shortwave forcing of dust is usually small and difficult to estimate [*Christopher and Jones*, 2007]. However, over relatively darker surfaces such as the Atlantic Ocean, dust aerosols increase the reflectivity of the earth-atmosphere system, giving a negative radiative forcing. In the longwave spectrum, the sign of the radiative forcing is positive that can compensate the shortwave forcing [*Zhang and Christopher*, 2003; *Christopher and Jones*, 2007]. Most previous studies found net negative radiative forcing of dust at the surface, while the forcing can be either positive or negative at the top of the atmosphere [*Woodward*, 2001; *Shell and Somerville*, 2007; *Zhu et al.*, 2007; *Mallet et al.*, 2009; *Perrone et al.*, 2012; *Choobari et al.*, 2014]. *Woodward* [2001] estimated a global annual mean dust net radiative forcing of +0.07 W/m^2 at the top of the atmosphere and -0.82 W/m^2 at the surface. *Shell and Somerville* [2007] obtained a global annual average net radiative forcing of -0.49 W/m^2 at the top of the atmosphere and -0.97 W/m^2 at surface respectively. However, the local dust forcing can be much larger than these values, especially in the downstream of the dust source regions such as the Sahara desert. For example, *Zhu et al.* [2007] found that the radiative forcing of the Saharan dust off-shore of the African coast averaged through June to August are -14.37 W/m^2 at the top of the atmosphere and -14 W/m^2 at the surface.

1.2.2 Indirect Effects of Dust

The indirect effects of dust are linked to the cloud microphysics. Besides altering the radiative fluxes, dust aerosols can also modify the cloud and precipitation properties, while they serve as the seeds for the cloud droplets and ice crystals. The efficiency of a particular aerosol species to serve as Cloud Condensation Nuclei (CCN) depends on its hygroscopicity, which is controlled by the composition of its water soluble component. Generally, the fresh dust particles have relatively lower hygroscopicity making them inefficient CCN [e.g., *Tang et al.*, 2015]. However, dust particles coated with soluble materials (e.g., sulfate) can become efficient CCN [*Wurzler et al.*, 2000]. Various transformation processes such as coagulation, heterogeneous reactions on the surface of the dust particles (referred as the dust particle aging) may change their hygroscopicity [*Formenti et al.*, 2011; *Denjean et al.*, 2015; *Tang et al.*, 2015]. For example, *Tang et al.* [2015] investigated the CCN activities of calcite (CaCO3; as a proxy for the mineral dust, which has very small hygroscopicity value) and its potential aging products. They found a significant increase of the hygroscopicity parameter in the aged dust particles, making them efficient CCN compared to the primary dust particles. In the Oceanic environment dust particles are readily enriched with sulfate and nitrate ions making them water soluble [*Formenti et al.*, 2011]. Due to the higher humidity in the marine atmosphere, the dust particles become wet by forming thin water films on their surface. This causes efficient transformation of sulfur dioxide to sulfate and nitrogen dioxide to nitrate, making them capable of droplet condensation [*Formenti et al.*, 2011]. In addition, as the critical saturation ratio for droplet activation is lower for the larger sized aerosols, such as the dust particles, they have better advantage to become CCN [e.g., *Tao et al.*, 2012]. Therefore, while the fresh dust particles released from the Sahara desert are hydrophobic (and poor CCN),

various transformation processes during their transport across the Atlantic Ocean can modify their physical and chemical properties [e.g., *Denjean et al.*, 2015], which can change their hygroscopic properties. As a result, the aged dust aerosols over the Atlantic Ocean have the potential to serve as efficient CCN.

The aerosol indirect effect has two components. The first indirect effect, also known as the cloud albedo effect or the Twomey effect [*Twomey*, 1977] refers to the enhancement of the cloud reflectivity as a consequence of the aerosol induced change in the cloud droplet size. In the presence of higher aerosol concentration, the number of CCN activated at a particular supersaturation increases, leading to more cloud droplets with reduced sizes. This is verified by numerous studies. For instance, based on the satellite observations *Bréon and Colzy* [2000] reported that cloud droplet sizes over the land are smaller than those over the Ocean, owing to the abundance of biomass burning and anthropogenic aerosols over the land. *Ou et al.* [2012] found a statistically significant negative correlation between the East Asian dust aerosol optical depth and the cloud particle size, indicating that cloud droplets become smaller with increasing dust loading. *Rosenfeld et al.* [2001] also showed that the cloud droplets forming within the desert dust are smaller in size.

Cloud Liquid Water Path (LWP), a measure of the total amount cloud water over certain area is an important parameter in the aerosol-cloud interactions. For a constant cloud LWP, more numerous but smaller cloud droplets eventually increases the cloud cover (and albedo), giving negative climate forcing. However, the cloud LWP can increase, decrease, or remain constant depending on the competing effects of the droplet collision-coalescence and entrainment and evaporation of cloud droplets [*Han et al.*, 2002; *Ackerman et al.*, 2004]. As a result the climate forcing of the Twomey effect is unclear.

The first indirect effect of aerosols has consequence on the precipitation formation. Aerosol induced reduction of the cloud droplet size leads to the reduction in the collision-coalescence efficiency among the cloud droplets [e.g., *Ramanathan et al.*, 2001; *Saleeby et al.*, 2015]. This causes the delay in the initiation of precipitation and suppression of precipitation in the stratiform clouds, thereby enhances the cloud lifetime [*Kaufman et al.*, 2005]. This is referred as the aerosol second indirect effect, or the Albrecht effect [*Albrecht*, 1989]. Many studies have verified the precipitation suppression in the shallow clouds with higher aerosol concentration, which follows the Albrecht effect. For example, *Givati and Rosenfeld* [2004] found a reduction in precipitation over two locations they studied, both are downwind of the pollution regions. However, few studies reported that the precipitation inhibition induced by the dust aerosols is small. For instance, based on the remote sensing data *Rosenfeld et al.* [2001] showed that the Saharan dust aerosols indeed suppress the precipitation but the detrimental impact of dust is smaller than that of the other aerosols. *Teller et al.* [2012] also found that the dust impact on precipitation is negligible. It should also be noted that several more recent studies have reported the increase of precipitation with increasing aerosol concentration [e.g., *Lee and Yum*, 2012; *Zhou et al.*, 2017]. Enhancements of the precipitation are typically associated with the convective clouds with mixed phases of hydrometeors, although its detailed mechanism is not very clear [*Lee and Yum*, 2012]**.**

Similar to the other aerosols, the sign of the net radiative forcing due to the dust indirect effects is uncertain. This is because the enhancement of cloud droplet number concentration with reduced droplet size (Twomey effect) does not necessarily enhance the cloud albedo that would have caused negative radiative forcing. Likewise, the dust impact on precipitation

(Albrecht effect) is dependent on environmental conditions, thereby the modulation of precipitation does not necessarily change the cloud lifetime.

1.2.3 Dust Effects on Convection

The primary source of energy that drives the atmospheric convection comes from the radiation energy retained by the atmosphere and the surface. Therefore, any dust induced direct or indirect perturbation to the net heating of the atmosphere (and of the surface as a consequence) can influence the convective activities. Very limited number of studies are performed focusing specifically on the dust effects on convection. *Stephens et al.* [2004] used idealized model simulations to study the radiative effects of dust on tropical convection and found that the radiative heating of dust suppresses the convection in the lower troposphere for the initial period of the simulation. Using the remote sensing and model analyses data over the tropical east Atlantic Ocean, *Wong and Dessler* [2005] investigated the impact of the dust-laden SAL on the tropical deep convection. They suggested that the warm and dry air in the SAL raises the lifting condensation level and level of free convection, and increases convective barrier that leads to the suppression of convection. Using numerical model simulations *Solomos et al.* [2011] demonstrated that increasing the concentration of soluble dust particles leads to stronger convection and intense updraft. However, a clear understanding of the impact of dust due to the combination of both the radiative and microphysical effects is still not sufficient.

1.3 Dissertation Outline

The purpose of this study is to investigate the direct and indirect effects of Saharan dust aerosols, and the subsequent changes of the tropical convection and radiation budget over the east Atlantic Ocean. In this chapter, we have discussed the motivation behind this study, and

the review of the available literatures on the dust-cloud-radiation interactions. The subsequent chapters cover the results of the analysis of the observation and numerical simulation data for investigating the dust effects. Structure of this dissertation is briefly discussed in the following.

Chapter 2 presents the analysis of the 10 year climatological satellite data to identify any potential relationship between the anomalies of the Saharan dust loading and the tropospheric temperature and humidity. Chapter 3 includes a brief description of the WRF-Chem model, various configurations of the simulation experiments, and also the validation of the model outputs. Chapter 4 investigates the optical properties of the Saharan dust and its impact on the radiative forcing at the surface, inside the atmosphere, and at the top of the atmosphere based on the model outputs. Chapter 5 gives the analysis of the model data to explore the impact of dust on the cloud and precipitation properties. Finally, Chapter 6 brings together the findings of this study and also outlines the possible future work related to this work.

Chapter 2: Saharan Dust Climatology

2.1 Observation Variables and Datasets

As mentioned in Chapter 1, the Saharan dust aerosols are transported over the Atlantic Ocean which form a unique warm and dry air layer in the troposphere, called the Saharan Air Layer (SAL). The SAL encompasses a large geographical area from the Sahara desert to the United States, including a significant part of the North Atlantic Ocean [*Dunion and Velden*, 2004]. This chapter presents the results of our analyses of the multiyear climatology of the Saharan dust aerosols, as well as the thermal characteristics of the SAL. The study domain is over the tropical east Atlantic Ocean which covers the trajectory of the Saharan dust plumes. We utilize the 10 year (2003-2012) climatological data from various observational datasets on different remote sensing platforms. The analyses is based on the monthly mean data over the 10 year period including the following variables: Aerosol Optical Depth (AOD), aerosol Fine Mode Fraction (FMF), Angstrom Exponent (AE), tropospheric temperature (T) and the specific humidity (q).

AOD is a measure of the extinction of radiation through absorption and scattering in an atmospheric column due to all types of aerosols, including the dust particles. Because of the availability of ground based and satellite measurements of the AOD, it is commonly used as a proxy to the total aerosol concentration, where higher AOD is an indicator of the increased aerosol loading for a particular location. For a total of N aerosol species, AOD (τ) at a specific wavelength is defined as follows:

$$\tau = \int \sum_{i=1}^{N} (\beta_{ai} + \beta_{si}) dz$$

where, β_{ai} and β_{si} are the absorption and scattering coefficients due to the individual aerosol species respectively. We analyze the climatological AOD anomalies to identify the highest dust loading month through 2003-2012, which is then used in the modeling studies and discussed in the subsequent chapters.

In addition to the AOD, we use two parameters- FMF and AE to examine the dominance of dust loading with respect to the other aerosol species over the study domain. FMF (*f*) gives the relative abundance of smaller and larger sized aerosols which is calculated from the ratio between the AOD for fine mode particles (particle diameter < 1 μm) to the total (fine mode + coarse mode) AOD:

$$f = \frac{\tau_f}{\tau_f + \tau_c}$$

where, τ_f and τ_c are the AODs due to the fine and coarse mode aerosols respectively. Typically, anthropogenic and biomass burning aerosols are the fine mode aerosols while dust and sea salt aerosols fall into the coarse mode regime. Therefore, lower FMF values i.e. higher coarse mode to fine mode AOD ratio represents the prevalence of dust and sea salt over other aerosol species.

AE, an empirically derived parameter that gives the wavelength dependence of AOD, is also used to identify the size information of the aerosols in our domain. The AE (α) is defined as follows:

$$\alpha = \frac{\ln(\tau_1/\tau_2)}{\ln(\lambda_2/\lambda_1)}$$

where, τ_1 and $\tau_2$are the total AODs at wavelengths λ_1 and λ_2 respectively. Smaller AE values imply the dominance of larger sized particles [*Schuster et al.*, 2006].

The warm and dry features of the SAL is investigated using the monthly mean climatological tropospheric temperature (T) and the specific humidity (q) data. In addition, the climatological anomalies of the tropospheric temperature and humidity are compared to the AOD anomalies to find the potential role of the dust particles in the warm and dry nature of the SAL. To do this, we calculate the Pearson correlation coefficient (r) between the time series of AOD with the time series of T and q. The Pearson correlation coefficient (r) is calculated as follows:

$$r = \frac{\sum_{i=1}^{N}(x_i - \bar{x})(y_i - \bar{y})}{\sqrt{\sum_{i=1}^{N}(x_i - \bar{x})^2}\sqrt{\sum_{i=1}^{N}(y_i - \bar{y})^2}}$$

where, x_i and y_i are the individual samples of two variables x and y respectively. N is the total number of samples, and $\bar{x}$ and $\bar{y}$ are the respective mean of these variables. A higher value of r indicates a strong correlations between the two variables.

The AOD data used in this study are obtained from the retrievals of the Moderate Resolution Imaging Spectroradiometer (MODIS) instrument on both Aqua and Terra satellites (MODIS-Aqua, and MODIS-Terra respectively), Multi-angle Imaging SpectroRadiometer (MISR) instrument on Terra satellite (MISR-Terra), and the Cloud-Aerosol Lidar with Orthogonal Polarization (CALIOP) instrument on CALIPSO satellite. The AODs we use correspond to the retrievals at 550 nm, 550 nm, 555 nm, and 532 nm wavelengths from MODIS-Aqua, MODIS-Terra, MISR-Terra, and CALIOP respectively. Although, these AOD data are retrieved at different spectral wavelengths, they are fairly close to 550 nm, hence it is reasonable to assume that it will not cause any significant uncertainty in our analysis.

Prior to the analysis of the AOD climatology, the satellite measurement of AODs are validated against a reliable ground based AOD measurements (discussed in section 2.2). The AOD measurements from the ground based photometer called Aerosol Robotic Network (AERONET) is used as a benchmark for the validation. As the AERONET does not have any direct AOD retrieval at 550 nm, we use the direct-sun algorithm AERONET AOD retrieval at 440 nm to calculate the AOD at 550 nm by using the Ångström's formula [*Ångström*, 1964]:

$$\tau_{550} = \tau_{440}\left(\frac{440}{550}\right)^{\alpha}$$

where, τ_{550} and τ_{440} are the AOD's at 550 nm and 440 nm respectively. The other parameter α is the Angstrom Exponent (AE) for the spectral range 440-675 nm.

The Angstrom Exponent (AE) and the aerosol Fine Mode Fraction (FMF) data used in this study are taken from the MODIS-Terra, MODIS-Aqua, MISR-Terra and the AERONET datasets respectively. These two variables, together with the AOD are used to characterize the aerosol composition in our domain (discussed in section 2.3).

The tropospheric temperature and the specific humidity data, taken from the Atmospheric InfraRed Sounder (AIRS) instrument on Aqua satellite (AIRS-Aqua) are used to find any potential significant correlations of AOD, temperature, and humidity variabilities throughout the study period (discussed in section 2.4). The retrieval versions of all the datasets and their respective spatial resolutions are presented in table 2.1. All of these datasets are available through 2003-2012 with the exception of the CALIOP measurements which are available through 2006-2012.

Table 2.1: Dataset versions and the spatial resolutions of the data from various observation platforms used in this study.				
Instrument/Platform	Data Level/version	Data products used	Horizontal Resolution (latitude × longitude)	Vertical Resolution
MODIS/Aqua	Level 3 version 6	AOD, AE, FMF	1° × 1°	N/A
MODIS/Terra	Level 3 version 6	AOD, AE, FMF	1° × 1°	N/A
MISR/Terra	Level 3 version 4	AOD, AE	0.5° × 0.5°	N/A
AIRS/Aqua	Level 3 version 6	Temperature, Specific Humidity	1° × 1°	24 pressure levels from 1000-1 hPa
CALIOP/CALIPSO	Level 3.0	AOD	2° × 5°	N/A
AERONET	Level 2.0 (Direct)	AOD, AE	N/A	N/A

2.2 Aerosol Climatology over the East Atlantic Ocean

We validate the satellite measurements of aerosol loading by comparing the AODs from MODIS-Aqua, MODIS-Terra, MISR-Terra, and the CALIOP against the AERONET AOD.

The AERONET measurement site in the Cape Verde Island (16.73°N, 22.94°W) is chosen for the validation, as it is located in the downstream of the Sahara desert and also on the east Atlantic Ocean. Monthly mean AOD values from these platforms are shown in the scatter plot (figure 2.1) where individual points represent the mean AOD corresponding to a single calendar month from January 2003 to December 2012.

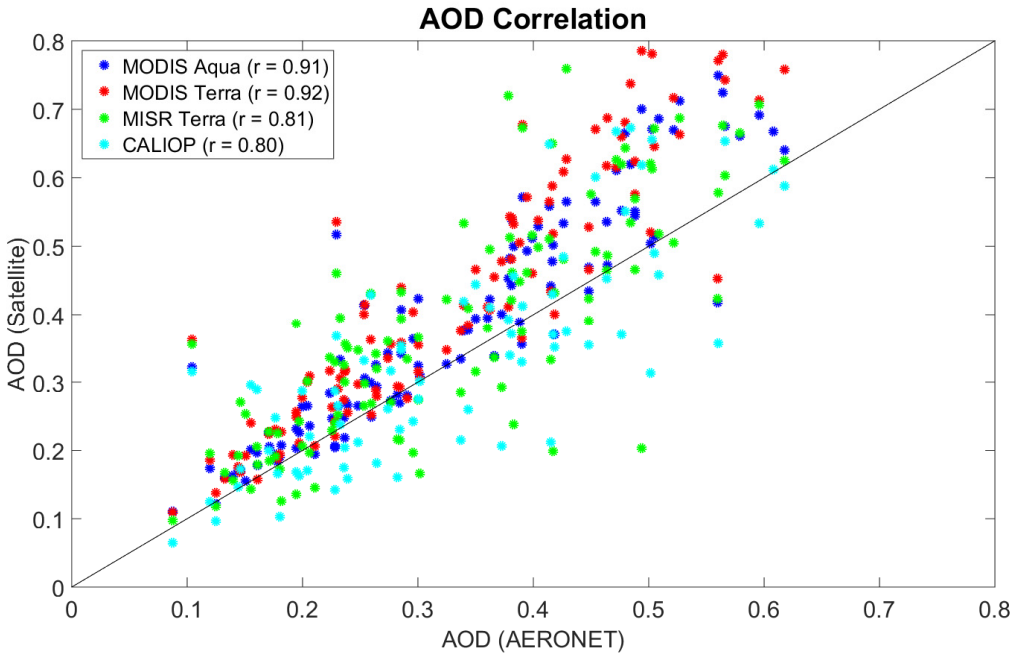

Figure 2.1 Scatter plot showing the comparison of the monthly mean AODs from MODIS-Aqua, MODIS-Terra, MISR-Terra, and CALIOP against the AERONET AOD. Individual points represent the monthly mean AOD measurements at the Cape Verde Island (16.73°N, 22.94°W) during 2003-2012. The Pearson correlation coefficient (*r*) values are shown inside the parentheses.

The AOD comparison (figure 2.1) shows good agreement of the satellite measurements with the ground based measurements. The Pearson correlation coefficients (*r*) are found to be ranging from 0.80 (AERONET and CALIOP) to 0.91 (AERONET and MODIS-Aqua). Therefore, the satellite AOD measurements especially, the MODIS-Aqua and MODIS-Terra are reliable to be used for studying the aerosol climatology.

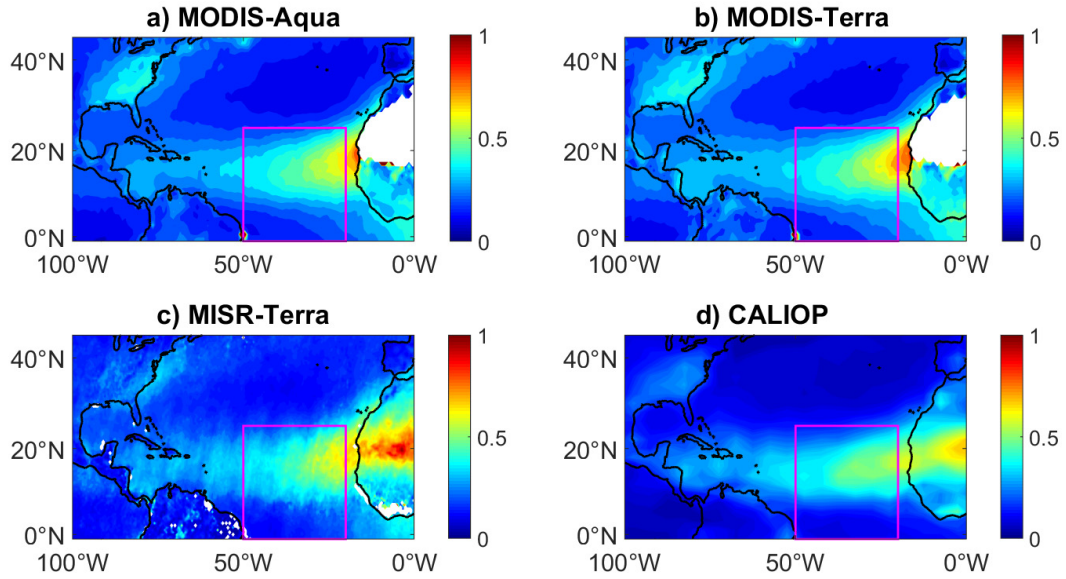

Figure 2.2 June-August AOD climatology (averaged through 2003 to 2012) over the downstream of the Sahara desert from a) MODIS-Aqua, b) MODIS-Terra, c) MISR-Terra, and d) CALIOP. Abscissa and ordinate represent the longitude and latitude respectively. Rectangles indicate the domain chosen for the multiyear dust climatology study and the analysis of the correlations of AOD anomalies with the temperature and humidity anomalies.

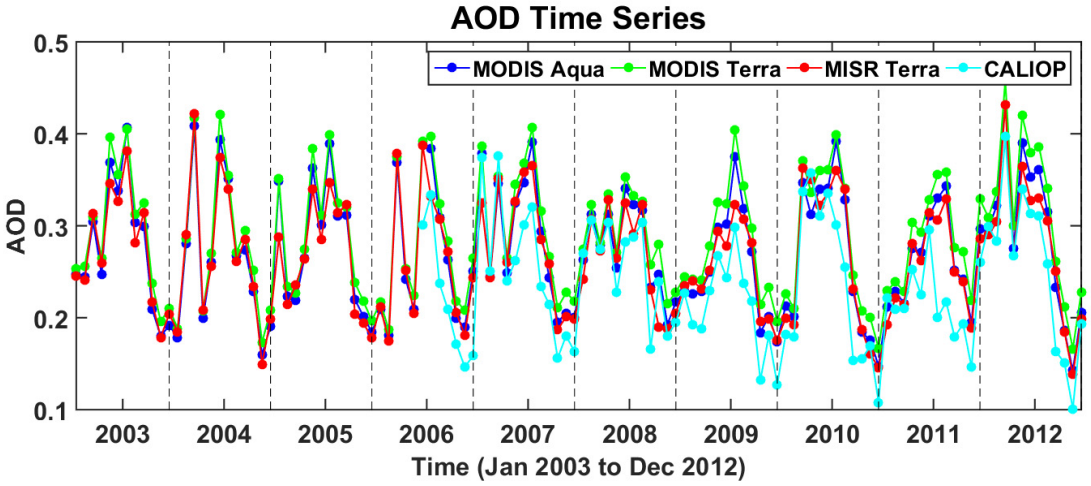

Figure 2.3 Monthly mean AOD time series for the time period 2003-2012 from the MODIS-Aqua, MODIS-Terra, MISR-Terra, and CALIOP datasets. AOD data are averaged over the study domain (0-25°N, 20-50°W).

Previous works suggest that the Saharan dust transport over the east Atlantic Ocean is highest during the spring and summer season [*Dunion and Velden*, 2004; *Wang and Liu*, 2014]. Figures 2.2a-d show the quantitative representation of the June-August climatological mean (2003-2012) aerosol loadings over the downstream of the Sahara desert from the MODIS-Aqua, MODIS-Terra, MISR-Terra, and the CALIOP respectively. The AOD distribution patterns are similar in these four datasets despite some disagreements in their magnitudes (e.g., MISR-Terra vs CALIOP). A common feature in these plots are the gradual decrease of the AOD from the west coast of Africa towards the Atlantic Ocean indicating the transport of aerosols from the African continent towards the eastern coast of United States. As the main focus of this study is to examine the dust climatology over the tropical east Atlantic Ocean, we limit out interest to the region where the AOD is relatively higher. Hence, for the further analysis we limit our study domain from 20°-50°W and 0°-25°N, as indicated by the rectangles on figures 2.2a-d.

Time evolutions of the domain averaged (0-25°N, 20-50°W) monthly mean AODs from January 2003 to December 2012 are shown in figure 2.3. The CALIOP measurements generally underestimate the AOD compared to the other measurements, possibly due to its coarser resolution (2° x 5°). The occurrence of the peak AODs are not always consistent among the datasets. However, despite these disagreements the datasets represent the seasonal variations and agree with each other reasonably well. It is evident that the highest aerosol loading mostly occur during the summer months and the lowest in the winter months.

The 10-year mean AOD for individual calendar months indicate (shown in figure 2.4) that the AOD is highest (mean ~ 0.34; taken over all platforms) in July, and lowest (mean ~ 0.18; taken over all platforms) in November.

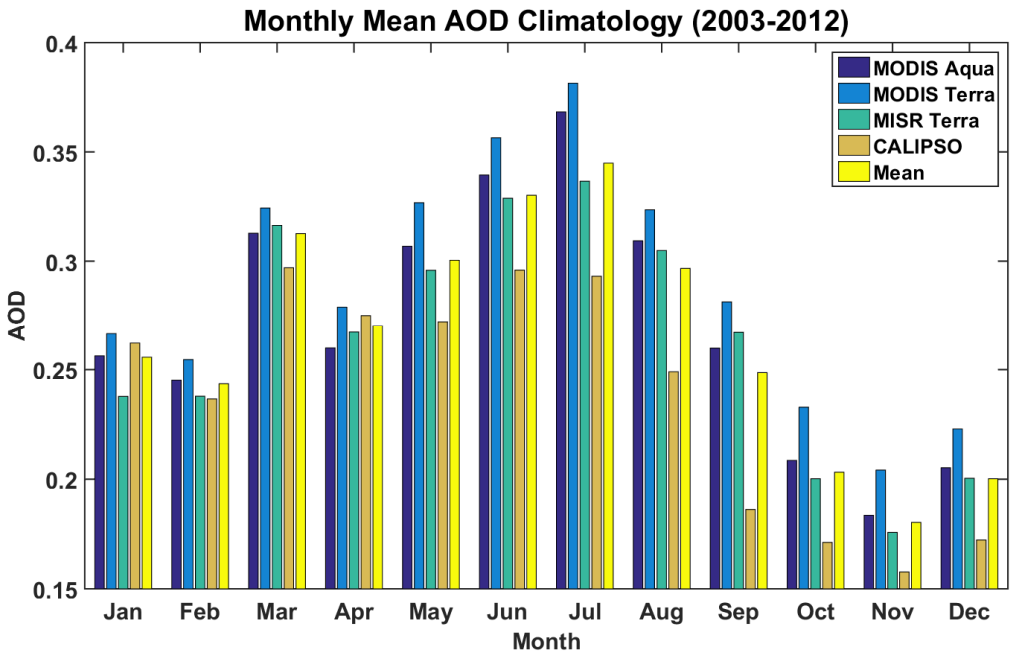

Figure 2.4 Climatological (2003-2012) mean AOD over the domain (0-25°N, 20-50°W) for individual calendar months from the MODIS-Aqua, MODIS-Terra, MISR-Terra, and CALIOP datasets, and their mean.

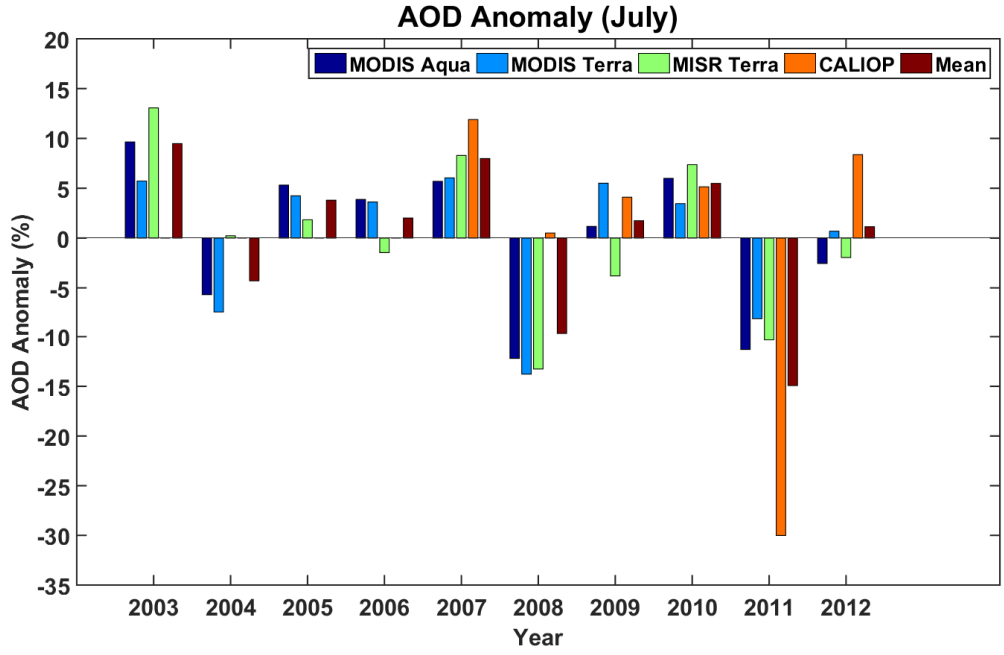

Figure 2.5 Inter-annual variability of the monthly mean AOD anomalies in July (relative to the climatological July mean over 2003-2012) retrieved from the MODIS-Aqua, MODIS-Terra, MISR-Terra, and CALIOP datasets.

We also examine the inter-annual variability of the AOD anomalies in July (relative to the climatological mean AOD in July over 2003-2012). As shown in figure 2.5, the years 2003, 2007, and 2010 had the higher aerosol loadings in July with 10%, 8%, and 7% mean (taken over all platforms) positive AOD anomalies respectively. Lower aerosol loadings in July occurred in the years 2008, and 2011 with mean negative anomalies of 10%, and 15% respectively (figure 2.5).

2.3 Aerosol Characterization over the East Atlantic Ocean

Climatologically, dust is reported to be the primary aerosol species over the east Atlantic Ocean [*Talbot et al.*, 1986; *Dubovik et al.*, 2002]. A recent study by *García et al.* [2017] have also reported that 93% of the total aerosol mass in the SAL is contributed by the dust. However, due to a variety of factors such as the seasonal and annual climate variabilities, contributions of individual aerosol species (including dust) to the total AOD may not be consistent throughout our study period. Therefore, it is essential to verify that AOD variations through 2003-2012 in our domain is indeed due to the Saharan dust aerosols. To do this, we use Aerosol Fine Mode Fraction (FMF) and Angstrom Exponent (AE), in addition to the AOD. FMF and AE, both these parameters are generally used to characterize different aerosol types and also to infer the aerosol size information.

Dubovik et al. [2002] studied the climatology of various aerosol types in several AERONET sites. They found that the desert dust aerosols always show bimodal size distribution which is dominated by the larger dust particles. *Christopher and Jones* [2007] have reported that the annually averaged estimated FMF values for dust are 0.45±0.05. To calculate and compare the individual AODs due to the coarse mode (dust and sea salt) and fine mode (urban and

biomass burning) aerosols we use the FMF and AOD data retrieved from the MODIS-Aqua and MODIS-Terra. Domain averaged AOD's due to coarse and fine mode aerosols are shown in figure 2.6.

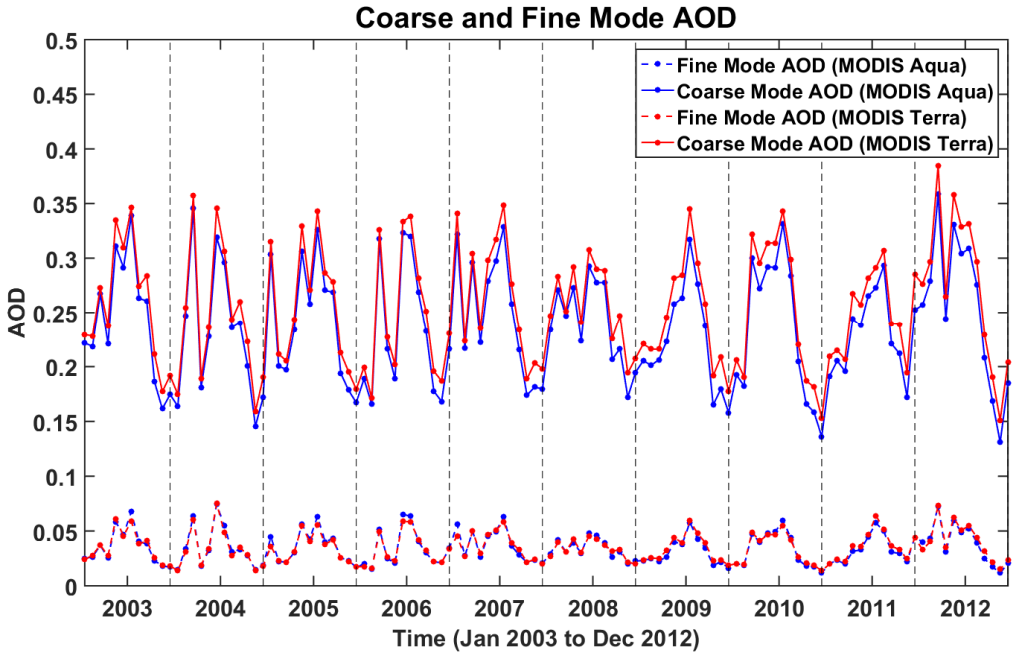

Figure 2.6 Monthly mean coarse mode and fine mode AOD time series averaged over the domain (0-25°N, 20-50°W) for the time period 2003-2012. AODs are calculated from the MODIS-Aqua, and MODIS-Terra FMF, and AOD datasets.

We find that the aerosols in our domain are dominated by the coarse mode particles (coarse mode to fine mode AOD ratio ~ 5) throughout the study period (figure 2.6). This implies that the larger sized dust and sea salt are the prevalent aerosol types in our domain. However, *Dubovik et al.* [2002] suggested that the optical depth of sea salt is much lower compared to the desert dust. For instance, at 440 nm the sea salt AOD does not usually exceed 0.15. While the mean AOD in our domain is found to be mostly higher than 0.15 (figure 2.3) with the dominance of coarse mode AOD (figure 2.6), it can be inferred that this dominance of coarse mode AOD is exclusively linked to the Saharan dust aerosols. Consequently, the AOD

variability through 2003-2012 in our domain effectively reflects the variability in the Saharan dust loading.

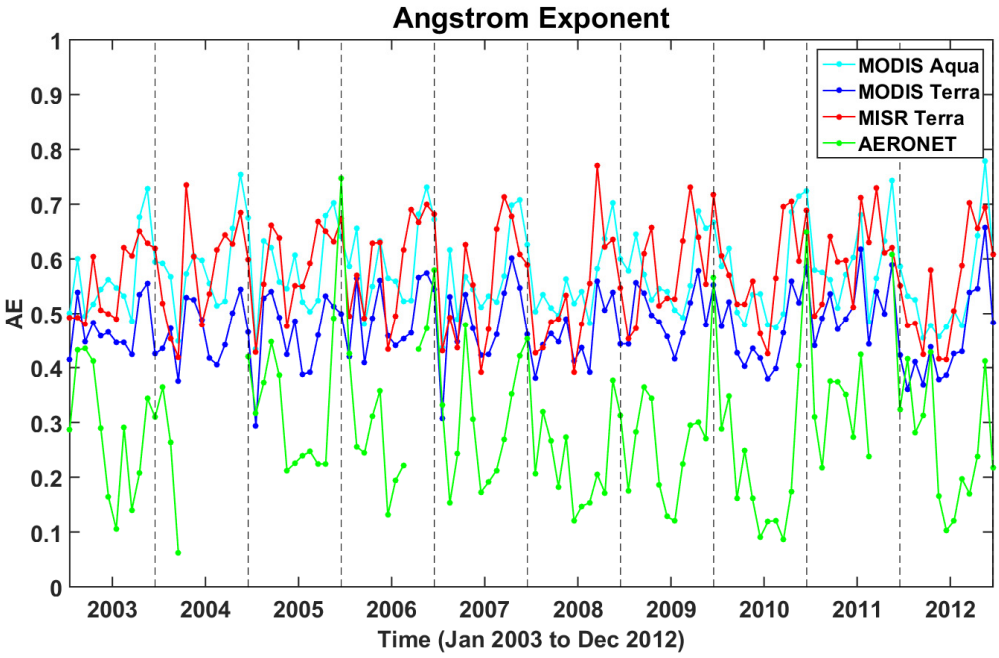

Figure 2.7 Monthly mean Angstrom Exponent (AE) time series averaged over the domain (0-25°N, 20-50°W) for the time period 2003-2012. AE data are taken from the MODIS-Aqua, MODIS-Terra, and MISR-Terra datasets. AERONET AE time series for the Cape Verde Island (16.73°N, 22.94°W) is also shown.

Previous studies have estimated the typical ranges of AE for different aerosol species. Values of AE < 1 indicate the dominance of coarse mode particles that are typically dust or sea salt [*Eck et al.*, 1999; *Dubovik et al.*, 2002; *Schuster et al.*, 2006]. AE time series for 2003-2012, averaged over the domain are shown in figure 2.7. As expected, the AE time series follow the opposite seasonal pattern of the AOD time series (figure 2.3), i.e. lowest in summer and highest in winter. We see that the AE values (figure 2.7) in our domain fall within the range 0.1-0.8 throughout the study period, which correspond to the larger particles. Therefore, from the higher contributions of the coarse mode AOD and lower AE values in the domain we

confirm the dominance of coarse mode dust aerosols over other aerosols in the East Atlantic Ocean throughout 2003-2012.

2.4 Warm and Dry Air Anomalies of the Saharan Air Layer

The Saharan Air Layer (SAL) is associated with warm and dry air anomalies, that influence the tropical convective activities [*Stephens et al.*, 2004; *Wong and Dessler*, 2005]. *Dunion and Velden* [2004] hypothesized that the SAL inhibits convection by enhancing the vertical wind shear and pre-existing trade wind temperature inversion, and also by importing stable and dry air from the Sahara desert. *Wang and Liu* [2014] identified eleven distinctive hot air plumes between May-August in 2007-2008. They reported an increase of environmental temperature up to 2 K at ~ 2 km, that stabilize the air below 2 km while destabilize between 2-5 km. Nevertheless, very few studies are conducted to recognize the potential role of dust particles in the warm and dry nature of the SAL. Based on the numerical simulations *Wong et al.* [2009] investigated the contributions of the Saharan dust in the atmospheric heating over the tropical Atlantic Ocean. The authors concluded that in the east Atlantic Ocean, the dust contributes about 50% of the heating rate anomaly of the SAL. Westward of 40 °W, dust effects are small and the heating rates become more sensitive to the presence of the water vapor. In this section, we attempt to identify the role of dust in maintaining the warm and dry features of the SAL during its transport by analyzing the correlations of the monthly mean AOD anomalies with the tropospheric temperature (T; K) and specific humidity (q; g/kg) anomalies through 2003-2012. If the variability of the temperature and the humidity anomalies vary monotonically with the AOD anomalies, then it can be inferred that the Saharan dust is playing a role in the warmth and dryness of the SAL. However, it should be noted that the strong coupled variations of the dust loading with the temperature and moisture over the east

Atlantic Ocean does not necessarily indicate that dust is the major influencing factor of the SAL's thermodynamic characteristics.

Prior to the analysis of the coupled time evolutions of the AOD with the tropospheric temperature and humidity, we first diagnose the extent of the warming and aridity of the dust-laden SAL during our study period. To do this, we analyze the horizontal distributions of AIRS-Aqua temperature and specific humidity data with the MODIS-Aqua AOD data for the highest dust loading month (July). Climatological (2003-2012) mean AOD distributions in July, along with the temperature (T) and specific humidity (q) fields at 850 hPa are shown in figure 2.8. We see that the AOD maxima (AOD ~ 0.82 at 18.5°N, 20.5°W) is associated with a nearby distinguishable temperature maxima (T ~ 297 K at 21.5°N, 20.5°W) and humidity minima (q ~ 4.4 g/kg at 24.5°N, 20.5°W) in the north eastern part of the domain. Although the temperature maxima and the humidity minima do not exactly coincide with the AOD maxima, their stronger magnitudes with respect to the other parts of the domain suggest that they are possibly associated with the relatively higher dust import through the eastern part of the domain.

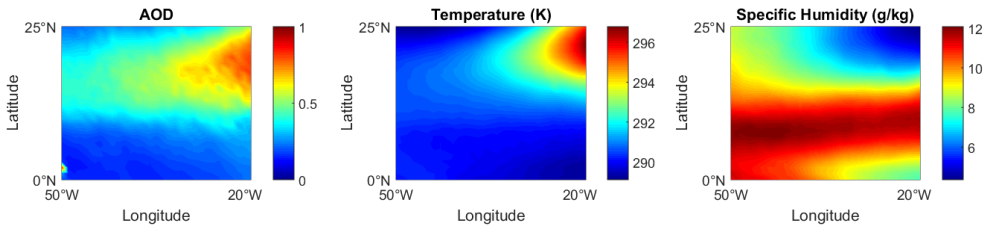

Figure 2.8 Horizontal distributions of July climatological (2003-2012) mean MODIS-Aqua AOD at 550 nm (left panel), AIRS-Aqua temperature (T; middle panel), and AIRS-Aqua specific humidity (q; right panel) at 850 hPa.

To further investigate the east-west temperature and humidity contrasts, vertical profiles of the temperature and humidity in different parts of the domain are examined (figures 2.9a, and 2.10a respectively). Deviation of these profiles from the relevant domain averaged profiles are shown in figures 2.9b, and 2.10b respectively. As there is a significant difference of the east to west dust concentration (e.g., AOD distribution shown earlier; figure 2.8), the entire domain is divided into three longitude bands: 20-30°W (High dust), 30-40°W (Moderate dust), and 40-50°W (Low dust; figures 2.9a-b, and 2.10a-b). The latitude ranges (0-25°N) are the same for all three regions. As expected, the vertical profiles indicate that the mean temperature in the high dust region is higher compared to the mean temperature of the domain (figures 2.9a-b). The maximum warming with respect to the domain mean is ~ +0.7 K that occurs at ~1.4 km (850 hPa; figure 2.9b).

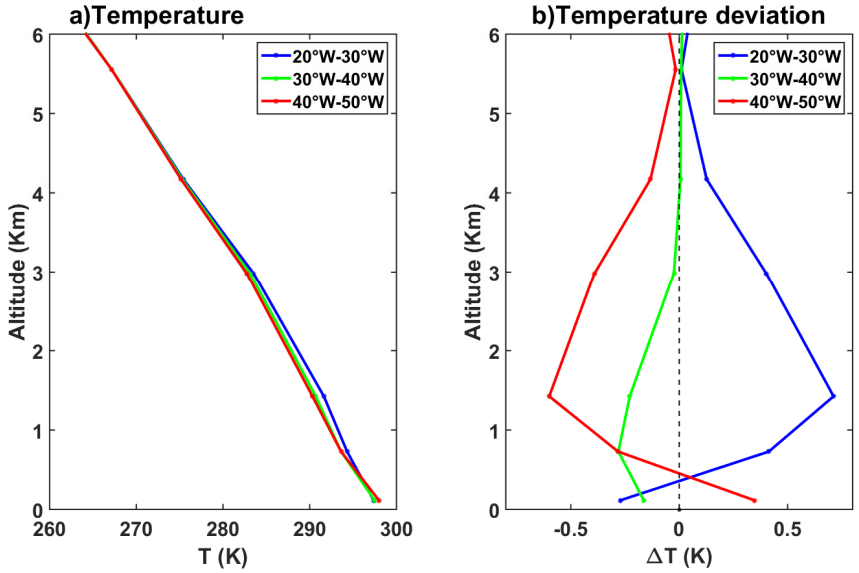

Figure 2.9 Climatological (2003-2012) July mean a) vertical temperature (*T*) profiles in high (0-25°N, 20-30°W), moderate (0-25°N, 30-40°W), and the low (0-25°N, 40-50°W) dust regions of the domain, and the b) deviation of these profiles from the domain averaged profile. Data are taken from the monthly mean AIRS-Aqua dataset.

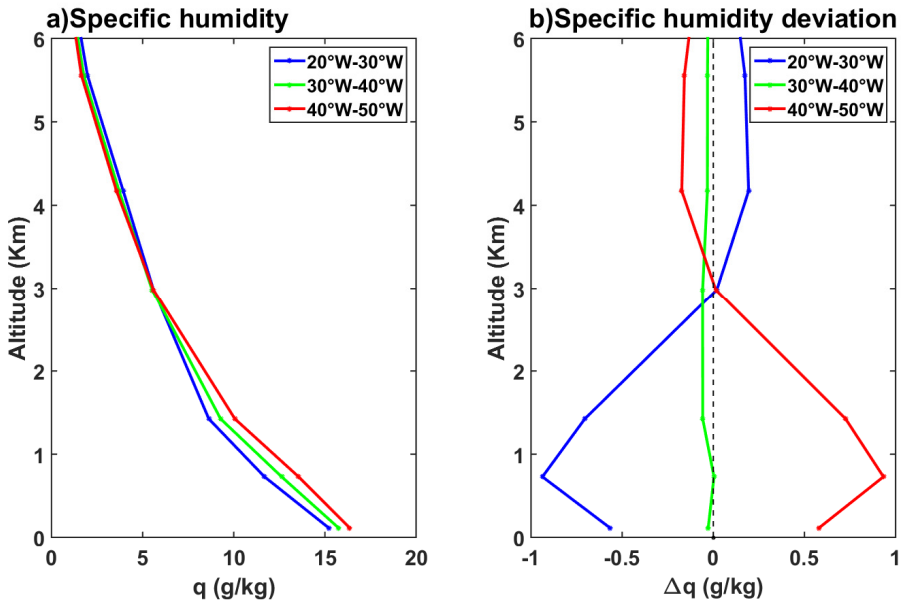

Figure 2.10 Climatological (2003-2012) July mean a) vertical specific humidity (q) profiles in high (0-25°N, 20-30°W), moderate (0-25°N, 30-40°W), and the low (0-25°N, 40-50°W) dust regions of the domain, and the b) deviation of these profiles from the domain averaged profile. Data are taken from the monthly mean AIRS-Aqua dataset.

The humidity profiles also show dry anomaly in the high dust region (Δq ~ -0.9 g/kg) although it is located at ~0.8 km (925 hPa; figure 2.10b). Therefore, the climatological mean data in July suggests that SAL is indeed associated with the warm and dry air anomalies during the study period. Now, the key question is whether the Saharan dust play any role in generating and maintaining these anomalies. To examine this, we look for consistencies in the time series of the AOD anomalies with the temperature and humidity anomalies at every retrieval levels of the AIRS-Aqua dataset. Here we present the time series correlations corresponding to the AIRS-Aqua temperature and humidity data at 850 hPa, and 925 hPa levels respectively. The anomalies are calculated by subtracting the 10 year climatological mean monthly values from the respective individual monthly values. Again, we split the domain into three regions according to the dust abundance as mentioned earlier.

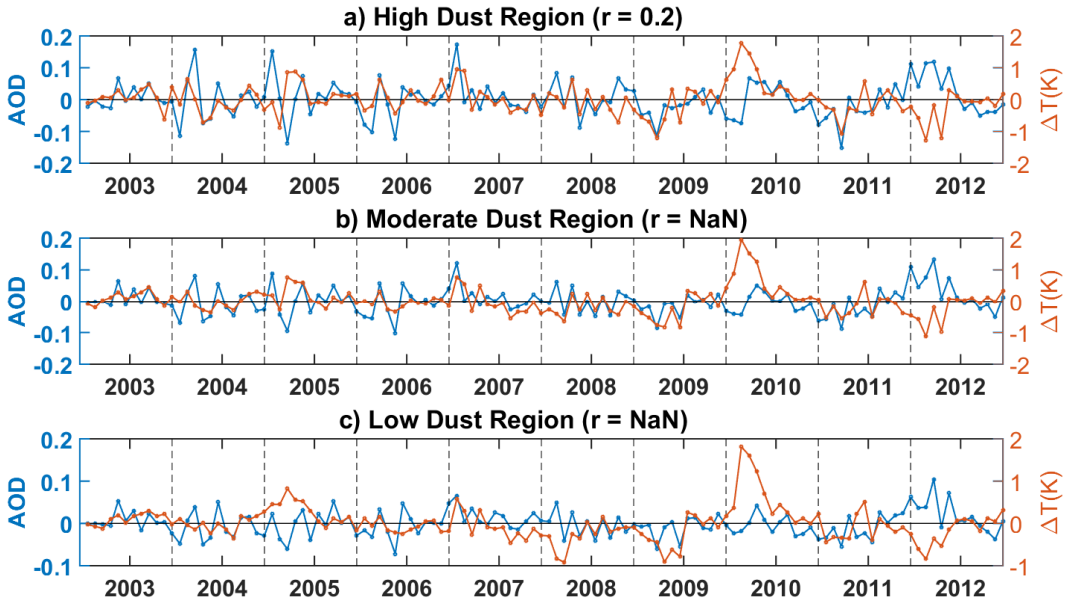

Figure 2.11 Monthly mean anomalies of MODIS-Aqua AOD at 550 nm (blue), and AIRS-Aqua temperature (*T*) at 850 hPa (brown) for a) high (0-25°N, 20-30°W), b) moderate (0-25°N, 30-40°W), and the c) low (0-25°N, 40-50°W) dust regions of the domain during Jan 2003-Dec 2012. Correlation coefficient (*r*) values are shown inside the parentheses, where 'NaN' indicates no statistical significance.

The time series of the AOD and temperature, and the AOD and humidity anomalies are shown in figures 2.11a-c and 2.12a-c respectively. We see that there are no significant correlations of the individual temperature anomalies with the AOD anomalies (figures 2.11a-c). Similarly, the humidity anomalies are also inconsistent with the AOD anomalies although it shows stronger statistically significant (at 95% level) correlations with the AODs (figures 2.12a-c). Nevertheless, the correlation coefficients (*r*) between the time series of these anomalies in all three regions of the domain are very small (largest absolute value of $r \sim 0.42$). Similar results are found for the anomalies calculated at all the pressure levels of the AIRS-Aqua temperature and humidity datasets (figures not shown here). This suggest that either the dust has no contribution to these anomalies or the dust effects are suppressed by other stronger influencing

factor. Advanced statistical techniques are therefore essential to isolate the potential dust effects on the variabilities of these climate fields, which are discussed in the following section.

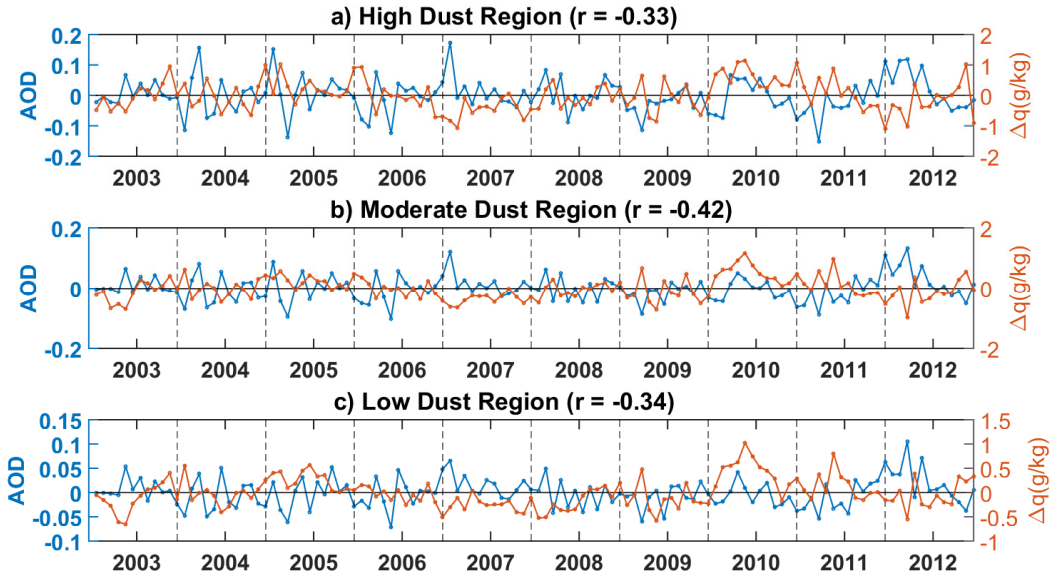

Figure 2.12 Monthly mean anomalies of MODIS-Aqua AOD at 550 nm (blue), and AIRS-Aqua specific humidity (q) at 925 hPa (brown) for a) high (0-25°N, 20-30°W), b) moderate (0-25°N, 30-40°W), and the c) low (0-25°N, 40-50°W) dust regions of the domain during Jan 2003-Dec 2012. Correlation coefficient (r) values are shown inside the parentheses.

2.5 Statistical Analysis of the Climate Data

In this section we use two statistical methods to analyze the spatiotemporal variabilities of the climatological dust loading, atmospheric temperature, and the moisture anomalies over the tropical east Atlantic Ocean. The methods used in our analysis are: the Empirical Orthogonal Function (EOF) and the Singular Value Decomposition (SVD). Both these techniques follow similar computational procedures which can be found in *Bjornsson and Venegas* [1997]. While the EOF analysis is primarily used for isolating the spatial and temporal variability patterns of an individual data field, the SVD is used to identify the coupled variability of two climate variables. As in the analysis of the previous section, here we perform the statistical

analysis (EOF and SVD) on the monthly mean AOD (550 nm) data from MODIS-Aqua, and temperature (T) data at 850 hPa and specific humidity (q) data at 925 hPa from the AIRS-Aqua measurements over 2003-2012.

2.5.1 Empirical Orthogonal Function (EOF) Analysis

The Empirical Orthogonal Function (EOF) decomposition separates the spatiotemporal climate data into a sum of orthogonal variability modes. This technique has been widely used to examine the variability of different isolated climate variables, which can also be extended to examine coupled fields. Here we use both the single and coupled EOF decomposition of the AOD, T, and q fields in our domain to examine whether the warm and dry anomalies of the SAL is linked to the Saharan dust. To perform the EOF analysis, the seasonal trends of these data fields are removed by subtracting the respective climatological mean values in each month. Each decomposition mode of the EOF analysis represents a fraction of the total variance of the data and is composed of eigenvectors (or EOFs) and Principal Components (PCs). While the EOF patterns represent the spatial distribution of the data variability, the PC time series represent the time evolutions of these EOFs. In our case we retain with the first three variability modes of the EOF analysis for each of the three climate variables. All the EOF fields and the PC time series shown in the following are normalized with respect to the relevant largest (absolute) values.

First, we perform the EOF analysis of the individual AOD, temperature, and humidity fields for isolating the spatial and temporal variability of these variables. Figures 2.13a-c show the AOD EOFs for the three leading decomposition modes respectively. The three leading mode

principal component time series associated with these EOFs are shown in figures 2.14a-c respectively.

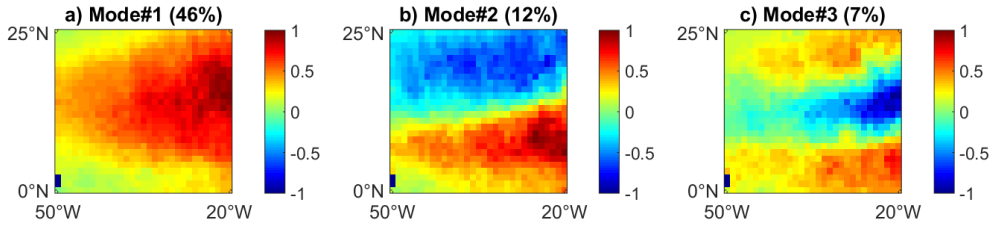

Figure 2.13 EOF patterns of the a) 1st, b) 2nd, and c) 3rd modes of AOD decomposition. Abscissa and ordinate represent the longitude and latitude respectively. The amplitudes are normalized by the largest (absolute) value corresponding to each mode. AOD data are taken from the monthly mean AODs at 550 nm from the MODIS-Aqua dataset over 2003-2012. Fraction of the total variance for each mode are shown inside the parentheses.

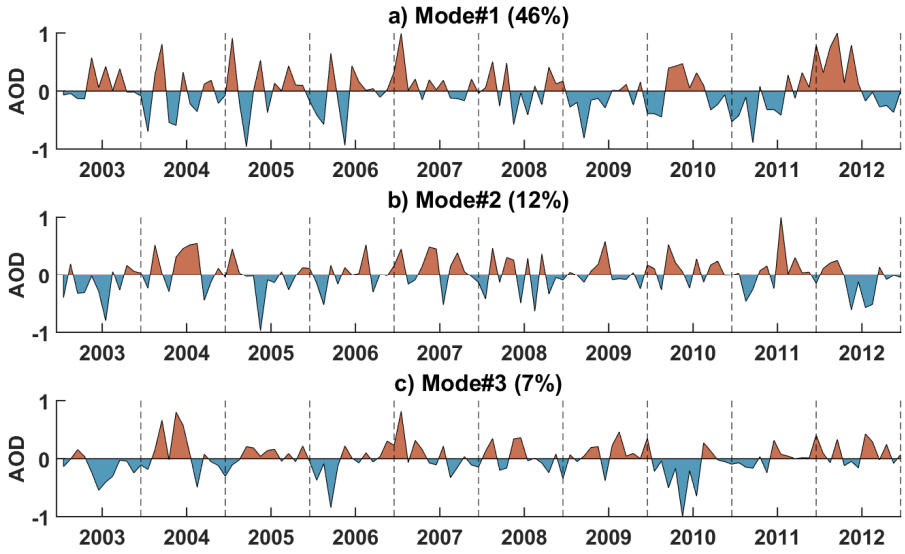

Figure 2.14 Principal Component (PC) time series of the a) 1st, b) 2nd, and c) 3rd modes of AOD decomposition. The amplitudes are normalized by the largest (absolute) value corresponding to each mode. AOD data are taken from the monthly mean AODs at 550 nm from the MODIS-Aqua dataset over 2003-2012. Fraction of the total variance for each mode are shown inside the parentheses.

The first three variability modes contribute ~ 66% of the total AOD variance. Most of the AOD variability in the 1st mode (representing ~ 46% of the total variability) occur in the eastern part of the domain where the dust laden SAL enters the domain (figure 2.13a). The

time series of the first PC shows large interannual variability of dust with no definite trends (figure 2.14a). It is evident that year 2010 had positive dust anomaly, although the amplitude of the anomaly is weaker than the anomaly in year 2012. The 2nd EOF mode representing ~ 12% of the total variance have both positive and negative amplitudes which dominate the south eastern and north eastern part of the domain respectively (figure 2.13b). This mode is clearly characterizing the variability of the SAL's trajectory over the Atlantic Ocean due to the local climate variability. Similar to the 1st PC time series, time evolutions of the 2nd and 3rd PCs do not indicate any noticeable trend (figures 2.14b-c).

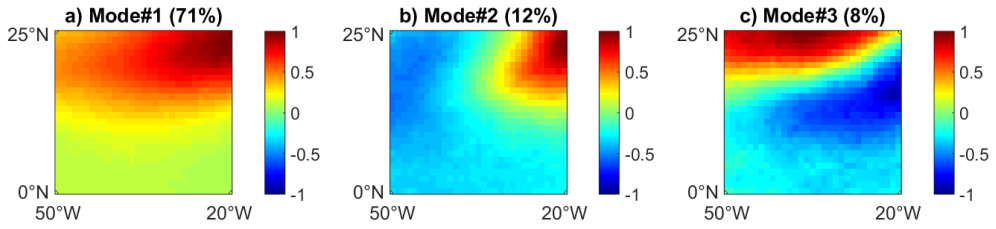

Figure 2.15 Same as figure 2.13, but for the temperature (*T*). The temperature data are taken from the monthly mean temperature at 850 hPa from the AIRS-Aqua dataset over 2003-2012.

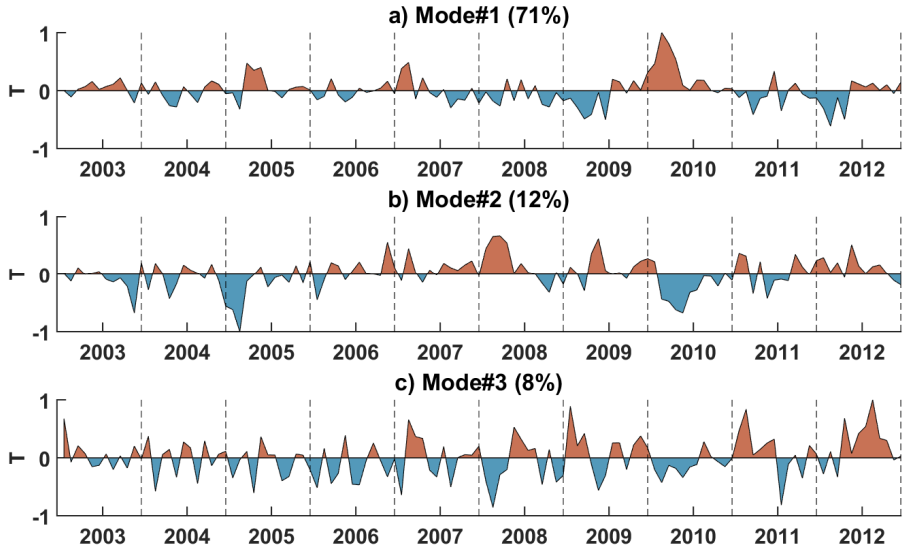

Figure 2.16 Same as figure 2.14, but for the temperature (*T*). The temperature data are taken from the monthly mean temperature at 850 hPa from the AIRS-Aqua dataset over 2003-2012.

The EOF patterns, and the associated PC time series corresponding to the three leading modes of the EOF decomposition of the temperature (*T*) field are shown in figures 2.15a-c and figures 2.16a-c respectively. These three variability modes contribute ~ 91% to the total temperature variability. The temperature variabilities are strongly concentrated in the north eastern corner of the domain (1st and 2nd EOF patterns; figure 2.15a-b). These maxima are not exactly collocated with the AOD variability maxima mentioned earlier (figure 2.13a). The 1st principal component time series shows a pronounced and persistent warming anomaly in 2010 (figure 2.16a). The EOF analysis of the temperature fields at other AIRS retrieval levels are also examined. The EOF patterns and the PC time series of the temperature fields at other levels are not exactly same as the 850 hPa level (figures not shown here). However, they have some common features (e.g., warming anomaly in 2010).

EOFs and PCs from the EOF analysis of the specific humidity (*q*) data are presented in figures 2.17a-c and 2.18a-c respectively. First three leading EOF modes explain ~ 73% of the total moisture variance. The spatial pattern of the 1st EOF mode, which accounts for 54% of the total variance is characterized by only the increase of the moisture (maxima centered at ~ 13 ° N and 25 ° W; figure 2.17a) and resembles the 1st EOF pattern of the AOD (figure 2.13a). The 2nd and 3rd EOF modes show both increment and decrement of the humidity (figures 2.17b-c). We notice that the *q* EOF minima at the north eastern corner of domain in the 2nd EOF pattern (figure 2.17b) is very similar (with opposite sign) to the temperature EOF maxima corresponding to the 1st and 2nd variability modes (figures 2.15a-b). This indicates that both of these variability extremes are coupled together. The PC time series associated with the three leading modes show clear positive anomaly of *q* in year 2010 (figures 2.18a-c).

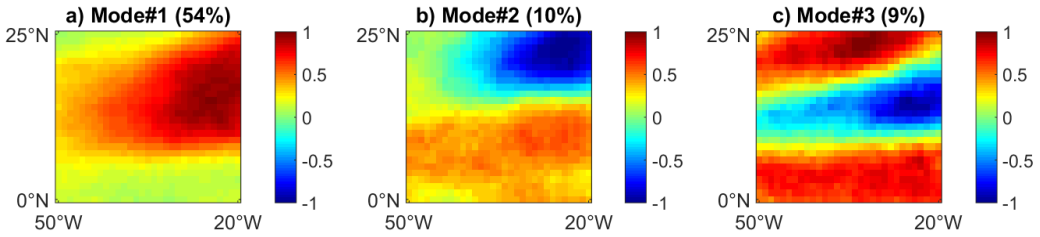

Figure 2.17 Same as figure 2.13, but for the humidity (q). The humidity data are taken from the monthly mean specific humidity at 925 hPa from the AIRS-Aqua dataset over 2003-2012.

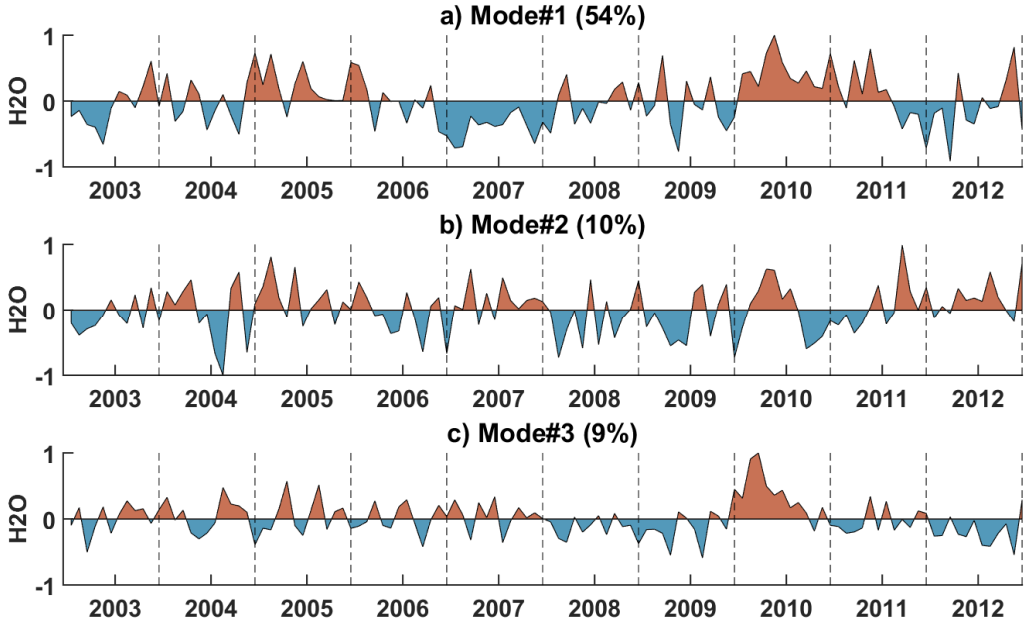

Figure 2.18 Same as figure 2.14, but for the humidity (q). The humidity data are taken from the monthly mean specific humidity at 925 hPa from the AIRS-Aqua dataset over 2003-2012.

We now extend the EOF analysis to investigate the paired variability of the data fields, i.e. the AOD-T, and AOD-q anomaly fields. To do this, we generate correlation maps by computing the correlations (r) between the time series of the anomaly of one field [so called left data field; e.g., *Bretherton et al.*, 1992] at each grid point and the principal components from the EOF decomposition of another field (right data field). As our goal is to find the potential dust

effects on T and q, in our case the left field is the detrended AOD anomaly field, and the right data fields are the PCs of either the T, or q field.

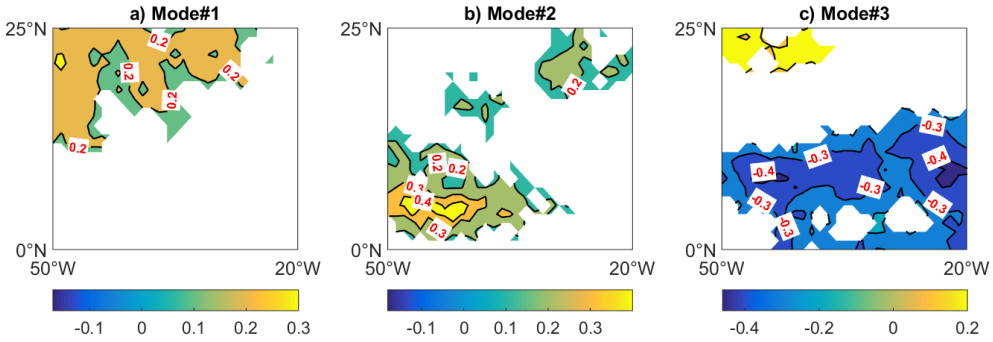

Figure 2.19 Correlation maps between the time series of grid point AOD anomalies (left data field) and the principal components of the temperature (right data field) corresponding to the a) 1st, b) 2nd, and c) 3rd modes of EOF decomposition of temperature. Abscissa and ordinate represent the longitude and latitude respectively. The temperature data are taken from the monthly mean temperature at 850 hPa from the AIRS-Aqua dataset over 2003-2012. Only the statistically significant values (at 95% confidence level) are shown on the map.

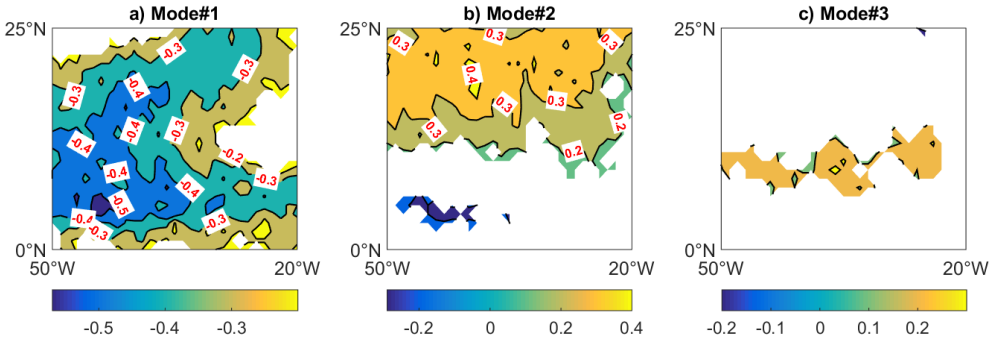

Figure 2.20 Same as figure 2.19, but for the correlations between the grid point AOD anomalies (left data field) and the principal components of the humidity (q; right data field). The humidity data are taken from the monthly mean specific humidity at 925 hPa from the AIRS-Aqua dataset over 2003-2012.

Figures 2.19a-c and 2.20a-c show the correlation patterns (heterogeneous correlation map) between the AOD anomaly field and the three leading principal components of T and q respectively. Only the statistically significant values (at 95% significant level) are shown on

the map. In general, for both variables the magnitudes of the correlations are very weak (strongest value of $r \sim 0.5$) and limited to a very small part of the domain. The maximum positive (warming) correlation between AOD and T is +0.4, which is centered at the south western part of the domain and corresponds to the 2nd variability mode of temperature (figure 2.19b). Negative (cooling) correlations ($r \sim -0.4$) are present in the southern half of the domain, associated with the 3rd variability mode (figure 2.19c). Similarly, the strongest correlation between the dust and humidity data fields is -0.5 which is also at the south western part of the domain, but it is associated with the 1st variability mode of the humidity (figure 2.20a).

Therefore, based on EOF analysis of the coupled fields we infer that the Saharan dust cannot be considered as the primary cause of the warming anomaly of the SAL as the AOD-T correlation is not very strong ($r < 0.4$) and also because it occurs in the 2nd and 3rd variability modes. In contrast, the humidity variations in the southwest part of the domain shows better coupled variations with the dust anomalies as it occurs in the 1st variability mode and also because the correlation is relatively stronger ($r \sim -0.5$).

2.5.2 Singular Value Decomposition (SVD) Analysis

The Singular Value Decomposition (SVD) technique is used to analyze the coupled variabilities of two climate variables. In this section we use the SVD analysis of the climatological AOD, T, and q data to further examine whether the variations of the dust loading, temperature, and moisture are linked to one other. In contrast to the single field EOF analysis, the SVD analysis identifies only those modes of variability where two data fields are strongly coupled [e.g., *Bjornsson and Venegas*, 1997]. Results of the SVD analysis include the eigenvectors (spatial patterns) and the expansion coefficients consisting of several paired

variability modes, where each mode represents a fraction of the covariance between the two fields (Squared Covariance Fraction; SCF). Here we perform two separate pairs of SVD analysis: AOD-*T*, and AOD-*q*. Prior to the SVD analysis, the seasonal trends of the data are removed by subtracting the respective climatological monthly mean values.

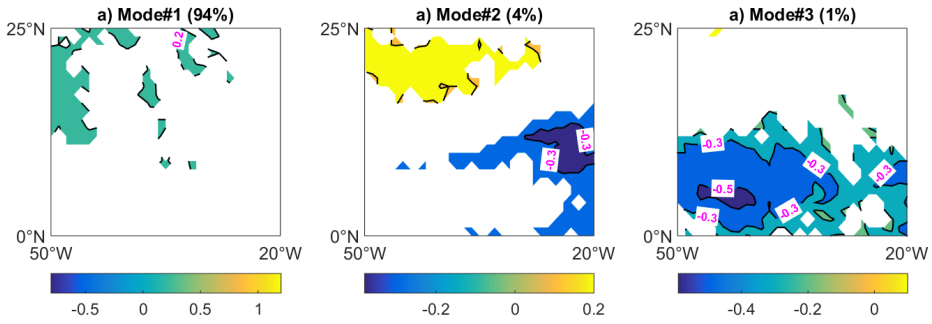

Figure 2.21 Heterogeneous correlation maps between the coupled SVD decomposition of AOD (left data field) and temperature (right data field) corresponding to the a) 1st, b) 2nd, and c) 3rd modes. Abscissa and ordinate represent the longitude and latitudes respectively. The temperature data are taken from the monthly mean temperature at 850 hPa from the AIRS Aqua dataset over 2003-2012. Only the statistically significant values (at 95% confidence level) are shown on the map. The Squared Covariance Fraction (SCF) values are shown inside the parentheses.

SVD analysis of the AOD-*T* shows that the three leading SVD modes of the coupled AOD and temperature variations represent ~99% of the total squared covariance. The spatial patterns of the individual fields are very similar to those found in the EOF analysis, therefore not shown here. The heterogeneous correlation maps between the AOD anomalies in individual grid cells and the temperature expansion coefficients from the first three modes are shown in figures 2.21a-c. As in the case of the coupled EOF analysis, we find no significantly strong correlations except the minima at the southwest part of the domain where the correlation reaches up to -0.5 and associated with the 3rd mode (figures 2.21c).

However, this mode only represents 1% of the total paired variability, suggesting that correlations are limited to only few grid cells.

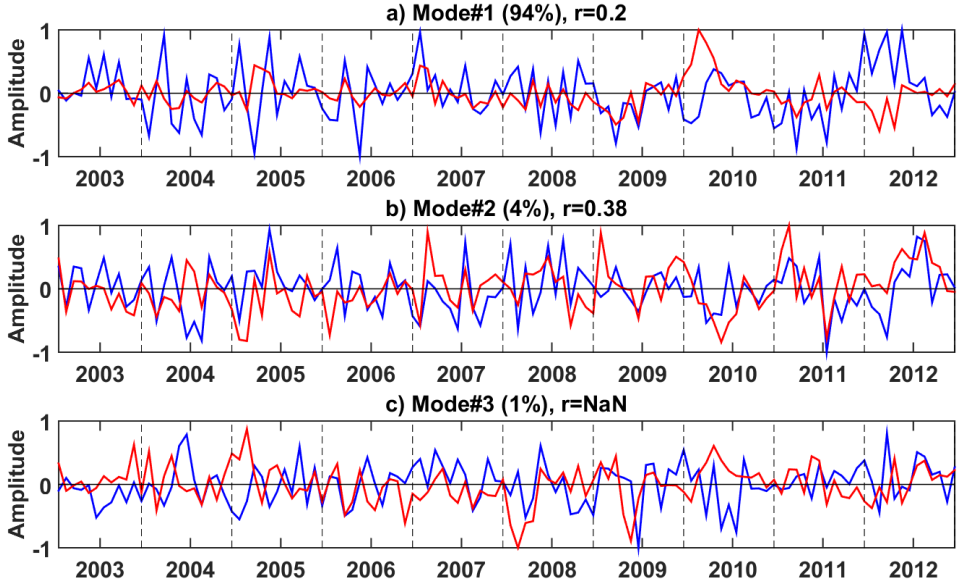

Figure 2.22 Time evolutions of the expansion coefficients of AOD (blue) and temperature (red) from the SVD analysis of AOD-T corresponding to the a) 1st, b) 2nd, and c) 3rd modes. The amplitudes are normalized by the largest (absolute) value corresponding to each mode. The Squared Covariance Fraction (SCF) values are shown inside the parentheses. Correlation coefficients (*r*) are also shown, where 'NaN' indicates no statistical significance.

We also investigate the temporal correlations of these two fields by comparing the time series of the expansion coefficients. Time evolutions of the expansion coefficients of AOD and *T* from the three leading modes of SVD analysis are shown in figures 2.22a-c respectively. We see that the expansion coefficients of AOD and *T*, for most part of the study period do not have good correlations. However, there are some occurrences where they vary in similar fashion (e.g., years 2005 and 2012; figure 2.22b). Similar correlations are also conducted by the permutation-combination of different modes of the expansion coefficient time series of AOD and *T*. Results are presented in table 2.2, which suggests that none of the first three modes of these two fields are strongly correlated to one another. However, we notice that there

are more likelihood of positive AOD-*T* correlations at 850 hPa and 925 hPa levels (table 2.2), indicating the association of warm anomaly with the SAL. The maximum positive correlation is between the expansion coefficients of AOD in 3rd mode and *T* in 2nd mode ($r = +0.39$).

Table 2.2 Correlation coefficients (at 95% confidence level) between the expansion coefficients associated with different modes of the coupled SVD decomposition of AOD (left field) and atmospheric temperature (right field) in the first six AIRS retrieval levels.

Level (hPa)	1-1	2-2	3-3	1-2	2-3	3-1	2-1	3-2	1-3
1000	-	-	-	-	-	-	-	-	-
925	0.23	0.3	-	-	0.33	-	-	0.39	-
850	0.2	0.38	-	-	0.36	-	-	0.32	-
700	-	-	-0.22	-	-	-	-	-	-
600	-0.32	-	-0.19	-0.19	-	-	-	0.19	-
500	-0.27	-	-	-0.4	-	-	-	-	-

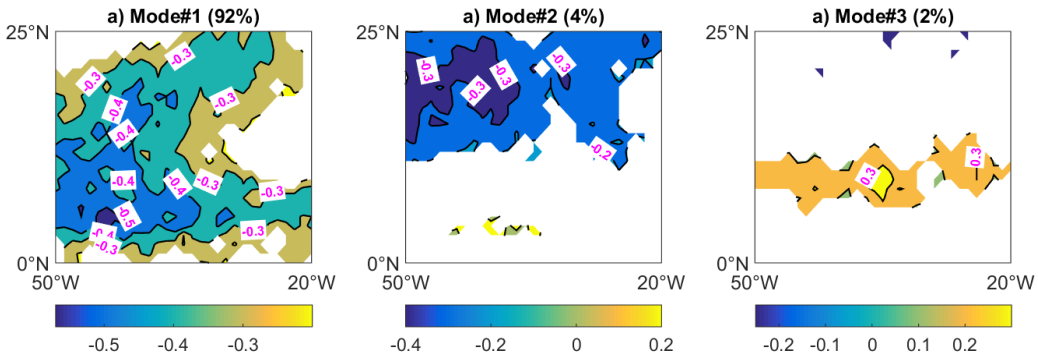

Figure 2.23 Same as figure 2.21, but for the coupled SVD decomposition of AOD (left data field) and specific humidity (right data field). The specific humidity data are taken from the monthly mean specific humidity at 925 hPa from the AIRS-Aqua dataset over 2003-2012.

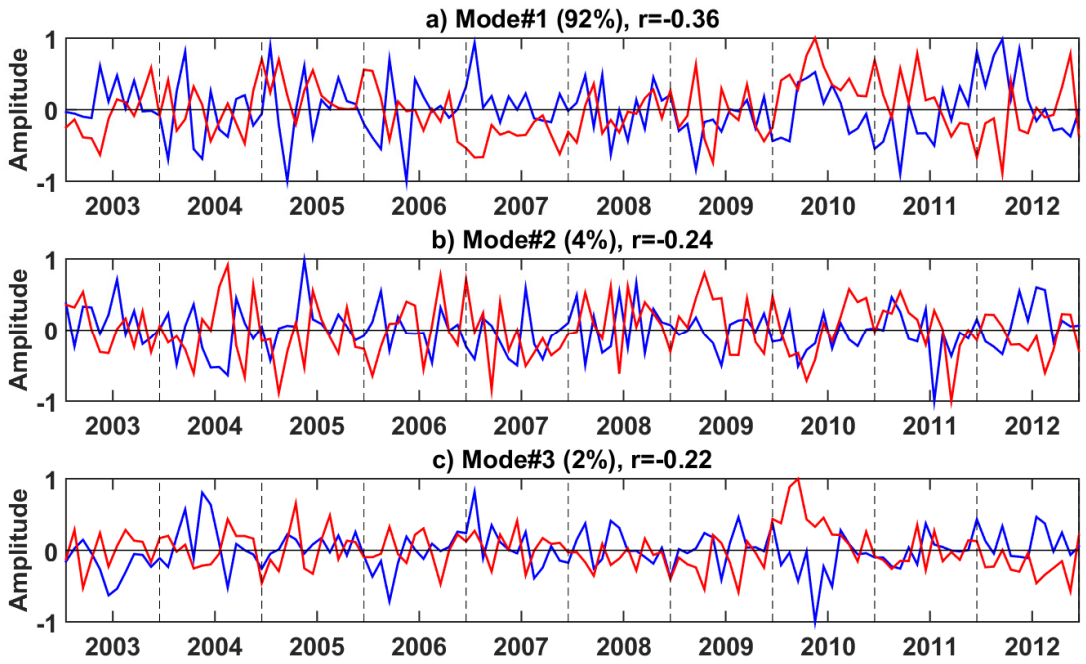

Figure 2.24 Same as figure 2.22, but for the coupled SVD decomposition of AOD (blue) and the specific humidity (red). The specific humidity data are taken from the monthly mean specific humidity at 925 hPa from the AIRS-Aqua dataset over 2003-2012.

Following the similar procedures of the SVD analysis of AOD-*T*, we also compute the SVD analysis of AOD and *q* fields. The Heterogeneous correlation maps and the time series of the expansion coefficients from the first three modes of the SVD analysis of AOD-q are shown in figures 2.23a-c and 2.24a-c respectively. We see that the AOD and humidity are negatively correlated in the south western part of the domain (strongest correlation is -0.5; figure 2.23a), which is consistent with the findings from the EOF analysis. Temporal correlations between the expansion coefficients of AOD and *q* also show negative AOD-*q* relationship in some portion of the study period (e.g., year 2012; figure 2.24a). As shown in table 2.3, the negative AOD-*q* correlations are mostly at 925 hPa levels, indicating the association of dry air anomaly with the SAL.

Table 2.3 Same as table 2.2, but the expansion coefficients are associated with the SVD decomposition of AOD (left field) and specific humidity (right field).									
Level (hPa)	1-1	2-2	3-3	1-2	2-3	3-1	2-1	3-2	1-3
1000	-0.3	-	-	-	0.22	0.29	-	-	-0.31
925	-0.36	-0.24	-0.22	-0.24	-0.36	-0.37	-	-	-
850	-	-	-	-	-0.25	-0.23	-	0.21	-
700	0.19	-	-	-	-	-	-	0.31	-
600	0.27	0.18	-	-	-0.23	-	-	-0.32	-
500	0.29	-	-	-	-0.20	-	-	-0.33	-

Based on both the coupled EOF and SVD analysis we find no strong impact of the Saharan dust on the temperature anomalies of the SAL. On the other hand, both EOF and SVD analysis show a moderately strong (~ -0.5) negative effect of dust on the moisture which is only limited to a small region downstream of the SAL's track (south western part of the domain). However, for the entire domain as a whole there are no strong statistically significant coupled variations of AOD-*T*, and AOD-*q* during 2003-2012. This suggest that possibly dust have no role in the thermodynamic features (warm and dry anomalies) of the SAL, or the dust effects are very small in longer time scale which are not distinguishable due to other stronger contributing factors, such as the presence of the Intertropical Convergence Zone (ITCZ) or the influence of the African Easterly Wave (AEW). Controlled numerical simulation experiments are therefore necessary to identify any potential dust effects on tropical east Atlantic climate variables. A number of simulation experiments are conducted by varying the dust

concentration in different model configurations simulating various type of dust effects. The model configurations and results of these experiments are discussed in the following chapters.

Chapter 3: Numerical Model Description and Validation

3.1 Model Description

To investigate the effects of the Saharan dust aerosols on temperature and humidity profiles over the tropical East Atlantic Ocean, we perform several model simulation experiments. We also use the model data to study the dust impacts on the radiation budget and cloud microphysics. In this chapter we present a brief description of the model, major parameterization schemes of the model, simulation configurations, and the evaluation of the model output data. The numerical model used for the simulations is the Weather Research and Forecasting model (WRF) coupled with Chemistry module [WRF-Chem; *Grell et al.*, 2005]. WRF [*Skamarock et al.*, 2008] is a fully compressible, nonhydrostatic mesoscale modeling system designed for both weather research and forecasting needs. It is developed by the collaboration of several research organizations including the National Center for Atmospheric Research (NCAR) and National Oceanic and Atmospheric Administration (NOAA) among others. The model has two dynamic solvers: Advanced Research WRF (ARW) and the Nonhydrostatic Mesoscale Model (NMM). Current study employs the ARW solver. Prognostic variables in WRF include the horizontal and vertical wind velocities, perturbation potential temperature, perturbation geopotential height, perturbation surface pressure of dry air, hydrometeor mixing ratios of water vapor, cloud water, rain, and the cloud droplet number concentration.

WRF-Chem, a version of WRF is a fully coupled meteorology-chemistry-aerosol model that simulates the trace gases and aerosols simultaneously with the meteorological fields of the

native WRF model. Online chemistry module was first implemented in WRF by *Grell et al.* [2005]. Current study uses the WRF-Chem version 3.6.1 (WRF-Chem hereafter) which was released in August, 2014. Both chemistry and meteorology components of the model use the same model grid, model dynamics, and also the sub-grid scale transport parameterization scheme [*Grell et al.*, 2005]. In addition to the prognostic WRF variables, prognostic variables in WRF-Chem includes various chemical species and tracers particular to the choice of the chemistry module. This makes the WRF-Chem computationally more expensive than the meteorology-only run. Nevertheless, representation of the radiative and microphysical processes that interacts with aerosol processes (e.g. wet scavenging) is essential for studying the direct and indirect effects of aerosols.

3.2 Model Configuration

Table 3.1 Summary of the physical parameterization schemes used in this study.

Atmospheric Process	Scheme	Reference
Planetary Boundary Layer	MYNN	[*Nakanishi and Niino*, 2006]
Surface Layer	Unified Noah LSM	[*Chen and Dudhia*, 2001]
Sub grid scale Cloud Physics	Grell 3D	[*Grell and Dévényi*, 2002]
Grid scale Cloud Microphysics	Morrison double moment	[*Morrison et al.*, 2005, 2009]
Shortwave Radiation	RRTMG	[*Iacono et al.*, 2008]
Longwave Radiation	RRTMG	[*Iacono et al.*, 2008]
Gas phase Chemistry	RADM2	[*Stockwell et al.*, 1990]
Aerosol Chemistry	MADE-SORGAM	[*Ackermann et al.*, 1998; *Schell et al.*, 2001]

The major physical and chemical parameterization schemes used in the model simulations for the present study are listed in Table 3.1. Detailed descriptions of these schemes are discussed in the literatures given in the reference column. Below, we briefly discuss the schemes relevant to the cloud-aerosol-radiation interactions.

3.2.1 Aerosol Model: MADE-SORGAM Scheme

Mineral dust aerosols consist of irregular particle shapes with sizes varying from tenths of nanometers to hundreds of microns [*Formenti et al.*, 2011]. Due to this wide size spectrum, representation of the dust size distribution in numerical models is a challenging task. Nevertheless, the size distributions of dust particles are usually represented by either multiple size modes or size bins [*Huneeus et al.*, 2011]. Compromising both the accurate representation of dust and the computational cost of the simulations, for the current study we use the modal size distribution of dust particles. The aerosol module coupled with the WRF model for this study includes the Modal Aerosol Dynamics Model for Europe [MADE; *Ackermann et al.*, 1998] for the inorganic aerosols, and the Secondary Organic Aerosol Model [SORGAM; *Schell et al.*, 2001] for the organic aerosols. The MADE-SORGAM aerosol module uses the modal approach of the aerosol size distributions with three size modes (atiken, accumulation and coarse mode) assuming a log-normal size distribution for each mode:

$$\frac{dN}{d(\ln D_p)} = \frac{N}{\sqrt{2\pi}\ln\sigma_g}\exp[-\frac{(\ln D_p - \ln D_g)^2}{2\ (\ln\sigma_g)^2}]$$

where, N is the particle number concentration, D_p is the particle diameter, D_g is the median diameter, and σ_g is the standard deviation of the distribution. All particles in a particular size mode is assumed to be internally mixed i.e. have the same chemical composition. The aerosol

species treated in this scheme include the main inorganic ions (sulfate, nitrate, and ammonium), elemental carbon (EC), organic matter (OM; primary and secondary), aerosol water, sea salt and mineral dust. The mass conservation equations used to predict the aerosol distributions follow those of the gas phase species with additional terms for the aerosol dynamics. Sources of the aerosols include the direct particle emission and the secondary formation by nucleation. Other physical processes that contribute to the aerosol population are the condensation, coagulation, aqueous phase chemistry, water uptake by aerosols, and dry and wet deposition. Dry deposition and sedimentation velocities are calculated for each mode separately which are based on *Binkowski and Shankar* [1995]. Wet deposition of aerosols by grid scale precipitation is simulated by *Easter et al.* [2004].

3.2.2 Radiation: RRTMG Scheme

Rapid Radiative Transfer Model for General Circulation Model [RRTMG; *Iacono et al.*, 2008] is used in the current study to account for both longwave and shortwave radiative effects. RRTMG calculates the radiative fluxes and atmospheric heating rates for 16 longwave bands (LW; 3.08-1000 μm), and 14 shortwave bands (SW; 0.2-12.2 μm). It provides the top of the atmosphere and the surface radiative fluxes for both clear sky and all sky conditions. RRTMG also includes the interaction of radiation with cloud, rain, ice, and snow. Optical properties of water and ice clouds are calculated from the parameterizations based on *Hu and Stamnes* [1993], and *Fu et al.* [1998] respectively. Cloud droplet number concentration and cloud water mass mixing ratio are used to calculate the cloud effective radius, which is then used to determine the cloud optical depth. Aerosol optical properties are calculated in a separate module using the Mie theory, and then passed onto the RRTMG radiation module [*Fast et al.*, 2006]. These optical properties are calculated at the midpoint of each of the four different

shortwave bands (covering the spectrum: 400 nm-1000 nm) and sixteen longwave bands (covering the spectrum: 10 cm^{-1}-3250 cm^{-1}). Mie theory calculates the extinction efficiency (Q_e), scattering efficiency (Q_s), and the asymmetry parameter (g) at each grid cell for a particular wavelength (λ), and size parameter ($x_i = 2\pi r_i/\lambda$) of each of the size mode ($i = 1 - 3$ for the MADE-SORGAM). The net optical properties are then determined by the summation over all three size bins. For instance, the aerosol extinction co-efficient, $\beta_e(\boldsymbol{x}, \lambda)$ which is calculated as a function of three dimensional position ($\boldsymbol{x}$) and wavelength (λ), is given by:

$$\beta_e(\boldsymbol{x}, \lambda) = \sum_{i=1}^{i=3} Q_e(x_i, \boldsymbol{x}, \lambda)\, \pi {r_i}^2 n(r_i, \lambda)$$

where, $Q_e(x_i, \boldsymbol{x}, \lambda)$is the extinction efficiency, r_i is the wet particle radius, and $n(r_i, \lambda)$ is the prognostic number concentration of the aerosol. The total optical depth (τ) at particular grid cell is obtained by integrating the extinction efficiency from the lowest model level (z_0) to the top level (z_{top}):

$$\tau(\lambda) \cong \sum_{k=z_0}^{k=z_{top}} \beta_e(k, \lambda)\, \Delta z$$

where, Δz is the altitude difference between two consecutive model half-levels associated with the *k*-th model level. Detailed descriptions of the calculation of aerosol optical properties in WRF-Chem can be found in *Fast et al.* [2006] and *Barnard et al.* [2010].

For this study, we choose the volume averaged mixing rule that assumes internal mixing of aerosol composition and calculates the refractive indices for each size modes from the refractive indices of individual aerosol species. Most of the refractive indices for the aerosol species are adapted from the National Centre for Atmospheric Research Community

Atmosphere Model (CAM). However, unlike the CAM model, the real and imaginary part of the refractive indices for the dust used for our experiments are 1.55 and 0.003 respectively for all four shortwave wavelengths which are based on *Zhao et al.* [2010]. The longwave refractive indices varied from 1.242 - 2.904 for the real part and 0.0068-0.857 for the imaginary part. However, it should be noted that currently aerosol LW scattering is not implemented in the RRTMG module, and therefore only the aerosol LW absorption is considered in the radiative transfer calculations.

3.2.3 Cloud Microphysics: Morrison Scheme

Cloud microphysics scheme simulates the physical processes controlling the formation of the cloud droplets and ice crystals. There are several cloud microphysics options available in WRF-Chem, however currently the Lin scheme [*Lin et al.*, 1983], and Morrison scheme [*Morrison et al.*, 2009] are capable of simulating the cloud-aerosol interactions. In the beginning of this research project Lin scheme was used for all of our simulations. However, for all of the latest simulation experiments, including the results presented here are based on the simulations with the Morrison scheme. The Morrison scheme [*Morrison et al.*, 2009] is the updated version of its predecessor version [*Morrison et al.*, 2005] which treats 5 hydrometeor species: water vapor, cloud water, cloud ice, rain, snow, and graupel. Current study employs both the single and the double-moment versions of the Morrison schemes for the direct and indirect effects respectively. While the single moment bulk microphysics scheme predicts only the mass mixing ratio, the double moment scheme predicts both the prognostic mass mixing ratio and the number concentration of the hydrometeor species. It should be noted that the double moment scheme is required for the dust indirect effects that involves the dust effect on cloud droplet number concentration.

In the Morrison scheme, all particles are assumed to be spheres for simplicity. Size distributions of each hydrometeor species are represented by the gamma function [*Morrison et al.*, 2005]:

$$N(D) = N_0 D^{-\mu} e^{-\lambda D}$$

Here, $N(D)$ is the total number concentration per unit volume, D is the particle diameter, N_0 is the intercept parameter, μ is the shape parameter, and λ is the slope parameter. For the precipitation species (i.e., rain, snow, and graupel), as well as cloud ice, μ is considered as = 0. Thus, the size distributions for these species essentially becomes exponential functions (Marshall–Palmer distributions). For cloud droplets, μ is a calculated from the observed droplet number concentration following *Martin et al.* [1994]. In the single moment scheme N_0 is specified. In the double moment scheme N_0 is derived from the predicted number concentration, and calculated μ values. The parameter λ is derived from the predicted number concentration and mass mixing ratios, and the calculated μ value. The time tendencies of the mass mixing ratio (q) and number concentration (N) of each species consist of the terms representing advection, sedimentation, turbulent diffusion, and the source and sink terms for the microphysical processes. These microphysical processes require approximations and parameterizations by the scheme. A complete list of these microphysical processes representing the source and sink terms in the kinetic equations of q and N are given in the table 1 of *Morrison et al.* [2005].

3.3 Model Set-up and Simulation Design

The model simulations are conducted over two nested domains covering the north east Atlantic Ocean (figure 3.1). The larger domain (d01 in figure 3.1; 0 - 25°N and 20 - 50°W) is

exactly same as the domain used in the remote sensing data analyses (discussed is chapter 2). It extends from the west of the African continent to the east of the Caribbean Islands covering a significant part of the Saharan dust plumes. The smaller domain (d03 in figure 3.1; 2.5 – 11.5°N and 30 - 40°W) also have the Saharan dust, but most importantly it is within the Intertropical Convergence Zone (ITCZ) featuring strong tropical convection (not shown on the figure).

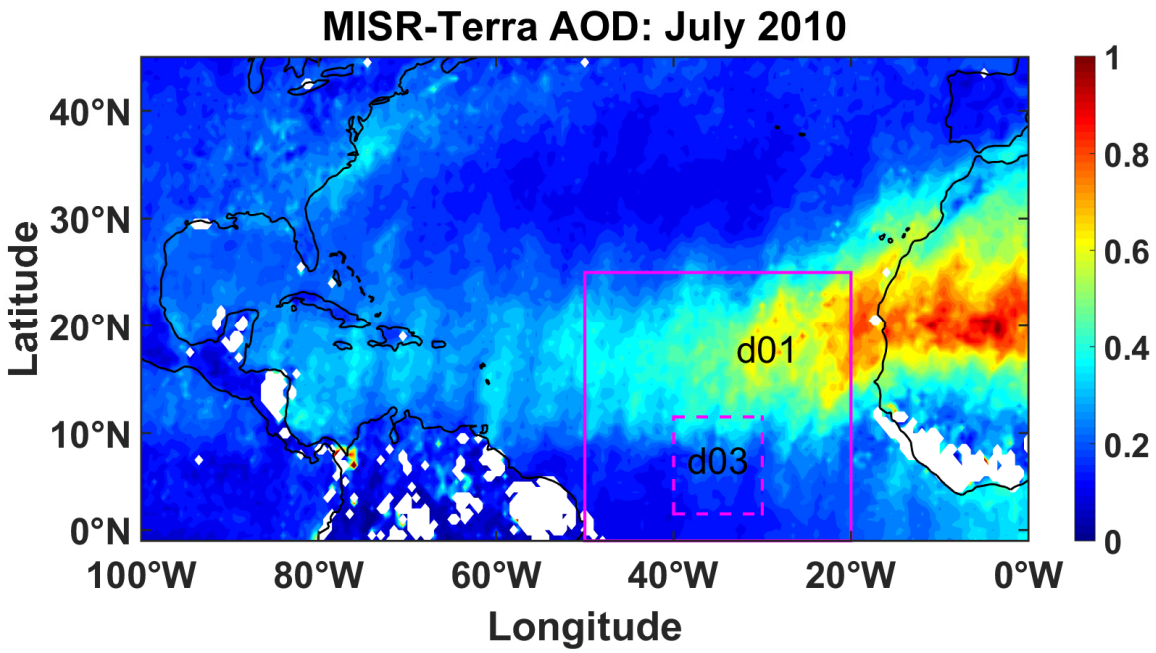

Figure 3.1 Distribution of the Saharan dust aerosols (indicated by the MISR-Terra AOD) for July 2010, and the geographical locations of the parent (d01; indicated by the solid magenta lines) and nested (d03; indicated by the dashed magenta lines) domains for the model simulations.

The model simulations are performed for two major cases: direct effect, and the indirect effects of dust. The direct effect simulations are performed only over the larger domain at 36 × 36 km resolution. On the other hand, the indirect effect simulations include both the coarser resolution (36 × 36 km) runs over the larger domain (d01), and the finer resolution runs (4 ×

4 km) over the smaller domain (d03). In both cases model are run from surface up to 1 hPa with 56 vertical eta levels.

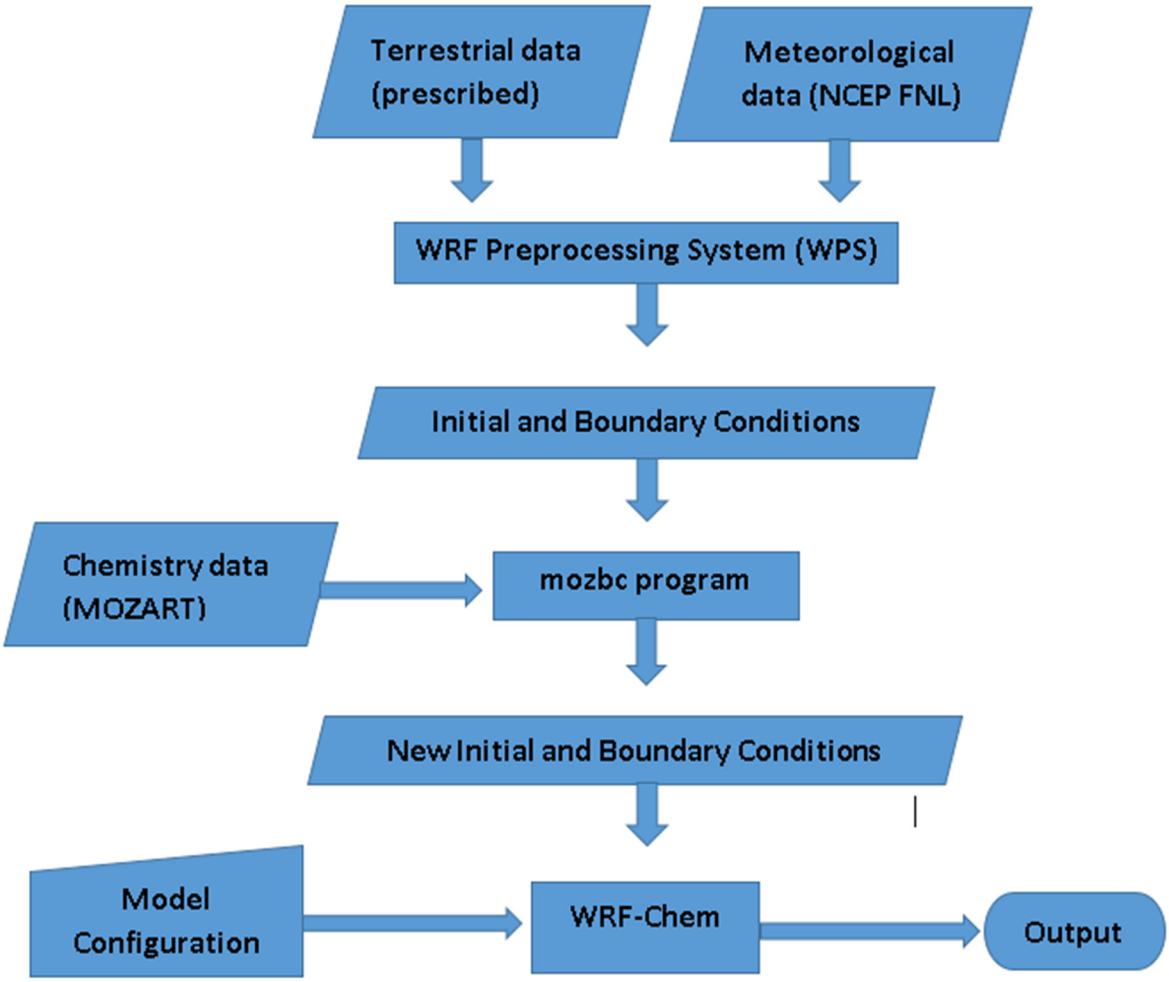

Figure 3.2 WRF-Chem version 3.6.1 modeling system flowchart for this study.

The initial and boundary conditions for the meteorological fields are provided from the National Centre for Environmental Prediction or NCEP's final analyses (NCEP FNL) data archive. As the domains are located over the Ocean, there are no massive dust emission sources within the domains. Therefore, the primary source of the dust in our domains is the Saharan dust plumes imported from the outside of the domain. In our experiments, we provide

the continuous dust flux for the larger domain (d01) through specific lateral boundary conditions supplied from the output of the version 4 of the Model for OZone and Related chemical Tracers (MOZART). The 3-D chemical transport model MOZART provides the dust emission from the Sahara desert in four dust size bins in terms of volume mixing ratios. An external program called mozbc is then used to convert the volume mixing ratios to dust mass mixing ratios, compatible with the MADE-SORGAM scheme. Figure 3.2 shows the model flowchart for this study.

Table 3.2 Details of the WRF-Chem model simulation experiments used in this study.

Experiment Name	Dust Effects	Model Resolution
D36DRY	Only radiative (direct) effect without any feedback from the cloud and moisture (microphysics and cumulus schemes are inactive)	36 km × 36 km
D36	Only radiative (direct) effect with the cloud and moisture feedback	36 km × 36 km
I36	Both radiative (direct) and cloud microphysical (indirect) effects	36 km × 36 km
I04	Both radiative (direct) and cloud microphysical (indirect) effects	4 km × 4 km

We have conducted four simulation experiments with various model configurations and resolutions for investigating the two major cases (direct and indirect effects). The model configurations and the resolutions for these experiments are presented in table 3.2. Based on

the AOD climatology discussed in chapter 2, July 2010 was found to have high positive dust loading anomaly. Therefore, all the coarser resolution (36 km × 36 km) runs are performed over 0Z July 01 to 18Z July 31, 2010. Due to the limitations of the computational resources, the finer resolution runs (4 km × 4 km) are conducted over 0Z July 06 to 18Z July 13, 2010. Model outputs for each runs are stepped every 6 hours.

Each of the four experiments listed in the table 3.2 has unique model configuration and consists of two simulations: A and B, both having the common model configuration. In the simulations 'A', the initial and the boundary condition files of the model are modified to make the dust concentration zero. Therefore, the former (run A; control run) include the effects of all aerosols excluding dust, the latter (B; test run) consider the effects from all aerosols including dust. Dust effects are then quantified from the difference between the two runs (B-A). It should be noted that the experiment D36DRY is used only for the qualitative assessment of dust impact on radiation, which has similar model configuration as the experiment D36, except that it does not simulate the cloud and moist processes. To isolate the dust effects from the radiative feedback from the cloud and moisture, in D36DRY both cloud microphysics and cumulus scheme parametrization schemes are kept inactive during the simulations. Therefore, in D36DRY the aerosol optical properties, radiative fluxes, and the heating rates are not affected by the moisture variables (e.g. water vapor, cloud, rain etc.). Rest of the three experiments (D36, I36, and I04) are used for the quantitative analysis, and therefore all the major parameterization schemes are active during the simulations of these experiments.

In addition to the simulations listed in table 3.2, several sets of sensitivity tests related to various aspects of the dust effects are also performed. Brief descriptions and results of some

of these tests are discussed in section 5.1. Rest of the sensitivity test results are not discussed in this dissertation, but only their findings are referred in the text wherever relevant.

3.4 Model Validation

In this section, we discuss the evaluation of the model performance by comparing the model simulations against the satellite measurements and analyses data from various platforms. The evaluation is performed by using the data from the AIRS (Atmospheric InfraRed Sounder) on Aqua satellite, MODIS (MOderate resolution Imaging Spectroradiometer) on both Terra and Aqua satellites, the TRMM (Tropical Rainfall Measuring Mission) satellite, GPCP (Global Precipitation Climatology Project), CALIPSO (Cloud-Aerosol Lidar and Infrared Pathfinder Satellite Observations), and the NCEP (National Centre for Environmental Prediction) final analyses. The validated model output variables are: tropospheric temperature (T), water vapor mass mixing ratio (mmr; q), cloud Liquid Water Path (LWP), accumulated surface precipitation rate (P), and the dust extinction (β). Here, we only discuss the validation of these variables from the outputs of the experiments: D36 and I36.

Figure 3.3a shows the spatially and temporally averaged (0-25°N, 20-50°W and 0Z July 01 to 18Z July 31, 2010) vertical profiles of the tropospheric temperature (T; K) from D36B, I36B, NCEP, and AIRS and the figure 3.3b shows the respective temperature biases (ΔT; K) against the mean AIRS temperature profile. We see that the model simulated temperature profiles are very similar in the two experiments (D36B and I36B) and generally agree well with both the NCEP analysis and AIRS observation data (figure 3.3a). In the lower troposphere (below ~ 7 km) the model show cold bias that reach up to ~ -0.6 K at ~ 1.5 km compared to the AIRS

(figure 3.3b). However, both model runs show better agreement with the NCEP profile than the AIRS profile, especially in the lower troposphere.

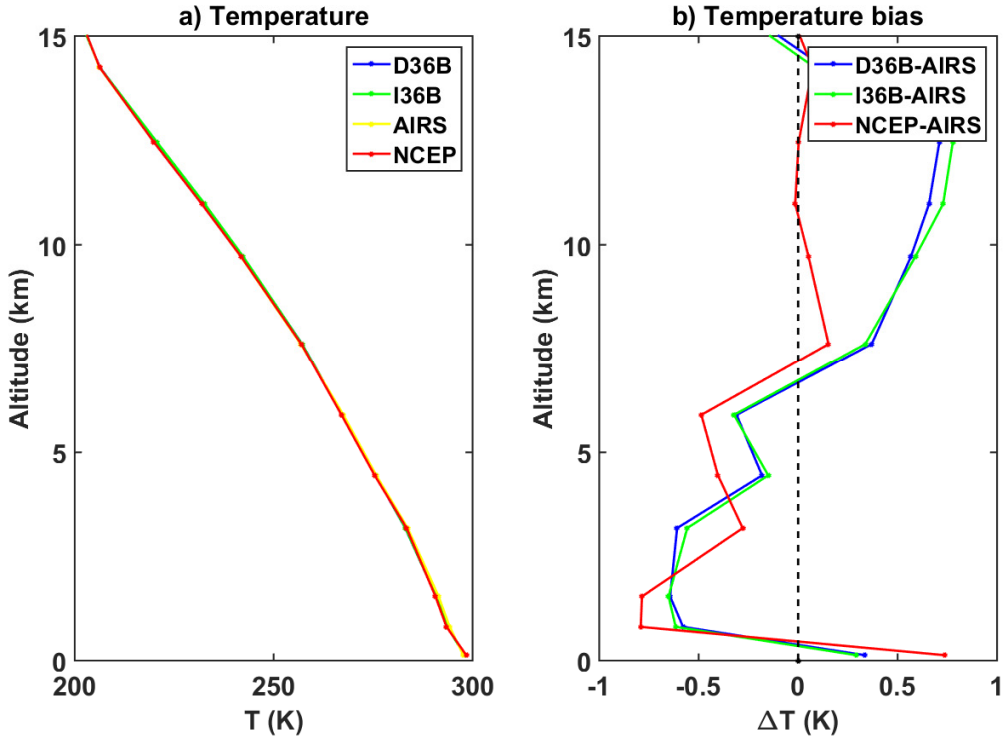

Figure 3.3 Time and domain averaged (0Z July 01 to 18Z July 31, 2010, and 0-25°N, 20-50°W) vertical profiles of the a) temperature (*T*) from the WRF-Chem simulations including dust (D36B and I36B), NCEP analyses and the AIRS datasets, and the b) temperature biases (*ΔT*), calculated with respect to the AIRS dataset.

Model simulations of the tropospheric water vapor (*q;* g/kg) are compared with the AIRS measurements, as shown in figures 3.4a-b. The two experiments (D36B and I36B) yield very similar moisture profiles (as they overlap; figure 3.4a). However, compared to the AIRS profile the model clearly overestimates the moisture throughout the troposphere (figure 3.4b). The maximum model wet bias is ~ 1.6 g/kg (14%) at ~ 1.5 km. This is reasonable as the results are based on one month model forecast. Nevertheless, we find that the simulated temperature and water vapor profiles are consistent between the two experiments (D36 and I36) indicating

that these model outputs are not sensitive to the choice of the model configurations considered for the direct and indirect effects.

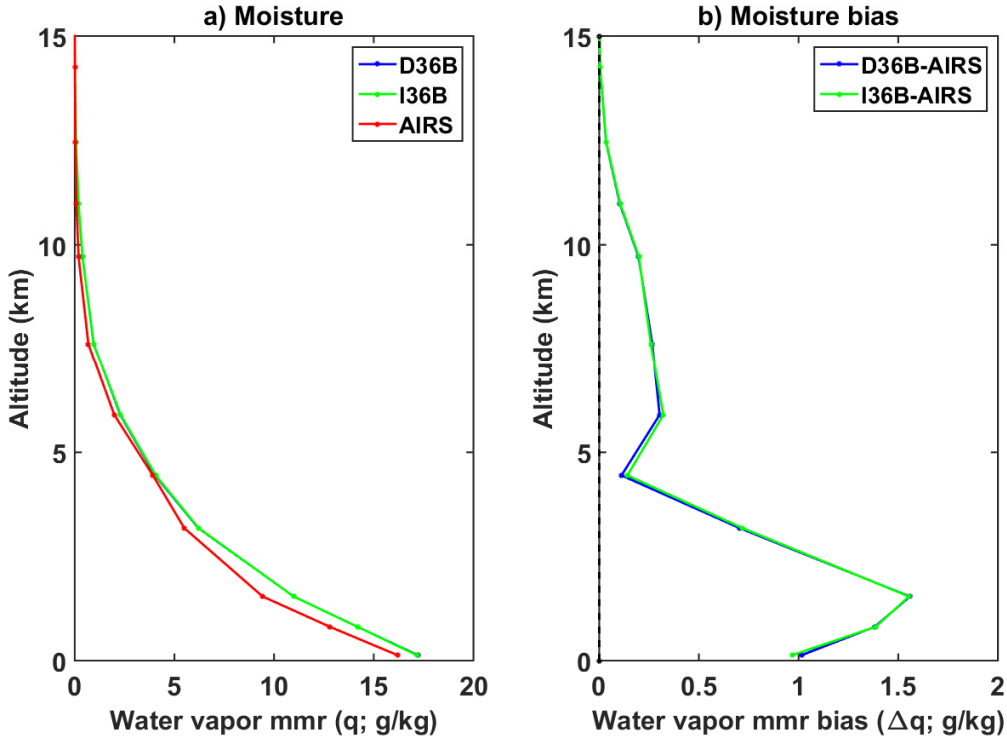

Figure 3.4 Time and domain averaged (0Z July 01 to 18Z July 31, 2010, and 0-25°N, 20-50°W) vertical profiles of the a) water vapor mass mixing ratio (q) from the WRF-Chem simulations including dust (D36B and I36B), and the AIRS datasets, and the b) water vapor mass mixing ratio biases (Δq), calculated with respect to the AIRS dataset.

Time evolutions of the model simulated LWP is compared with the LWP products from the MODIS Terra and Aqua observations. As the model does not directly calculate the Cloud Liquid Water Path (LWP; g/m^2), we integrate the model output of the cloud liquid water mass in the vertical column over each grid cell to obtain the LWP:

$$LWP = \int q\rho_{air}dz \cong \sum_{k=1}^{k=56} q_k(P_{k+\frac{1}{2}} - P_{k-\frac{1}{2}})/g$$

where, q is the atmospheric water vapor mass mixing ratio, ρ_{air} is the density of air, $P_{k+\frac{1}{2}}$ and $P_{k-\frac{1}{2}}$ are the air pressure at the two consecutive model half-levels corresponding to the k-th full level, and g is the gravitational acceleration.

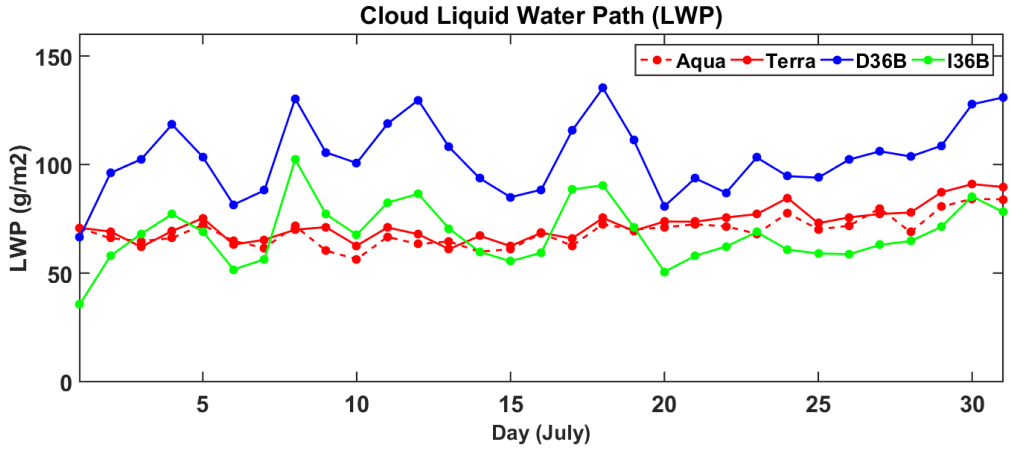

Figure 3.5 Domain averaged (0-25°N, 20-50°W) Cloud Liquid Water Path (*LWP*) time series from the WRF-Chem simulations including dust (D36B and I36B), and the measurements from the MODIS instrument on Terra and Aqua satellites. Individual data points represent daily mean values through July 1-31, 2010.

The LWP comparison (figure 3.5) indicates some discrepancies between the Terra and Aqua measurements. Despite these disagreements between the two MODIS datasets, it is very clear that the aerosol direct effect-only simulation (D36) produce excessive cloud amount compared to the observations (Terra and Aqua). The experiment I36, which includes both the direct and indirect effects show both underestimation and overestimation of the cloud throughout the simulation period. However, compared to the D36, the experiment I36 shows much better agreement with the two MODIS LWP time series. While the monthly mean LWP in D36 is overestimated by 43% and 50% with respect to the Terra and Aqua respectively, the mean LWP in I36 is underestimated by only 6% and 2% with respect to these measurements. As mentioned in section 3.2.4, prior to using the Morrison scheme, the Lin scheme was used to

simulate the grid scale cloud and moist processes. Results (not shown here) with the Lin scheme showed similar features where the cloud is overestimated in the direct effect case. We therefore conclude that both direct and the indirect aerosol effects need to be considered together to reproduce the reasonable cloud amount.

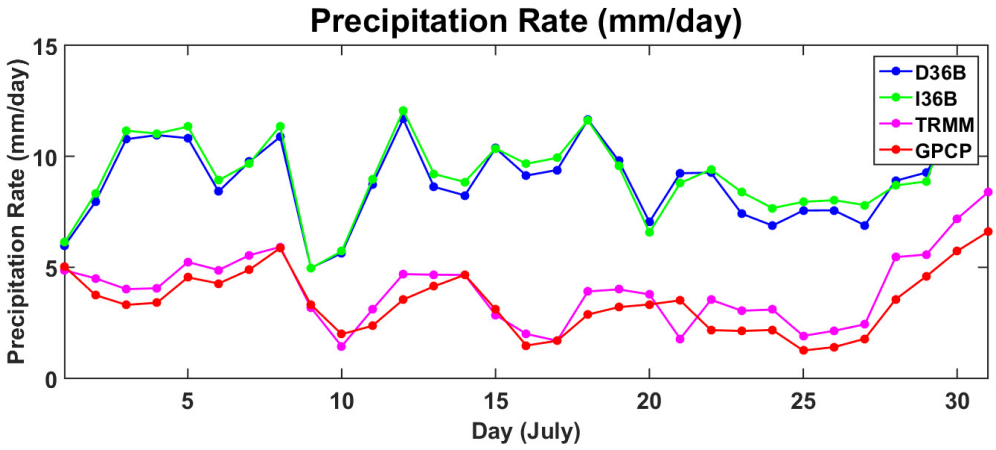

Figure 3.6 Domain averaged (0-25°N, 20-50°W) Precipitation rate (*P*) time series from the WRF-Chem simulations including dust (D36B and I36B), and measurements from the TRMM, and GPCP datasets. Individual data points represent daily mean values through July 1-31, 2010.

Model outputs of the accumulated grid scale and sub-grid scale precipitation in every six hours are combined to generate the precipitation rate (mm/day) time series through July 2010. Precipitation measurements from TRMM, and GPCP are used to validate the model results. Comparisons (figure 3.6) show that both experiments (D36B and I36B) overestimate the precipitation rate. This overestimation is possibly linked to the shallow convection used in the cumulus parameterization scheme. Sensitivity tests with disabling the shallow convection (figures not shown here) give better agreement of the total model precipitation with the observed precipitation. However, the shallow convection is necessary for vertical distribution of heat and moisture, especially for the tropical region. *Smith* [2013] suggested that, without

the shallow convection, moisture transport from the boundary layer to the free troposphere becomes weaker, leading to drying above 900 hPa and moistening below. *Cai et al.*, [2016] studied the sensitivity of the shallow convection parameterization over the tropics using the CAM model. They reported that the spatial pattern of precipitation amount, and the precipitation frequency and intensity are better reproduced when the shallow convection is enabled. Therefore, despite the overestimation of the precipitation we retain with the shallow convection parameterization in our simulations.

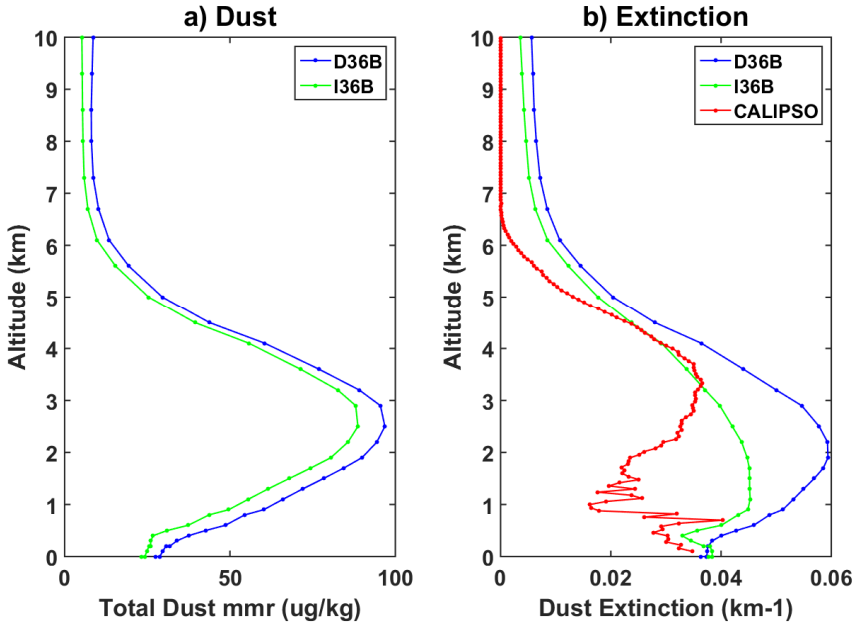

Figure 3.7 Time and domain averaged (0Z July 01 to 18Z July 31, 2010, and 0-25°N, 20-50°W) vertical profiles of the a) total dust mass mixing ratio (*D*), and the b) dust extinction (β) coefficient at 550 nm, and 532 nm from the WRF-Chem simulations including dust (D36B and I36B), and the CALIPSO dataset respectively.

Satellite measurements of the vertical features of dust is very scarce. We use the radiation extinction profiles from the CALIPSO retrieval at 532 nm to validate the model simulation of the dust. Spatially and temporally averaged vertical profiles of the total (three modes together) dust mass mixing ratio from the model outputs and the dust induced radiation extinction (B-

A) at 550 nm are shown in figures 3.7a-b respectively. We see that the dust loading is lower in I36B (figure 3.7a). This can be attributed to the extra removal processes in I36 (direct + indirect effects) where the aerosol wet scavenging is considered. We also find that beyond 6 km, dust mass mixing ratio decreases to nearly ~10% of the peak value (85 μg/kg in D36B and 95 μg/kg in I36B at 2.5 km). Extinction profiles (figure 3.7b) show that the model overestimates the dust extinction with respect to the CALIPSO, especially in the lower levels. However, the CALIPSO observation itself show random fluctuations in these levels indicating the uncertainty of the measurement. In addition, the discrepancy may also be related to the very coarse resolutions (5° × 2°) of the CALIPSO dataset.

Chapter 4: Radiative Effects of the Saharan Dust

4.1 Absorption and Scattering Properties of the Saharan Dust

In this chapter, we investigate the radiative forcing of the Saharan dust over the tropical East Atlantic Ocean through July 2010. We also discuss the consequence of the changes in radiative fluxes on the atmospheric heating rates and the surface heat fluxes. Results presented here are primarily based on our analyses of the model simulations: D36A and D36B which include only the aerosol radiative (direct) effect, including the cloud feedback. The magnitude of the dust radiative forcing depends on the size dependent optical properties of the dust particles, its horizontal and vertical distribution and the feedback from the cloud [e.g., *Nousiainen*, 2009; *Mahowald et al.*, 2014]. Therefore, we first analyze the horizontal and vertical distributions of the dust over the domain from the model output and also their absorption and scattering properties in relation to the other aerosols of the domain.

As mentioned in chapter 3, the MADE-SORGAM aerosol scheme coupled with the WRF-Chem for the simulations treats dust in three log-normal size modes: atiken mode (particle diameter < 0.1 μm), accumulation mode (particle diameter between 1 μm to 0.1 μm), and the coarse mode (particle diameter >1 μm). Monthly mean (0Z July 1- 18Z July 31, 2010) geographical (0-25°N, 20-50°W) distributions of the vertically integrated column mass densities (g/m2) of the atiken mode (D_{c1}), accumulation mode (D_{c2}), coarse mode (D_{c3}) dust and their sum (D_c) from the model run D36B are shown in figures 4.1a-d respectively. As expected, the dust burden is concentrated mainly in the north eastern part of the domain where the SAL enters the domain, and then gradually decrease westward. Although, the coarse mode

dust particles are the heaviest of the three modes, accumulation mode dust contribute the most in the total dust loading of the domain. The mean (spatial and temporal) column mass densities of the atiken mode and coarse mode dust are 0.03 g/m2 and 0.07 g/m2 respectively, whereas the accumulation mode dust column mass density is 0.26 g/m2, contributing nearly three quarter of the combined dust mass loading of the domain. This has significant impact on the radiative forcing as the radiative parameters of the mineral aerosols are strongly dependent on the particle size [*Tegen et al.*, 1997; *Mahowald et al.*, 2014].

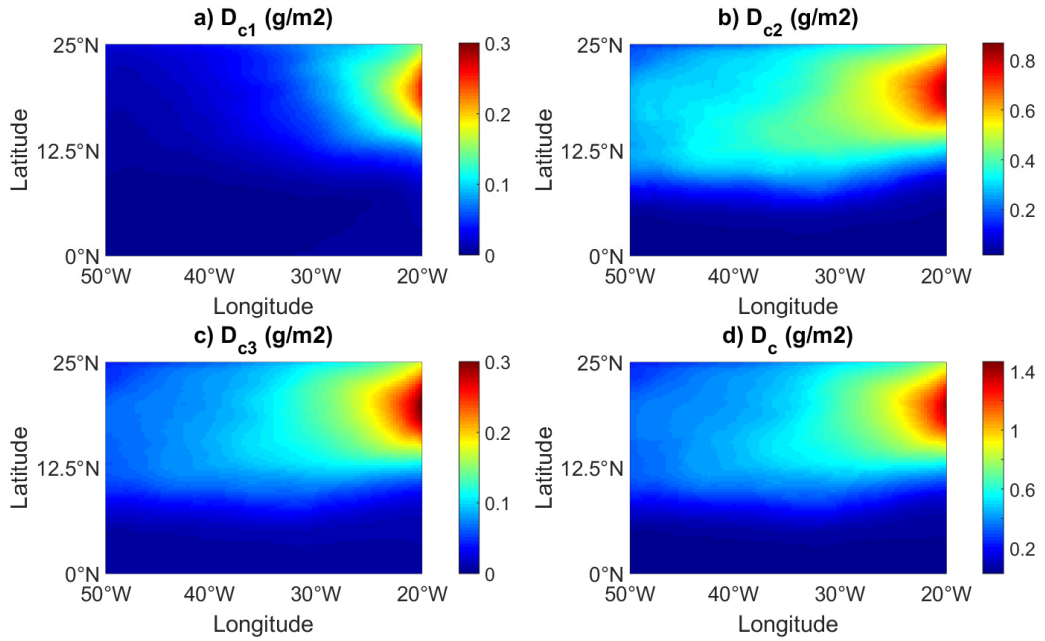

Figure 4.1 Time averaged (0Z July 01 to 18Z July 31, 2010) horizontal distributions of the column mass densities (g/m2) of the a) atiken mode (D_{c1}), b) accumulation mode (D_{c2}), c) coarse mode (D_{c3}), and the d) total (D_c) dust aerosols. All the data are taken from the outputs of the simulation D36B.

Domain averaged monthly mean (0-25°N, 20-50°W and 0Z July 01 to 18Z July 31, 2010) vertical profiles of the mass mixing ratios of the three dust size modes, total aerosol absorption and scattering coefficients (β_a and β_s respectively; km^{-1}) at four different shortwave wavelengths (300 nm, 400 nm, 600 nm, and 1000 nm) are shown in figures 4.2a-c

respectively. Similar to the horizontal distributions (figure 4.1a-d), it is evident that, the accumulation mode dust aerosols are the dominant amongst the three size modes (figure 4.2a). The peak dust loading (~12 ug/kg, ~60 ug/kg, and ~20 ug/kg for the three modes respectively) occur at ~ 2.5 km regardless of their sizes.

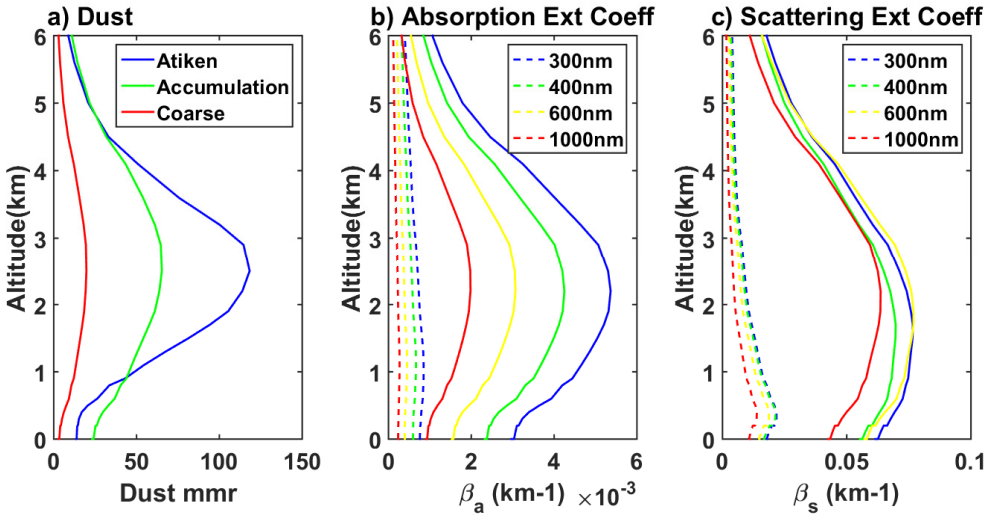

Figure 4.2 Vertical profiles of the time and domain averaged (0Z July 01 to 18Z July 31, 2010; 0-25°N, 20-50°W) a) dust mass mixing ratio (D; µg/kg) for the atiken mode ($\times 10^{-1}$), accumulation mode, and the coarse mode dust aerosols from D36B, b) aerosol absorption coefficients (β_a; km-1) from D36A (dashed lines) and D36B (solid lines), and c) aerosol scattering coefficients (β_s; km-1) from D36A (dashed lines) and D36B (solid lines) at different shortwave wavelengths.

Compared to the other aerosols in the domain, the net contribution of dust to the total absorption and scattering is significantly higher, as seen from the respective magnitudes of absorption and scattering coefficients in the two model runs: D36A and D36B (dashed versus solid lines in both figures 4.2b and 4.2c). This clearly suggests that dust is the primary aerosol species contributing to the total radiation extinction by aerosols in the domain which also agrees with the finding from the observation data (discussed in chapter 2). The maximum absorption of radiation at any of the four wavelengths occur in the layers between 2-3 km that consists the peak of the dust loading layer (figures 4.2a-b). The absorption efficiency of the

dust (solid lines in figure 4.2b) show significant variations with the wavelengths, in contrast to the scattering efficiency (solid lines in figure 4.2c) which has less spectral dependence. The absorption is strongest in the lower end of the spectral region (300 nm) and become weaker with increasing wavelengths. This agrees with the finding from *Petzold et al.* [2009] who studied the optical properties of the Saharan dust under the SAMUM (Saharan Mineral Dust Experiment) project. The authors reported that the imaginary part of the refractive index of the Saharan dust is sensitive to the wavelength due to diverse chemical composition of the particles. However, in the current experiments (D36A and D36B), both the real and the imaginary parts of the refractive index (give scattering and absorption respectively) are held constant, regardless of the wavelength. Therefore, in our case the sensitivity of the absorption and scattering to different wavelengths (figures 4.2b-c) can be attributed to the size distribution of dust and/or the moisture content of the dust. It should be noted that although the refractive indices of dust are fixed, the refractive indices of the aerosol water in D36A and D36B are wavelength dependent which influence the weighted refractive indices passed to the Mie calculation.

For the mineral dust aerosols, scattering dominates the absorption in the shortwave wavelength ranges [*Otto et al.*, 2007]. Here we analyze the relative contributions of the dust scattering and absorption to the total Aerosol Optical Depth (AOD). Horizontal distributions of the dust absorption and scattering AODs, and their sum (absorption + scattering) at four different shortwave wavelength bands (SW) are shown in figures 4.3a-l. Dust AODs are calculated from the difference between the AODs from the dust-laden (D36B) and the dust-free (D36A) runs.

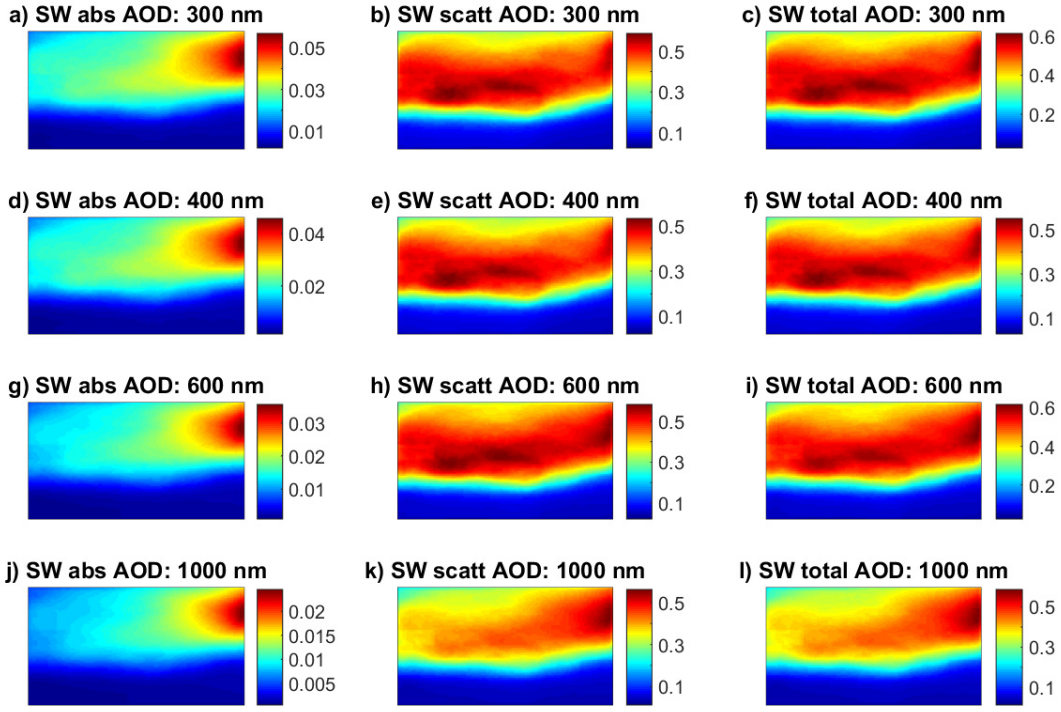

Figure 4.3 Time averaged (0Z July 01 to 18Z July 31, 2010) horizontal distributions of the absorption (abs), scattering (scatt), and total dust AOD at different shortwave (SW) wavelengths. Abscissa and ordinate represent the longitude and latitude respectively. Dust AODs are calculated from the difference between the AODs from the dust-laden (D36B) and the dust-free (D36A) runs.

As expected, the scattering is dominant than the absorption. We see that the absorption maxima (figures 4.3a, 4.3d, 4.3g, and 4.3j) are collocated with the dust loading maxima (figures 4.1a-d). However, strong scattering occur in most parts of the domain which are not consistent with the dust loading pattern. Consequently, the total AOD (absorption + scattering) maxima (~ 0.7) are located around the middle of the domain (~ 30 ° W, 12 °N and ~ 40 ° W, 12 °N) instead of the region where dust loading peaks occur (north eastern part of the domain). To identify the possible causes of the shifting of the AOD peaks, dust AODs from the experiment D36DRY are analyzed. As mentioned in chapter 3, D36DRY does not simulate any moisture variables (e.g. water vapor, cloud, rain etc.) and therefore, the dust interactions

with the radiation is not affected by any of the moisture fields. The results (figure 4.4) show that without the presence of any moisture, both the absorption and scattering (and therefore the total) maxima are consistent with the dust loading throughout the domain. Therefore, the scattering throughout the domain found in D36 (figure 4.3) can be attributed to the modulation of dust scattering property due to the atmospheric moisture content.

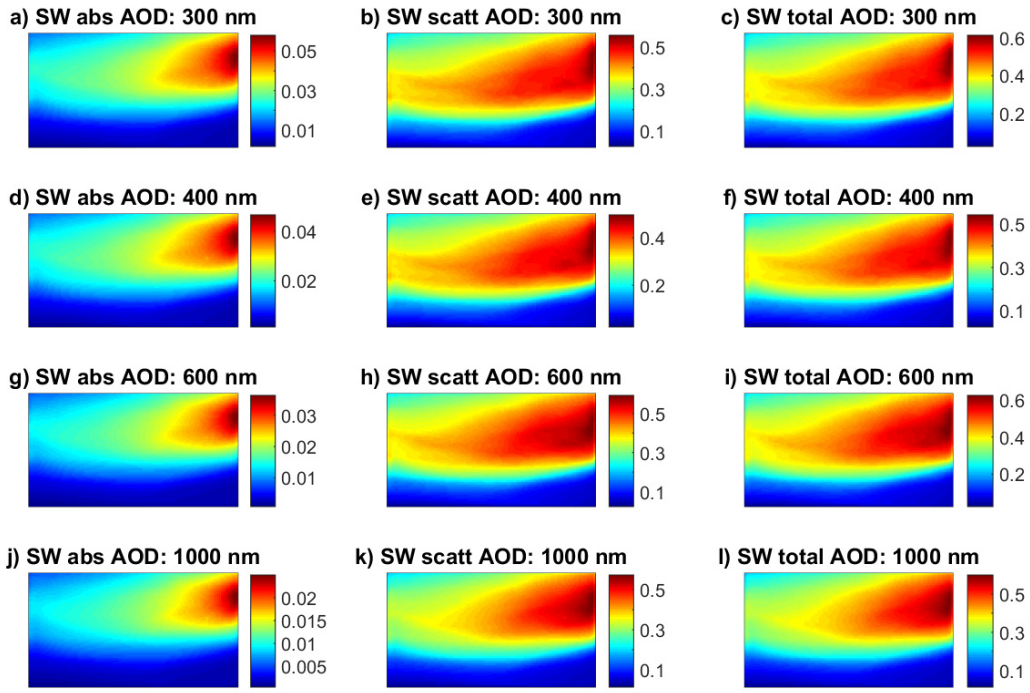

Figure 4.4 Same as figure 4.3, but the data correspond to the experiment D36DRY.

Unlike the SW, dust absorption prevail over scattering in the Longwave (LW) bands [*Mahowald et al.*, 2014]. Dust AOD (AOD difference between D36B and D36A) distributions at 16 longwave bands (LW) are shown in figures 4.5a-p. It should be noted that, due to the relatively smaller contributions of the scattering, like many climate models, aerosol scattering effects in the longwave bands are not considered in the RRTMG radiation module of the WRF-

Chem. Therefore, the AODs shown in figures 4.5a-p are entirely due to the longwave absorption AOD.

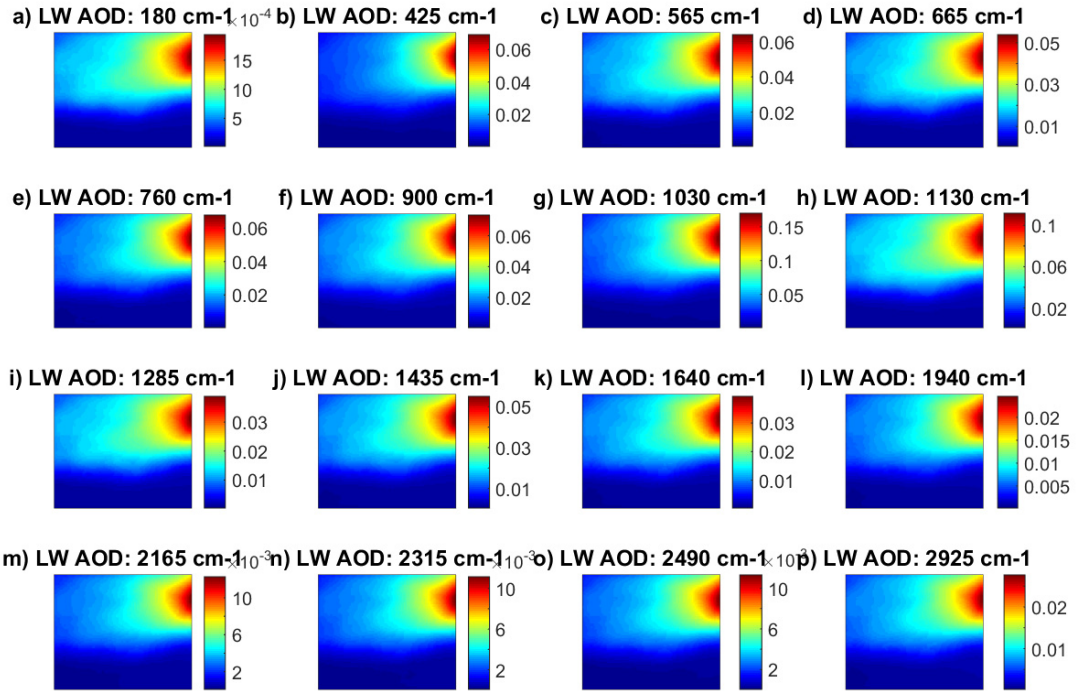

Figure 4.5 Time averaged (0Z July 01 to 18Z July 31, 2010) horizontal distributions of the total dust AOD at different longwave wavelengths. Abscissa and ordinate represent the longitude and latitude respectively. Dust AODs are calculated from the difference between the AODs from the dust-laden (D36B) and the dust-free (D36A) runs.

Similar to the shortwave absorption AODs (figures 4.3a, 4.3d, 4.3g, and 4.3j), all the longwave AOD distribution (figures 4.5a-p) follow the dust distribution patterns (figures 4.1a-d). However, the longwave AODs are well below 0.2 which are relatively smaller compared to the shortwave AODs (absorption + scattering) discussed earlier. The only significant longwave AOD comparable to the shortwave AODs is the AOD at 1030 cm^{-1} (covering the band 980-1080 cm^{-1}) that reach up to 0.17 at its peak (figure 4.5g). Stronger absorption at this particular longwave wavelength band is attributed to the high imaginary part of the refractive index refractive index (0.65) which is the result of the stronger absorption near 1050 cm^{-1} by

quartz contained dust [*Highwood et al.*, 2003]. This absorption peak falls within the infrared atmospheric window (8-12 um). As the dust particles absorb and reemit the longwave radiations back towards the surface (analogous to the greenhouse gases), dust absorption at this wavelength plays a crucial role in regulating the longwave radiation budget [*Osborne et al.*, 2011].

4.2 Clear-Sky Radiative Forcing of the Saharan Dust

In this section, we discuss the effects of the dust absorption and scattering on the cloud-free radiative energy budgets of the atmosphere (ATM), on the surface (SUR), and at the top of the atmosphere (TOA) over our domain. Schematic diagrams of the quantitative comparison of all the domain averaged radiative flux components (W/m^2) and the respective dust forcing in clear sky condition are shown in figure 4.6. Interactions of dust aerosols with the SW and LW radiations primarily affects the upwelling SW radiation at the TOA (SWUPT), downwelling SW radiation at the SUR (SWDNB), and the downwelling LW radiation at the SUR (LWDNB). Perturbations of these fluxes lead to the net radiative forcing at ATM, SUR, and TOA. In the following, we discuss the horizontal distributions of these radiative forcing and attempt to correlate them with the absorption and scattering AOD from dust. Radiative forcings are calculated from the difference of the net (downward-upward) fluxes between the dust-laden (D36B) and the dust-free (D36A) runs. For instance, the radiative forcing at the top of the atmosphere (RF_{TOA}) is calculated as follows:

$$RF_{TOA} = [SWDNT(B) - SWUPT(B) + LWDNT(B) - LWUPT(B)] - [SWDNT(A) - SWUPT(A) + LWDNT(A) - LWUPT(A)]$$

where, SWDNT, SWUPT, LWDNT, and LWUPT are the downward shortwave radiative flux, upward shortwave radiative flux, downward longwave radiative flux, and upward longwave radiative flux at the TOA respectively. Similar convention is used to calculate the radiative forcings inside the atmosphere (RF_{ATM}), and at the surface (RF_{SUR}).

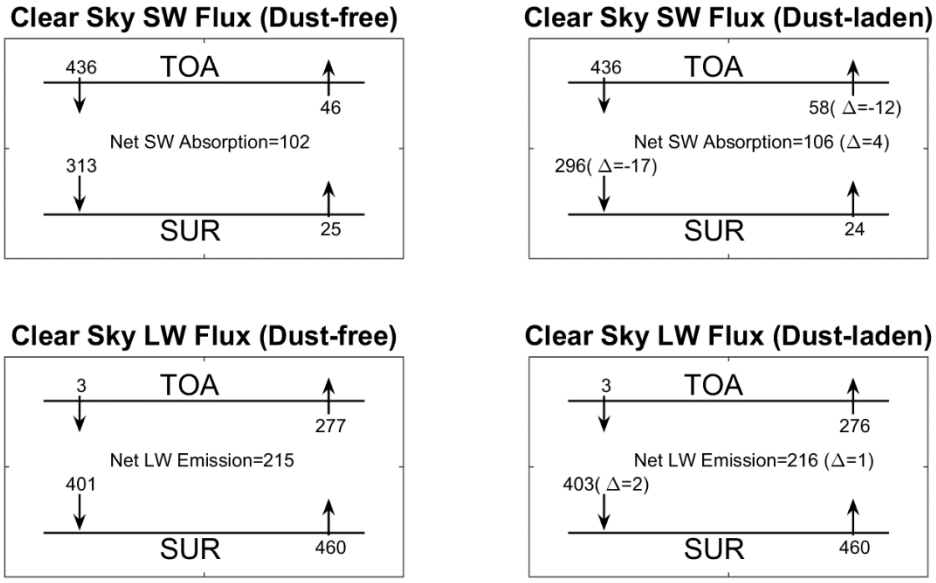

Figure 4.6 Schematic diagram of the time and domain averaged (0Z July 01 to 18Z July 31, 2010; 0-25°N, 20-50°W) radiative flux components (W/m^2) for the clear sky condition. All the data are taken from the outputs of the experiment D36.

Dust induced clear-sky atmospheric shortwave, longwave, and net radiative forcing (RF_{ATM}) over our study domain (averaged through 0Z July 1- 18Z July 31, 2010) are shown in figures 4.7a-c respectively. Both the shortwave and longwave forcing patterns (figures 4.7a-b respectively) follow the respective absorption AOD fields discussed earlier (figures 4.3 and 4.5 respectively). Therefore, we can attribute these forcing to the changes in atmospheric absorption and emission of radiation (as opposed to the scattering) due to the presence of dust. We find that the net effect of shortwave throughout the domain is warming only. In contrary,

the longwave accounts for both warming and cooling depending on the relative magnitudes of the absorption and emission at a particular grid cell. Shortwave positive radiative forcing (enhanced absorption) in the domain reach up to ~ +12 W/m^2 at the north eastern part of the domain where the dust loading is maximum (figure 4.7a). Longwave negative radiative forcing (enhanced emission) also reaches maximum (~ -8 W/m^2) at the dust maxima and partially compensate the positive shortwave forcing. In addition to the emission, absorption of longwave also give slight warming effect (< +1 W/m^2) spread throughout the domain (figure 4.7b). The net (shortwave + longwave) dust forcing over the domain is mostly positive and give net warming of the atmosphere in most areas (figure 4.7c). Consequently, the domain averaged net radiative forcing due to dust during July is ~ +3 W/m^2. Previous studies on dust impact over diverse regions [e.g., *Zhu et al.*, 2007; *Zhao et al.*, 2013; *Vinoj et al.*, 2014] also reported net positive forcing (warming effect) of dust in the atmosphere. For example, *Zhu et al.* [2007], who investigated the dust radiative forcing over the east Atlantic Ocean among other regions have found RF_{ATM} ~ +8.16 W/m^2 during summer season (June-August), which is stronger than our result.

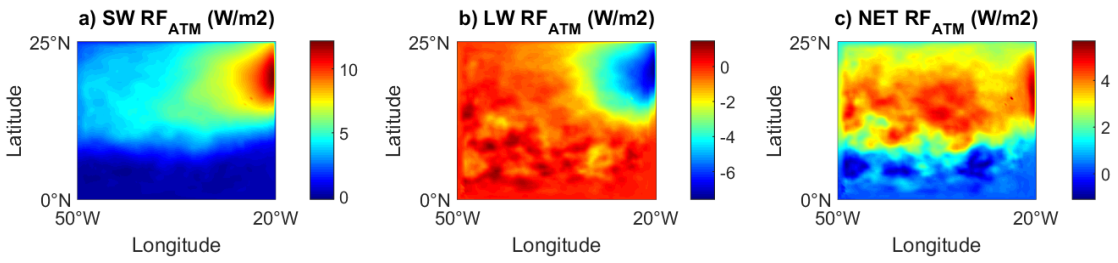

Figure 4.7 Time and domain averaged (0Z July 01 to 18Z July 31, 2010; 0-25°N, 20-50°W) horizontal distributions of the a) shortwave, b) longwave, and c) net (shortwave + longwave) radiative forcing (W/m^2) of the atmosphere (ATM) for the clear sky condition. All the data are taken from the outputs of the experiment D36.

The dust radiative forcing at the surface (RF_{SUR}) is controlled by the enhanced absorption and scattering of the shortwave, and the trapping of longwave inside the atmospheric layers. Past studies have found dust induced reduction of the radiative fluxes at the surface which is referred as the surface dimming [*Zhu et al.*, 2007; *Mallet et al.*, 2009]. Figures 4.8a-c show the clear sky shortwave, longwave and net radiative forcing at the surface respectively. Shortwave forcing is negative everywhere in the domain with the minima of ~ -30 W/m^2 at the dust maxima (figure 4.8a). This is because of the strong attenuation of shortwave radiation by the dust particles in the atmosphere. The longwave radiative forcing at SUR is mostly positive showing an increase of the downward longwave flux (figure 4.8b). Due to the strong downward longwave emission from the dust layers, the longwave forcing also peaks at the maximum dust region where it reaches to ~ + 9 W/m^2. However, this positive longwave forcing only partially compensates the stronger positive forcing by shortwave, giving a net negative dust radiative forcing at the surface (figure 4.8c). The domain averaged value of the net radiative forcing at the surface is -14 W/m^2. This is very close to the estimation of *Zhu et al.* [2007] who found a reduction of 14.2 W/m^2 at the surface over the east Atlantic Ocean through June to August.

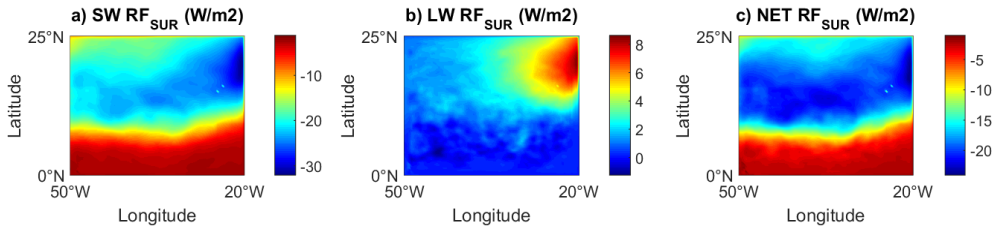

Figure 4.8 Same as figure 4.7, but for the surface (SUR).

Regional net radiative forcing of dust at the top of the atmosphere can be both positive and negative [*Liao and Seinfeld*, 1998]. This is because the RF_{TOA} not only depends on the optical

properties of dust but also depends on the atmospheric column and the underlying surface [e.g., *Shell and Somerville*, 2007]. Over dark surfaces (e.g., Ocean) the dust radiative forcing is negative as the dust enhance the Earth's reflectance. Radiative forcing at the top of the atmosphere (RF_{TOA}) in both the shortwave and longwave spectrum, and their sum are shown in figures 4.9a-c respectively.

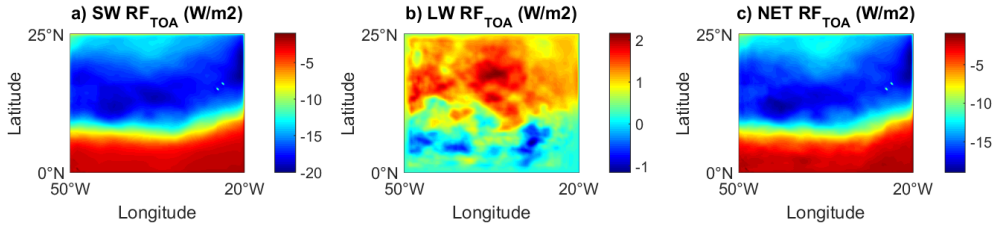

Figure 4.9 Same as figure 4.7, but for the top of the atmosphere (TOA).

Unlike the RF_{ATM} and RF_{SUR}, the RF_{TOA} (for both the shortwave and longwave) are inconsistent (figures 4.9a-b) with the dust absorption AOD patterns (figures 4.3 and 4.5) and therefore indicates that the forcing at the TOA is mainly due to shortwave scattering by dust layers, instead of the absorption. Shortwave forcing minima at the middle of the domain (figure 4.9a) coincide with the scattering AOD maxima corresponding to the shorter shortwave bands (300-600 nm; figure 4.3). For the longwave bands, both positive and negative forcing are present which are very small in magnitude (vary from -1 W/m^2 to +2 W/m^2; figure 4.9b), and therefore have very negligible contribution to the net radiative forcing (figure 4.9c). The net radiative forcing at the top of the atmosphere over the domain is -11 W/m^2. Therefore, the enhanced shortwave reflection by the dust layers is primarily responsible for the negative radiative forcing at the top of the atmosphere. The mean shortwave forcing from our experiment (-12 W/m^2) is relatively smaller compared to the satellite based estimation by *Li et al.* [2004]. The authors studied the Saharan dust forcing near the African coast and estimated

the shortwave radiative forcing at TOA is -65 W/m^2 per unit AOD during the high dust season (June-August). However, our result is much closer to the result from *Zhu et al.* [2007] who found the shortwave radiative forcing of -14.37 W/m^2 at the TOA.

4.3 Dust Effects on Atmospheric Heating Rates and Temperature

In the previous section, radiative effects of dust on surface, atmosphere and at the top of the atmosphere are discussed. Here we analyze the consequences of the perturbation of these radiative energy balances in the tropospheric heating rates at different atmospheric layers. First, we examine the qualitative distributions of the instantaneous dust mass mixing ratio and the change in atmospheric radiative heating rates (temperature tendency) due to the dust.

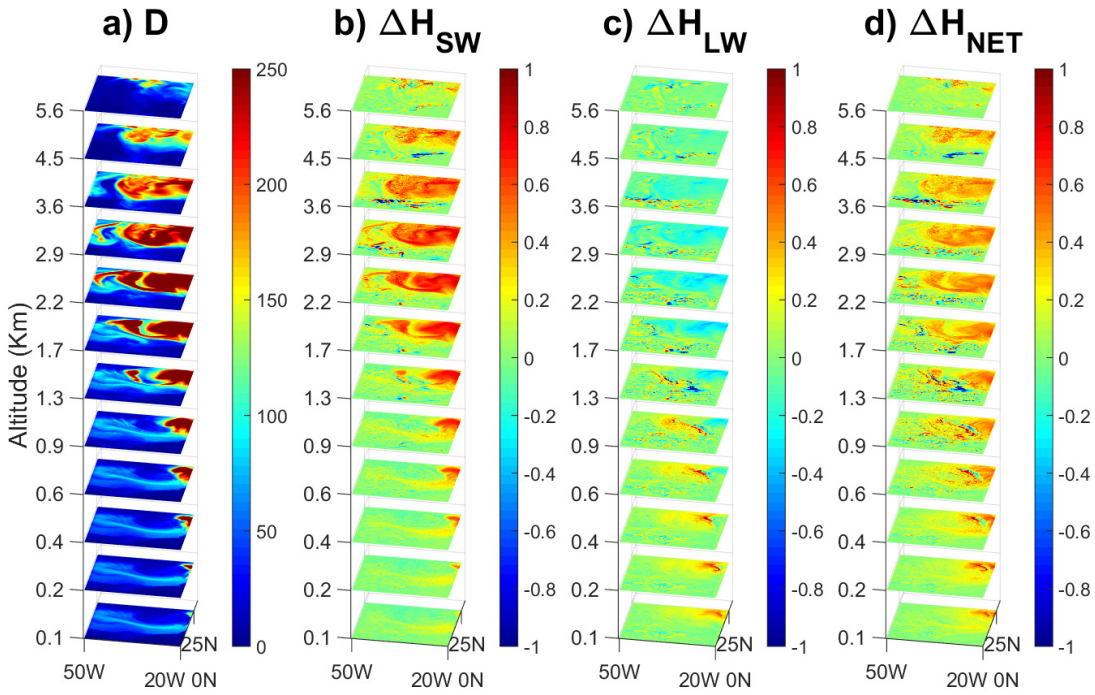

Figure 4.10 Instantaneous (12 Z, July 12, 2010) distributions of the a) total dust mass mixing ratio (*D*; µg/kg), dust induced changes (B-A) of the atmospheric heating rates (K/day) due to the b) shortwave (ΔH_{SW}), c) longwave (ΔH_{LW}), and d) net radiation (ΔH_{NET}). All the data are taken from the outputs of the experiment D36DRY.

Three dimensional distributions of the total dust mass mixing ratio (D; ug/kg) and the dust induced modulations of the atmospheric heating rates (B–A) through shortwave (ΔH_{SW} ; K/day), longwave (ΔH_{LW} ; K/day), and their sum (ΔH_{NET}; K/day) from the experiment D36DRY are shown in figures 4.10a-d respectively. In this experiment, the shortwave and longwave radiations are the only contributors to the net heating of the atmosphere. We find that the shortwave heating and longwave cooling rate changes are consistent with the dust distribution. Moreover, analogous to the greenhouse gases in the atmosphere, the dust layers can also absorb the longwave radiation emitted from the surface and then reemit back towards the surface [*Highwood et al.*, 2003; *Zhu et al.*, 2007]. This gives lower level warming through longwave absorption (figure 4.10c). Due to this longwave trapping in the lower levels, we find net warming in the lower levels (figure 4.10d).

We now examine the quantitative changes of the heating rates compared to the dust-free heating rates during July 2010. Here we use the heating rates from the experiment D36. It should be noted that the heating rates in D36 are not only the result of the clear sky atmospheric radiative forcing but also the feedback from the changes in cloud and atmospheric dynamics. As there is a significant difference of dust loadings from east to west (figures 4.1a-d), similar to approach used in chapter 2 we analyze the heating rates by dividing the entire domain into three longitude bands: 20-30°W (High dust), 30-40°W (Moderate dust), and 40-50°W (Low dust). The latitude ranges (0 - 25°N) are the same for the three regions. Spatially and temporally averaged vertical profiles of the shortwave and longwave atmospheric heating rates and their sum (H_{SW}, H_{LW}, and H_{NET} respectively) for the three regions are shown in figures 4.11a-i respectively.

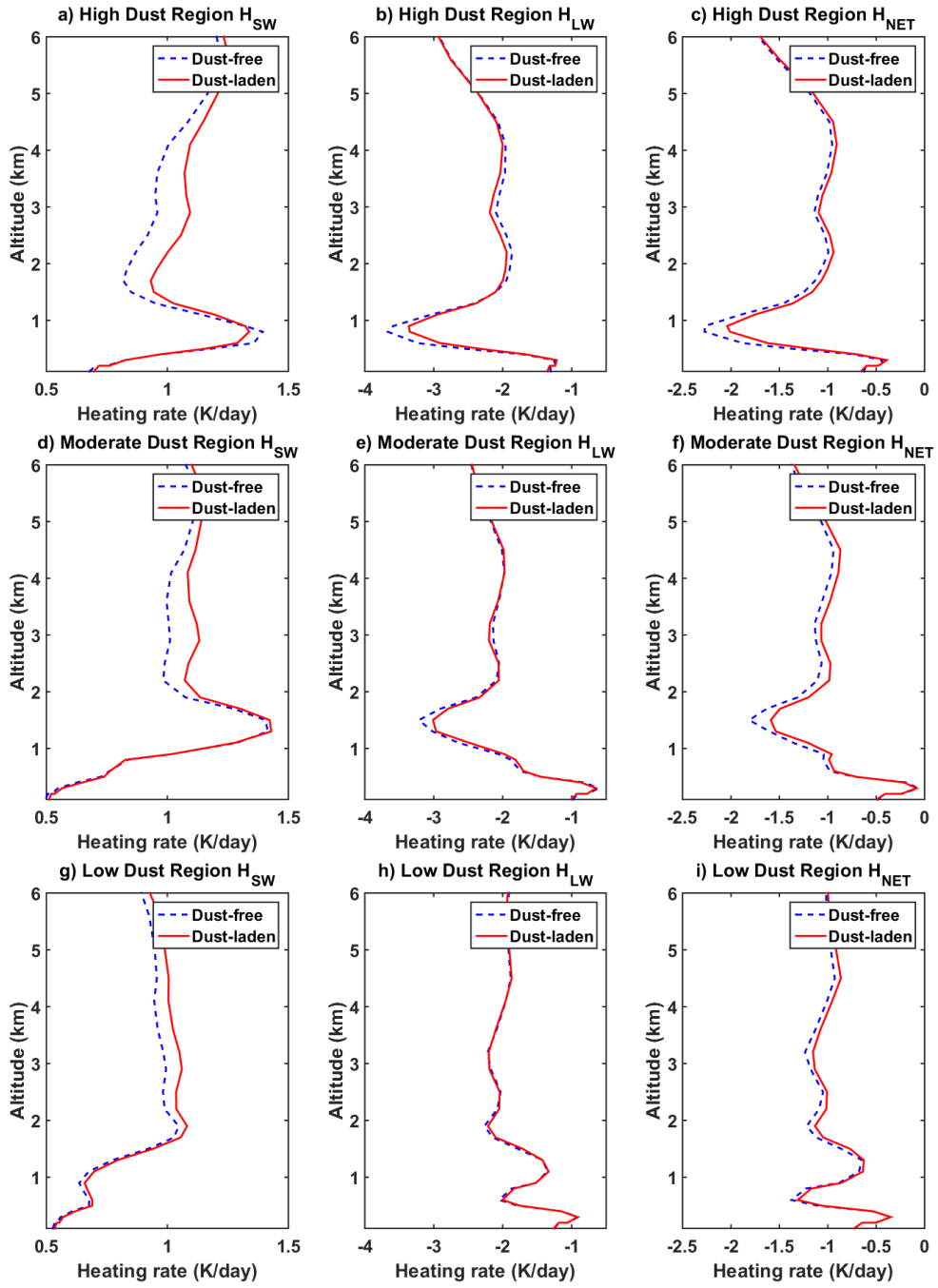

Figure 4.11 Mean vertical profiles (averaged over 0Z July 01 to 18Z July 31, 2010, and the respective regions) of the atmospheric heating rates (K/day) due to the shortwave (H_{SW}), longwave (H_{LW}), and net radiation (H_{NET}) in the high (0-25°N, 20-30°W; figures a-c), moderate (0-25°N, 30-40°W; figures d-f), and low (0-25°N, 40-50°W; figures g-i) dust regions. All the data are taken from the outputs of the experiment D36.

Generally, the shortwave cause atmospheric warming due to absorption and longwave give cooling through emission (D36A; dashed lines in figures 4.11a-i). In the presence of dust, both shortwave warming and longwave cooling become stronger, especially in the high and moderate dust regions (D36B; solid lines in figures 4.11a-i). In addition, as mentioned earlier, due to the role of dust similar to the greenhouse gases, longwave contribute to the warming through reduced cooling (e.g., 0.32 K/day less cooling at ~ 0.6 km in the high dust region; figure 4.11b), giving a net warming effect. These features of the heating rates are consistent with previous studies [e.g., *Zhu et al.*, 2007; *Naeger et al.*, 2013]. For example, *Zhu et al.* [2007] found that the dust induced heating rate perturbations off the Sharan coast at the peak dust altitude are +0.4 K/day and -0.5 K/day for the shortwave and longwave respectively.

The net effect of dust on the tropospheric temperature (T) not only depends on the changes in shortwave and longwave heating rates but also depends on the changes in other atmospheric processes that are sensitive to the radiative heating or cooling. In our simulations, these processes are: the heating and cooling due to the cloud microphysical processes (microphysics scheme), sub-grid scale moist processes (cumulus scheme), advection, and the turbulence and diffusion due to the boundary layer processes. Due to the complexities and mutual feedback of these processes, it is difficult to isolate the atmospheric temperature change that can directly be attributed to the dust radiative forcing. Nevertheless, to find the net dust impact on atmospheric temperature we analyze the time averaged (0Z July 01 to 18Z July 31, 2010) three dimensional distributions of dust mass mixing ratio (D; D36B), tropospheric temperature without dust [T(D36A], and the dust induced temperature perturbations [ΔT=T(D36B)-T(D36A); figure 4.12a-c]. As discussed earlier, the shortwave absorption and longwave trapping lead to the net warming, and therefore we find a certain increase of temperature below

the dust layers (figure 4.12c). These ΔT maxima (~ +0.3 K below ~1 km; figure 4.12c) are located at the north eastern part of the domain where dust concentration is highest. Apart from these maxima, temperature changes by dust are either very random or negligible elsewhere in the domain. We also examined the dust induced temperature changes in both day and night separately. There is no noticeable difference in the temperature perturbation by dust in day and night (figures not shown here).

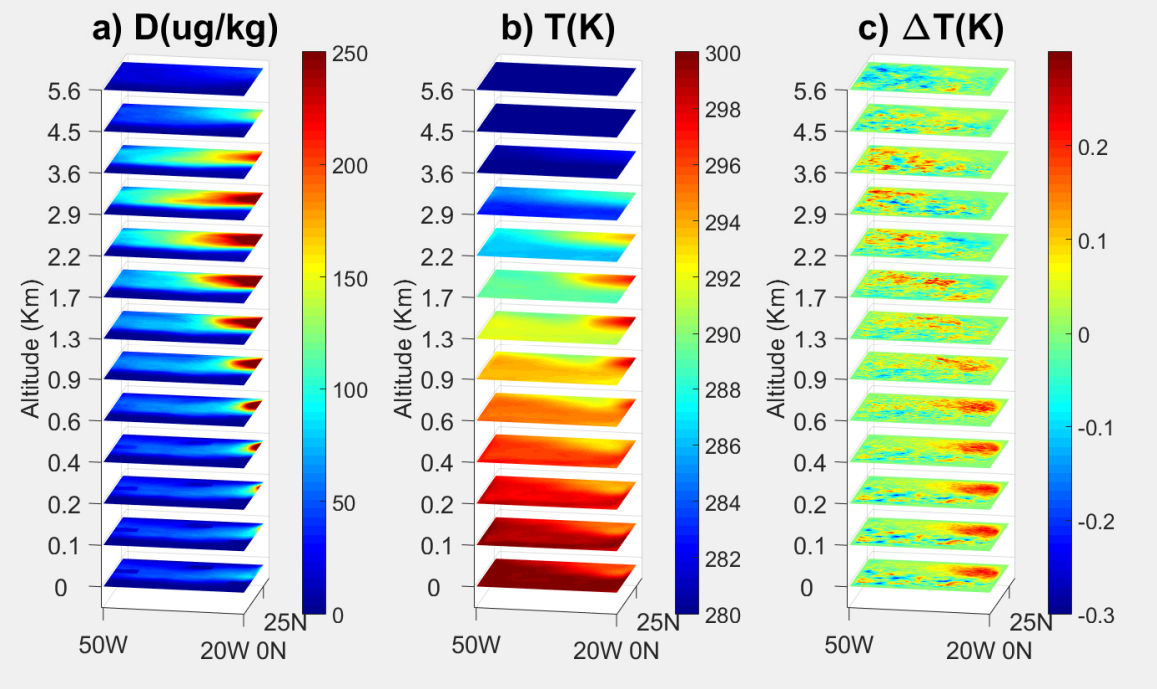

Figure 4.12 Monthly mean (0Z July 01 to 18Z July 31, 2012) distributions of the a) Dust mass mixing ratio (D; µg/kg), b) atmospheric temperature (T; K) without dust (D36A), and the c) dust induced temperature changes (ΔT; D36B-D36A) at different altitudes corresponding to the different model levels. All the data are taken from the experiment D36 with every 6 hour simulation outputs covering the domain: 0-25°N, 20-50°W.

4.4 Dust Effects on Surface Heat Fluxes and Cloud Cover

On a global scale, the dust negative radiative forcing at the SUR (surface dimming) is compensated primarily through the decrease of latent heat flux and secondarily through the

decrease of sensible heat flux [*Miller et al.*, 2004]. Regionally, the energy budget at the surface is the sum of the net radiative flux, sensible heat (SH) flux, latent heat (LH) flux and the ground heat flux into the surface that may eventually transferred out of the domain. Sensible and latent heat fluxes depend on the temperature, and the partial water vapor contrasts between the sea surface and the overlying air layer respectively. Here we discuss the sensitivity of the sensible and latent heat fluxes to the dust induced reduction of the surface radiative fluxes over the domain.

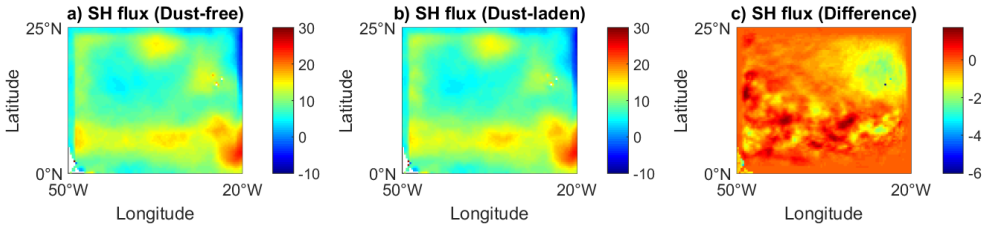

Figure 4.13 Monthly mean (0Z July 01 to 18Z July 31, 2010) horizontal fields of the Sensible heat fluxes (SH; W/m^2) a) without dust (D36A), b) with dust (D36B), and c) their difference (D36B-D36A). Heat fluxes are calculated from the accumulated values at the end of the simulation (18Z, July 31, 2010).

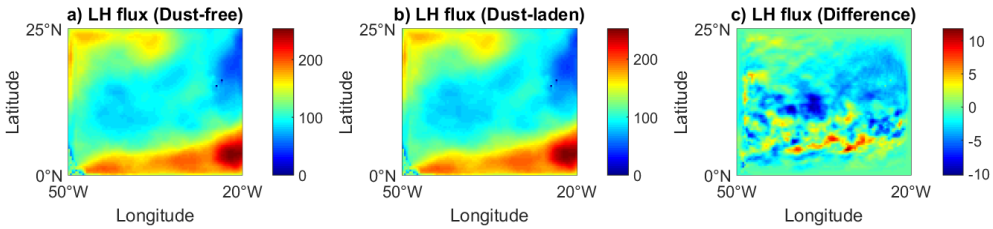

Figure 4.14 Same as figure 4.13, but for the latent heat fluxes (LH).

Figures 4.13a-c, and 4.14a-c present the horizontal distributions of the sensible and latent heat fluxes for D36A, D36B and their differences respectively. As the domain is mostly encompassed by the Ocean, the sensible heat flux is relatively smaller than the latent heat flux. We find that spatially and temporally averaged SH and LH fluxes reduced by only ~ -0.3 W/m^2 (3% decrease) and ~ -1.1 W/m^2 (1% decrease) respectively. In addition, there are no

significant changes in SH and LH flux patterns (figures 4.13c and 4.14c respectively) that can be collocated with the dust distribution (4.1a-d). Hence, there is no significant evidence of dust effects on the SH and LH fluxes during the one month period. Some of the previous studies on aerosol effects [*Shell and Somerville*, 2007; *Mallet et al.*, 2009] have reported more significant reduction of the surface heat fluxes in the presence of aerosols. However, it should be noted that in our case the Sea Surface Temperature (SST) was fixed during the model runs. Consequently, over the timescale of our simulation (one month) both the sensible and latent heat fluxes show very little sensitivity to the reduced radiative flux at the surface. We therefore argue that the dust induced surface dimming must have been compensated by the reduced energy transfer from the domain to the outside of the boundary.

As the water molecules are potent greenhouse gas, any perturbation of the atmospheric water vapor and the cloud cover can give significant feedback to the dust direct radiative forcing. Atmospheric heating rate change discussed in section 4.3 can influence the atmospheric circulation and stability that might affect the moisture and cloud amount. Here, we examine the effects of dust induced radiative forcing on the vertical profiles (time and domain averaged) of atmospheric water vapor mass mixing ratio (q) and the cloud fraction (C_F). We categorize the domain in terms of the dust abundance, as mentioned in section 4.3. We find that the impact of dust on the moisture is very negligible regardless of the regions and the time of the day in consideration (figures not shown here). However, the vertical profile of cloud fraction (fraction of the domain area with cloud water mass mixing ratio equal to or higher than 10^{-6} kg/kg) shown in figures 4.15a-f indicate that dust impact on cloud cover is relatively more significant compared to the moisture.

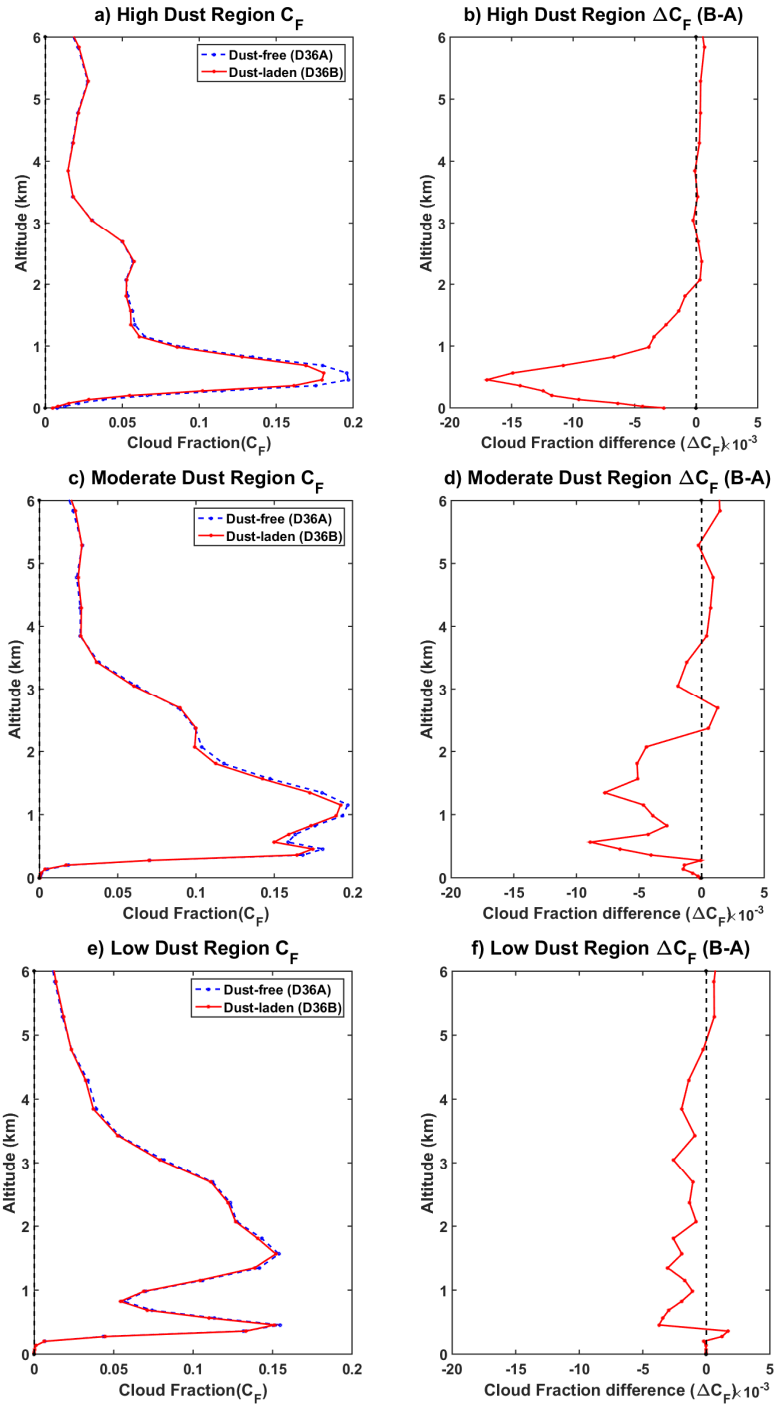

Figure 4.15 Mean vertical profiles (averaged over 0Z July 01 to 18Z July 31, 2010, and the respective regions) of the cloud fractions (fraction of the grid cells with cloud mass mixing ratio higher than or equal to 1e^{-6} g/kg; C_F) without (D36A) and with dust (D36B), and their difference (D36B-D36A) for the high (0-25°N, 20-30°W; figures a-b), moderate (0-25°N, 30-40°W; figures c-d), and low (0-25°N, 40-50°W; figures e-f) dust regions. All the data are taken from the outputs of the experiment D36.

Horizontal area covered by cloud is reduced by up to 9% (~ 0.5 km), 5% (~ 0.6 km), and 2% (at ~ 0.5 km) in the high, moderate and low dust regions (figures 4.15a-f). In the upper level, dust impact on cloud is negligible. This clearly suggests that the reduction of cloud cover is the result of the convection inhibition below the dust layer and discussed further in next chapter.

4.5 Dust Direct Effect with the Cloud Feedback

Cloud feedback to the net radiative budget is dependent on the cloud cover change and the position of the dust layer relative to the cloud. Dust induced reduction of cloud cover reduces the atmospheric albedo that eventually reduces the outgoing shortwave radiation. In addition, presence of dust layer above warm phase cloud reduces the outgoing shortwave radiation as the dust layers absorb the SW reflected from the cloud layer beneath [*Naeger et al.*, 2013]. Schematic diagrams of the quantitative comparison of all the radiative flux components in the presence of cloud (all sky conditions) from the D36 simulations are shown in figure 4.16. Reduced outgoing shortwave flux (positive forcing) at the top of the atmosphere (due to the reduction of cloud cover) partly compensate the increased shortwave reflection by the dust layer (negative forcing). In addition, as the cloud fraction peak is beneath the dust loading peak, the dust layer retain some of the shortwave radiation reflected from the cloud underneath. Hence, at the TOA the net negative shortwave forcing by the dust including the cloud feedback reduces from -12 W/m^2 (figure 4.6) to -2 W/m^2 (figure 4.16). Consequently, the net radiative forcing at the top of the atmosphere (RF_{TOA}) reduces from -11 W/m^2 to -3 W/m^2. The radiative forcing of the atmosphere (RF_{ATM}) does not change due to cloud feedback and remains +3 W/m^2. With the decrease of cloud fraction, more shortwave radiation is allowed through the atmosphere towards the surface (positive forcing) that compensate the

dust induced shortwave attenuation at the surface (negative forcing). As a result, dust induced radiative forcing at the surface (RF_{SUR}) also becomes weaker (-5 W/m^2) with the cloud feedback.

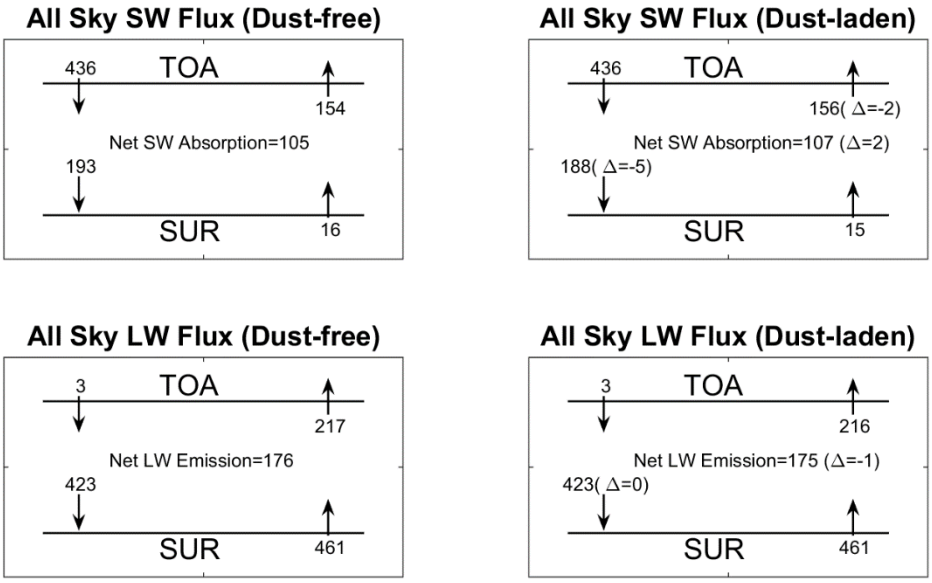

Figure 4.16 Schematic diagram of the time and domain averaged (0Z July 01 to 18Z July 31, 2010; 0-25°N, 20-50°W) radiative flux components (W/m^2) for all sky condition. All the data are taken from the outputs of the experiment D36.

Tables 4.1 and 4.2 summarize the domain averaged forcings for different cases and the net impact of the forcing on atmospheric and surface variables respectively. The radiative forcing from our experiment (table 4.1) show slight discrepancy with the results of *Zhu et al.* [2007]. The authors found that the all sky radiative forcing of dust off the African coast in June-August are +0.3 W/m^2, +9.16 W/m^2, and -8.86 W/m^2 at the TOA, ATM, and SUR respectively. We attribute this inconsistency to the differences in the domain coverage and the meteorological conditions between our case and that of *Zhu et al.* [2007].

Table 4.1 Radiative forcing (W/m^2) of the Atmosphere, Surface, and top of the atmosphere with (All sky) and without the cloud feedback (clear sky).

Radiative forcing	Clear Sky	All Sky
Atmosphere (RF_{ATM})	+3	+3
Surface (RF_{SUR})	-14	-5
Top of the Atmosphere (RF_{TOA})	-11	-3

Table 4.2 Domain averaged mean (0Z July 01 to 18Z July 31, 2010; 0-25°N, 20-50°W) changes in atmospheric and surface variables by the Saharan dust aerosols, considering only the dust direct effect.

Variable	Daytime Average (July)	Nighttime Average (July)	Month Average (July)
Shortwave heating rate (ΔH_{SW})	Maximum +0.21 K/day at 2.9 km	None	Maximum +0.11 K/day at 2.9 km
Longwave heating rate (ΔH_{LW})	Maximum +0.16 K/day at 0.8 km	Maximum +0.14 K/day at 2.9 km	Maximum +0.14 K/day at 0.8 km
Net radiative heating rate (ΔH_{NET})	Maximum +0.17 K/day at 2.5 km	Maximum +0.14 K/day at 2.9 km	Maximum +0.13 K/day at 1.5 km
Surface Sensible Heat flux (ΔSH)	-0.31 W/m^2 (-3%)	-0.28 W/m^2 (-3%)	-0.31 W/m^2 (-3%)

Surface Latent Heat flux (ΔLH)	-1.1 W/m^2 (-1%)	-1.14 W/m^2 (-1%)	-1.2 W/m^2 (-1%)
Atmospheric Temperature (ΔT)	Maximum +0.03 K at 0.5 km	Maximum +0.03 K at 0.8 km	Maximum +0.03 K at 0.6 km
Water vapor mass mixing ratio (Δq)	No change	No change	No change
Cloud Fraction (ΔC_F)	Maximum -7% at 0.5 km	Maximum -4% at 0.6 km	Maximum -5% at 0.5 km

Chapter 5: Saharan Dust Effects on Cloud Microphysics

5.1 Dust vs. Other Aerosols: Results from the Sensitivity Tests

In this chapter, we explore the potential impacts of the dust aerosols on cloud microphysics and precipitation, commonly known as the aerosol indirect effects. We also analyze the dust induced changes of the radiative fluxes to estimate the radiative forcing due to the combination of both direct and indirect effects of the Saharan dust. It should be noted that the representations of the aerosol-cloud interactions in the model version used in this study (WRF-Chem 3.6.1) is only limited to the explicitly resolved cloud processes (e.g. condensation, coalescence etc.). Therefore, to investigate the dust effects on cloud and precipitation, primarily the finer resolution model runs (4 × 4 km; I04A and I04B) covering the smaller domain (d03; figure 3.1) are used. To quantify the radiative forcing due to both direct and indirect effects, we use the coarser resolution runs (36 × 36 km; I36A and I36B), so that the model domain (d01; figure 3.1) and the resolution are consistent with the direct effect case (D36), discussed in chapter 4. In addition to the analyses of these experiments, results from a series of sensitivity tests are also discussed in the current chapter (this section). Due to the higher computational burden in the finer resolution model runs, the sensitivity tests are conducted at 12 × 12 km resolution through July 1-7. The results of these sensitivity tests are discussed in the following.

Absorption and scattering of the radiation by the other aerosols (all aerosols excluding dust) in the domain were found to be negligible compared to the contributions of dust (discussed in the chapter 4; figures 4.2b-c). However, the microphysical effects of these aerosols such as

the sea salt might be comparable to the dust effects. Therefore, to identify the relative importance of various aerosols in cloud microphysics, we examine the sensitivity of the cloud mass and number concentration to the different aerosol types of the domain. To do this, a series of sensitivity tests are performed by removing one aerosol species (potential condensation nuclei) at a time from the total aerosol loadings. The initial and the boundary condition files of the model are modified to omit the following aerosols in each of these tests: Dust, Sea salt, SO_4, NO_3, Black Carbon (BC), and the Secondary Organic Aerosol (SOA). Results from these tests are presented in figures 5.1a-b.

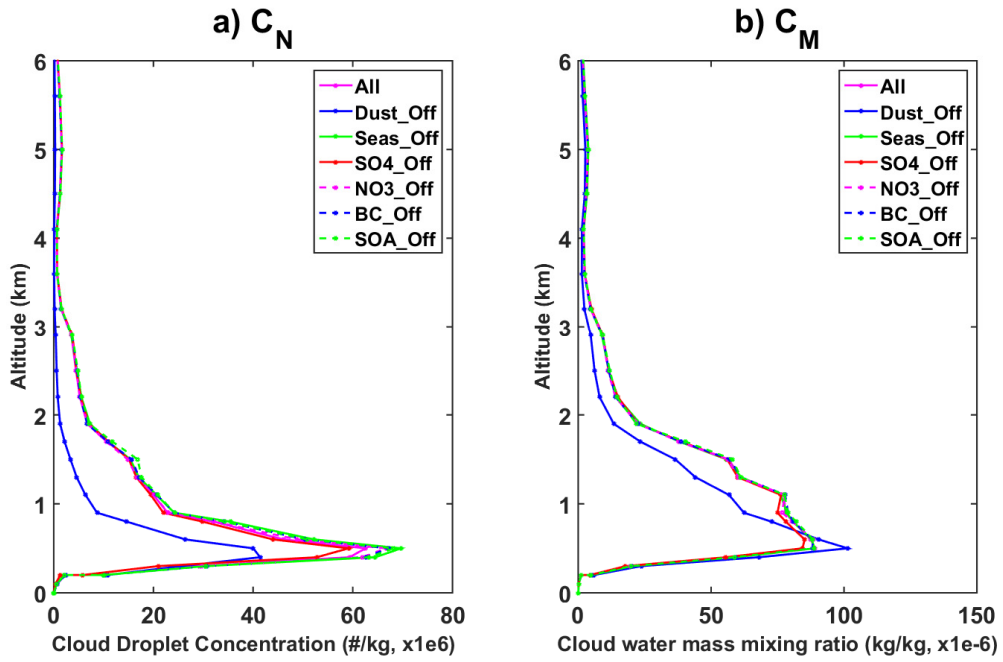

Figure 5.1 Time and domain averaged (0Z July 01 to 18Z July 10, 2010, and 10-25°N, 20-40°W) vertical profiles of the a) Cloud droplet number concentration (C_N), and b) Cloud water mass mixing ratio (C_M) from the sensitivity tests.

It is evident from the figures 5.1a-b that unlike the radiative effects, the microphysical effects of the other aerosols are not entirely negligible compared to that of dust. Nevertheless, both the cloud droplet number concentration (C_N; figure 5.1a) and the cloud water mass mixing

ratio (C_M; figure 5.1b) show most sensitivity to the dust aerosols. In the absence of dust, domain averaged cloud droplet number concentration is reduced by up to ~ 56% at ~ 0.5 km, compared to the 'all aerosol' case (figure 5.1a). Without dust, cloud water mass mixing ratio also decrease significantly above ~ 0.8 km having the maximum decrease of ~35% at ~ 1.1 km (figure 5.1b). Increase of C_M in lower levels (below ~ 0.8 km; figure 5.1b) is due to the weakening of the dust induced environmental instability underneath the maximum dust layer. Nevertheless, based on these results dust can be considered as the primary CCN in our domain. Analysis of the dust impacts on cloud microphysics, precipitation, moisture budget, and the net radiative forcing are discussed in the following sections respectively.

5.2 Dust Effects on Cloud Microphysics

Most of the previous studies on aerosol indirect effects [e.g., *Xue et al.*, 2008; *Saleeby et al.*, 2015] have reported various aspects of the aerosol impacts on cloud microphysics, which are based on the 'idealized' model simulations. Here we investigate the influence of the Saharan dust aerosols on cloud microphysics based on high resolution 'real' simulation data (experiment I04; smaller domain). The vertical profiles of the spatial and temporal average (2.5-11.5°N, 30-40°W and 0Z July 06 to 18Z July 13, 2010) of the cloud droplet number concentration (C_N) and the cloud water mass mixing ratio (C_M) from I04 and also their respective changes by dust (I04B-I04A) are shown in figures 5.2a-b and 5.3a-b respectively. Availability of dust as CCN lead to more droplet condensation. As a result, the cloud droplet number concentration is increased in almost every altitudes with the maximum increase of ~ 53% at ~ 0.6 km (figures 5.2a-b). The cloud water mass mixing ratio show both increase and decrease in different altitudes. It is increased beyond 1 km, with maximum increase of ~ 13% at ~ 1.5 km (figures 5.3a-b). The reduction of the cloud water is found in lower levels (below

~1 km) with the maximum cloud reduction of ~ 11% occurring at ~ 0.5 km (figures 5.3a-b). These features of cloud response to the aerosol indirect effects are consistent with *Saleeby et al.* [2015].

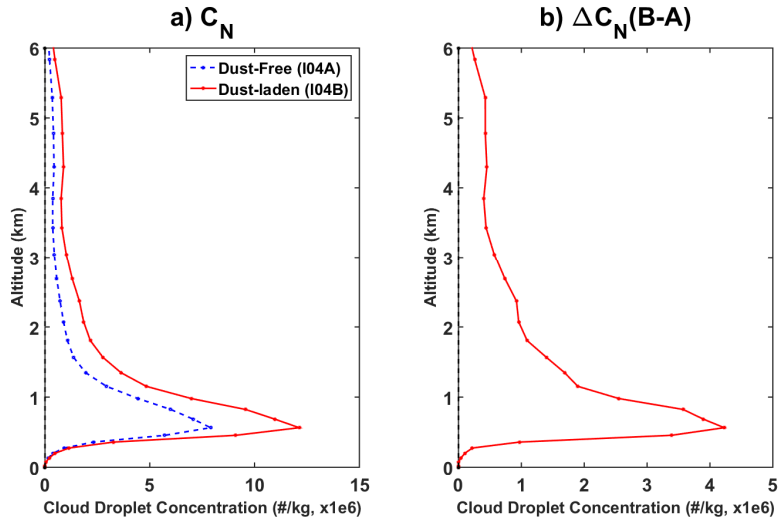

Figure 5.2 Time and domain averaged (0Z July 06 to 18Z July 13, 2010, and 2.5-11.5°N, 30-40°W) vertical profiles of the a) Cloud water number concentration (C_N) from the Dust-Free (I04A) and Dust-laden (I04B) runs, and the b) dust induced changes (I04B-I04A) of the Cloud water number concentration (ΔC_N).

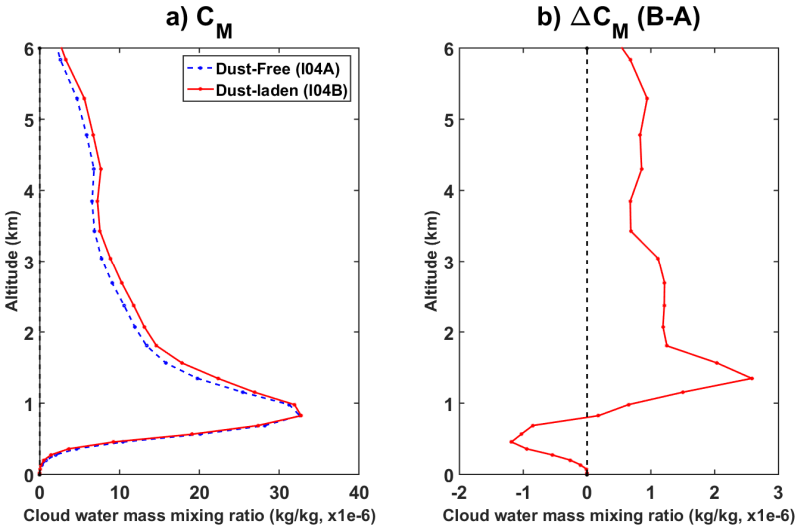

Figure 5.3 Time and domain averaged (0Z July 06 to 18Z July 13, 2010, and 2.5-11.5°N, 30-40°W) vertical profiles of the a) Cloud water mass mixing ratio (C_M) from the Dust-Free (I04A) and Dust-laden (I04B) runs, and the b) dust induced changes (I04B-I04A) of the Cloud water mass mixing ratio (ΔC_M).

As discussed in chapter 4, dust is a strong absorber of the shortwave radiation. In addition, dust layers also trap the longwave radiation emitted from the surface, causing a net warming at ~ 1 km. This strengthens the convection beyond 1 km and lead to more condensation above this level giving cloud enhancement. Past studies have attributed the reduction of the cloud water to the aerosol induced weaker conditional instability due to suppressed precipitation and less rain evaporation [*Stevens et al.*, 1998; *Saleeby et al.*, 2015]. However, the reduction of the low level cloud in our case (figure 5.3a-b) is due to the weaker instability caused by the dust induced heating that inhibits convection below ~1 km. This is discussed further in section 5.4.

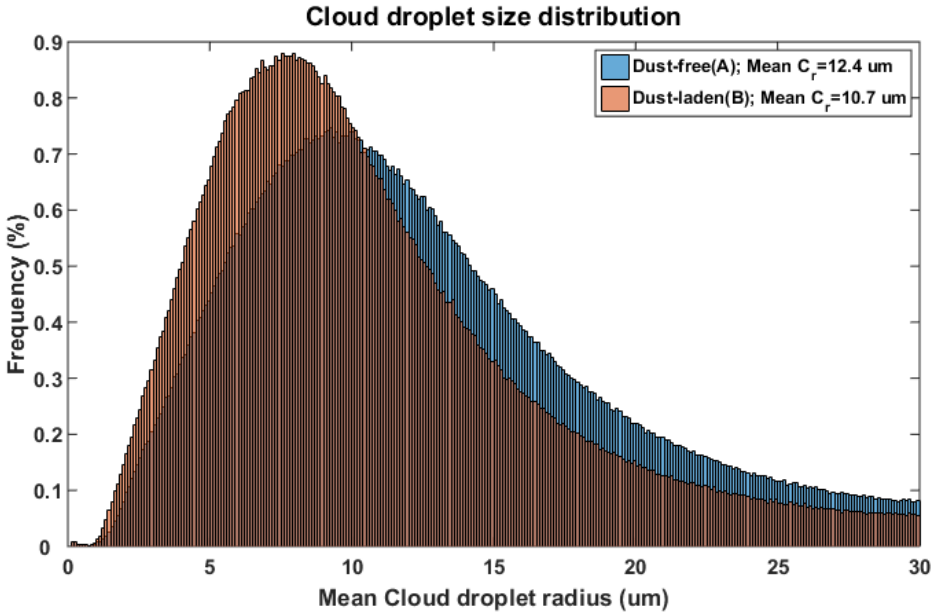

Figure 5.4 Cloud droplet size distributions (droplet radius; C_r) from the dust-free (I04A) and the dust-laden (I04B) runs.

Cloud droplet radius (C_r) is an important parameter for climate, as it determines the relationship between cloud Liquid Water Path (LWP) and its albedo [*Bréon and Colzy*, 2000]. Presence of aerosols lead to increased cloud droplet number concentration with the reduced

droplet size [*Twomey*, 1977] which is known as the first aerosol indirect effect. Histogram of the cloud droplet size distributions from experiment I04 are shown in figure 5.4. Droplet radii in the domain are mostly within 1-30 μm for both runs: I04A and I04B. Despite the variations in droplet sizes, it is evident that the size distribution is shifted towards the smaller size in the run 'I04B' indicating that relatively smaller cloud droplets are produced in the presence of dust. Mean cloud droplet radius is 12.4 μm without dust (I04A), which is reduced to 10.7 μm (~ 14% reduction) with the inclusion of dust as a CCN (I04B). Vertical distributions of the droplet sizes from both runs are also examined (figure not shown here), however there is no significant variation of the droplet sizes amongst different vertical levels. Formation of smaller cloud droplets in the presence of the Saharan dust is consistent with the findings of *Rosenfeld et al.* [2001]. East Asian dust aerosols are also reported to affect the droplet sizes [*Ou et al.*, 2012] and follows the 'Twomey effect'. However, production of smaller cloud droplets does not necessarily enhance the cloud cover (and hence albedo) due to the change of the cloud LWP. This is discussed in the following.

Aerosol induced changes of the condensation, dynamics, and the interactions amongst the cloud droplets determine the cloud LWP responses to the aerosol loading [*Lee et al.*, 2009]. Previous studies have found both increase and decrease of the LWP with the increase of aerosol concentration [*Han et al.*, 2002]. Figures 5.5a-c present the horizontal distributions of the Cloud LWP from I04A, I04B, and their difference respectively. Most of the domain is covered with low LWP (~ 0.05 mm) indicating the domain wide presence of the shallow marine cumulus cloud (figures 5.5a-b). Inclusion of the dust give both the enhancement and reduction of cloud LWP (figure 5.5c) all over the domain. Increase of LWP is attributed to the slower coalescence of droplets that suppress the precipitation [*Ackerman et al.*, 2004],

whereas the decrease of LWP is due to the enhanced entrainment and evaporation of cloud droplets [*Ackerman et al.*, 2004; *Tao et al.*, 2012]. Nevertheless, averaged over the domain, overall change of the LWP is an increase of ~ 7.3 %. Figure 5.6 shows the percentage contribution of different LWP bins to the total LWP. We find that in the presence of dust, there is a shift from the thinner cloud (LWP ~ 0.05 mm) to relatively thicker cloud (LWP > 0.07 mm), which is consistent with the results from *Saleeby et al.* [2015].

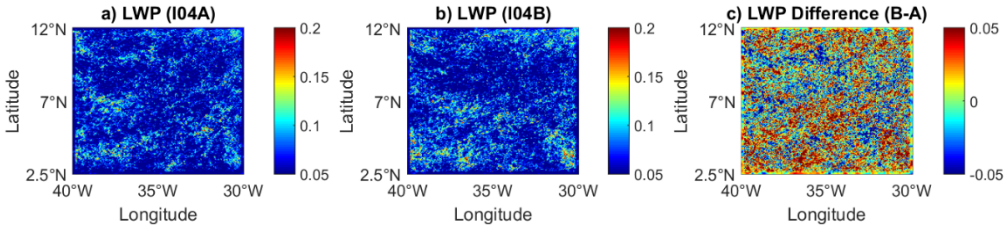

Figure 5.5 Time averaged (0Z July 06 to 18Z July 13, 2010) horizontal distributions of the Cloud Liquid Water Path (LWP) a) without dust (I04A), b) with dust (I04B), and the c) dust induced changes (I04B-I04A).

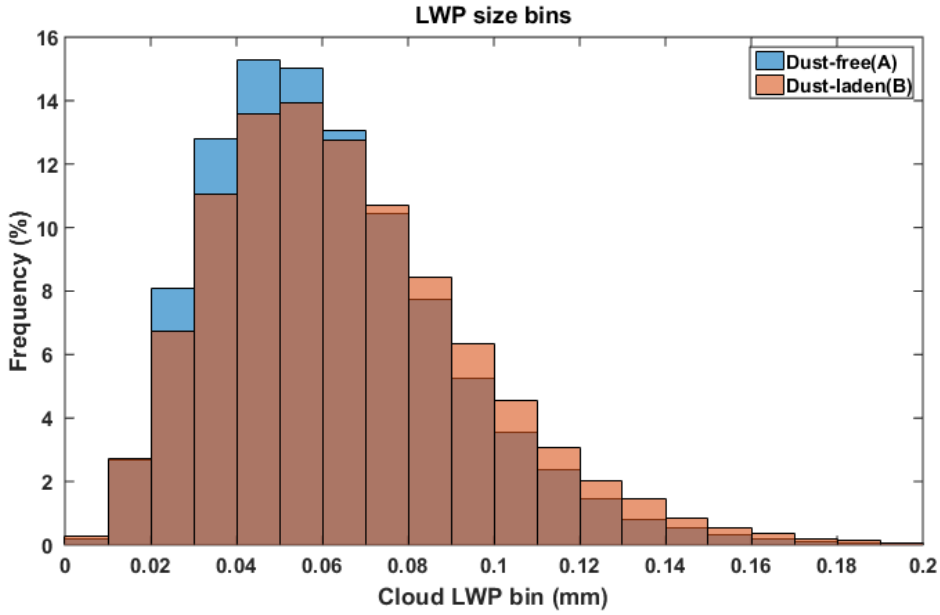

Figure 5.6 Percentage contributions (normalized) to the total Cloud Liquid Water Path (LWP) from discrete size bins. All the data correspond to the experiment I04.

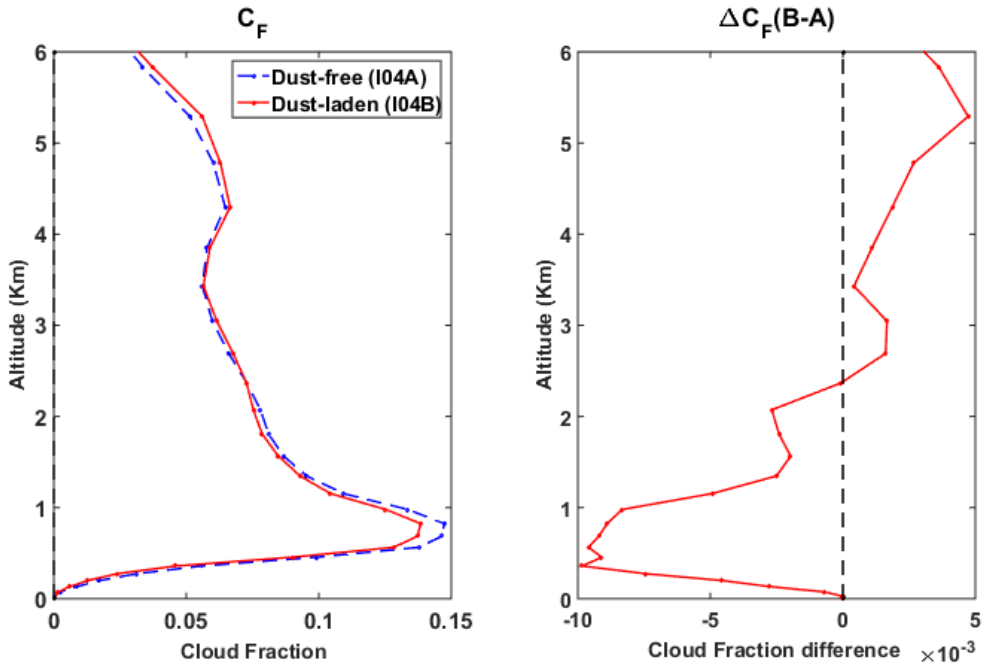

Figure 5.7 Mean vertical profiles (0Z July 06 to 18Z July 13, 2010, and 2.5-11.5°N, 30-40°W) of the a) Cloud fractions (fraction of the grid cells with cloud mass mixing ratio higher than or equal to 1e-6 kg/kg; C_F) from I04A and I04B, and b) their difference (ΔC_F).

Cloud fraction (C_F) determines the radiative feedback of the cloud. Opposing effects of aerosol induced precipitation suppression and droplet evaporation influence the cloud fraction [*Xue et al.*, 2008]. Mean (time and domain averaged) vertical profiles of the cloud fraction from I04 (fraction of the domain area having the cloud water mass mixing ratio equal to or more than 10^{-6} kg/kg) and the changes by dust (I04B-I04A) are shown in figures 5.7a-b. Dust reduce (enhance) the horizontal cloudy area below (above) ~2.5 km. Cloud fraction reduction is up to 17% (at ~ 0.4 km) and enhancement is up to 9% (at ~ 5.6 km). However, the cloud fraction in the lower level is higher (~ 0.15), and therefore the lower level reduction outweighs the upper level cloud fraction enhancement. As a result, the overall horizontal area of the domain covered with cloud (represented by the area under the curve; figure 5.7a) is reduced in the presence of dust. This affects the reflectance of the solar radiation and the shielding of

the upwelling thermal radiation emitted from the surface. Lower level bright clouds have strong cooling effect due to shortwave reflection, whereas high clouds have warming effect due to strong longwave trapping [*Rosenfeld et al.*, 2014]. Therefore, despite the increase of the cloud amount (LWP) mentioned earlier, the cloud radiative forcing change is positive (discussed in section 5.5) owing to the overall reduction of the number of cloudy grid cells in the domain. Coarser resolution runs (I36A and I36B) also give similar results (figures not shown here). It should be noted that, the cloud cover enhancement in the upper levels was negligible in D36 where only the radiative effects of dust were considered. This is due to the fact that the enhancement of cloud is not only related to the dust induced warming that lead to stronger convection in upper levels but also the result of the abundance of CCN that produce more condensation.

5.3 Dust Effects on Precipitation Properties and the Moisture Budget

Modulation of the cloud droplet size affects the coalescence process of the cloud droplets and consequently affects the rain production rate. Time and domain averaged Raindrop number concentration (R_N) and the Rain water mass mixing ratio (R_M) vertical profiles and their respective changes by dust (I04B-I04A) are shown in figures 5.8a-b and figures 5.9a-b respectively. Both of these quantities are reduced in the presence of dust. Maximum reduction of the raindrop number concentration is up to ~ 42% at ~1.3 km altitude (figures 5.8a-b), and the maximum raindrop mass mixing ratio is reduced up to ~11% at ~0.9 km (figures 5.9a-b). Reduction of the raindrop numbers and also the rainwater, can be attributed to the weakening of the aerosol induced droplet self-collection efficiency [*Ramanathan et al.*, 2001; *Saleeby et al.*, 2015].

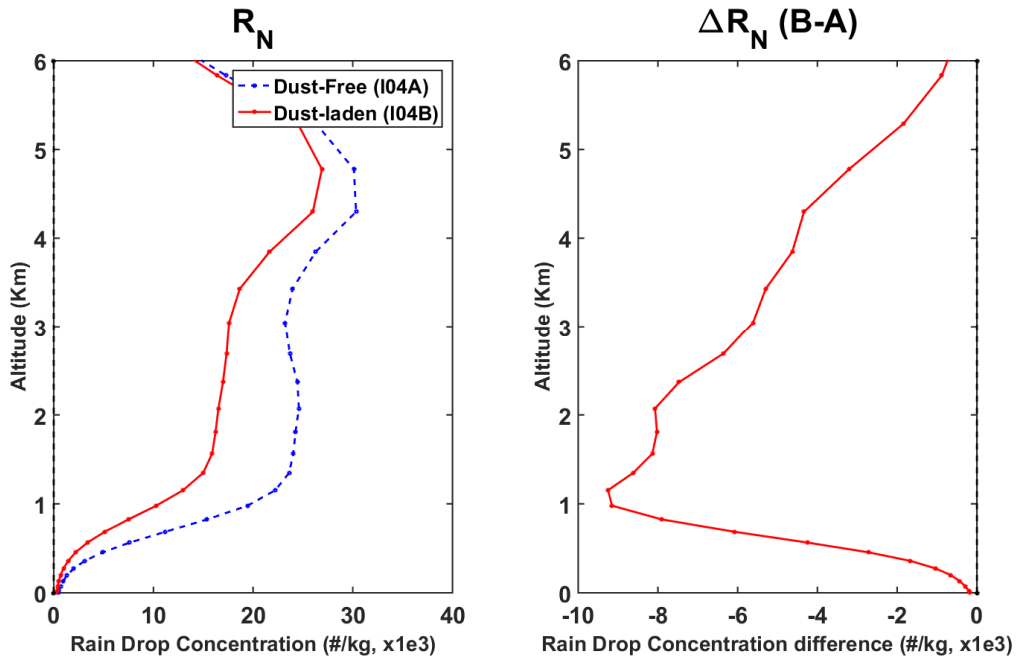

Figure 5.8 Mean vertical profiles (0Z July 06 to 18Z July 13, 2010, and 2.5-11.5°N, 30-40°W) of the a) raindrop number concentrations ($R_N \times 10^3$; #/kg of air) from I04A and I04B, and b) their difference($\Delta R_N \times 10^3$; #/kg of air).

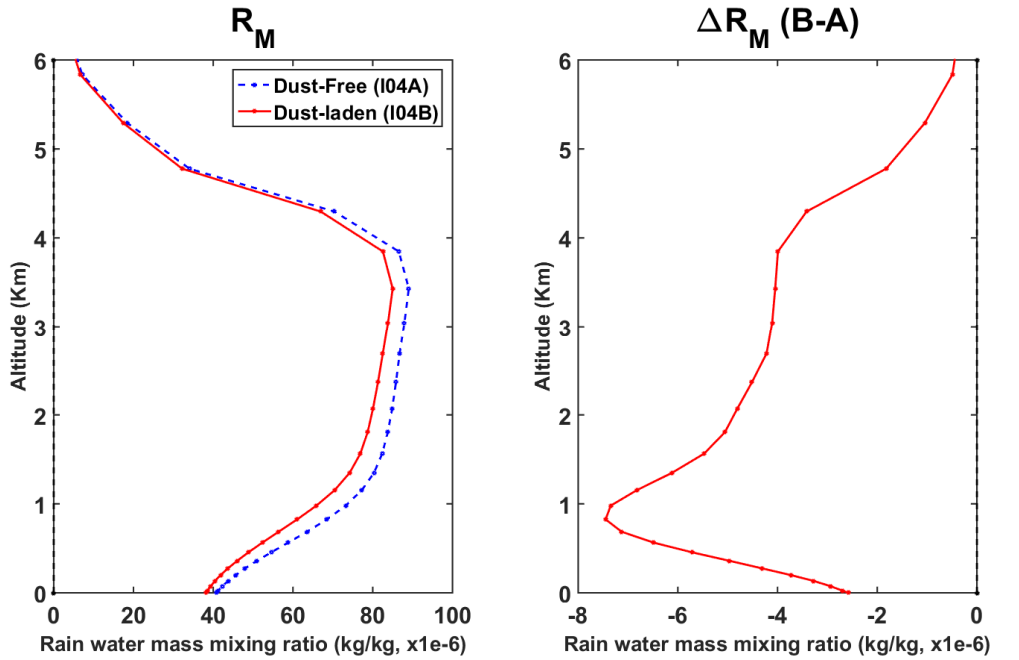

Figure 5.9 Mean vertical profiles (0Z July 06 to 18Z July 13, 2010, and 2.5-11.5°N, 30-40°W) of the (a) rain water mass mixing ratio ($R_M \times 10^{-6}$; kg/kg of air) from I04A and I04B, and b) their difference ($R_M \times 10^{-6}$; kg/kg of air).

The reduction of the raindrop number concentration and rain water mass mixing ratio can be attributed to the slower droplet self-collection process. Drizzle drops, which are larger than the cloud droplets are the precursors of the raindrops. The drizzle drops are primarily produced by the collision of small cloud droplets [e.g., *Hsieh et al.*, 2009]. These collision of the smaller cloud droplets can also produce larger cloud droplets which are smaller than the critical size of a drizzle drop, and this process is referred as the droplet self-collection process. Smaller cloud droplets are ineffective in collision due to lower fall speed and smaller collision efficiency [*Tao et al.*, 2012]. Due to the decrease of the cloud droplet size discussed in the previous section, the droplet self-collection process become slower. This reduces the raindrop production rate (figure not shown here) which consequently reduce the rainwater number concentration and rain water mass mixing ratio. The raindrop size is also affected (~ 1% increase; figure not shown here) although it is not very significant compared to the other studies [*Altaratz et al.*, 2008; *Lee et al.*, 2009; *Saleeby et al.*, 2015].

While the raindrops become larger, their surface to volume ratio decreases that reduce the likelihood of the rain evaporation [*Berg et al.*, 2008; *Saleeby et al.*, 2015]. Figures 5.10a-b show the time and domain averaged vertical profiles of the raindrop evaporation rates (E_R) and the dust induced changes (I04B-I04A) respectively. It is evident that, in the presence of dust the raindrop evaporation rate is smaller in any altitude. The peak of the rain evaporation change is at ~ 1.5 km where the evaporation is reduced by 11% (figure 5.10b).

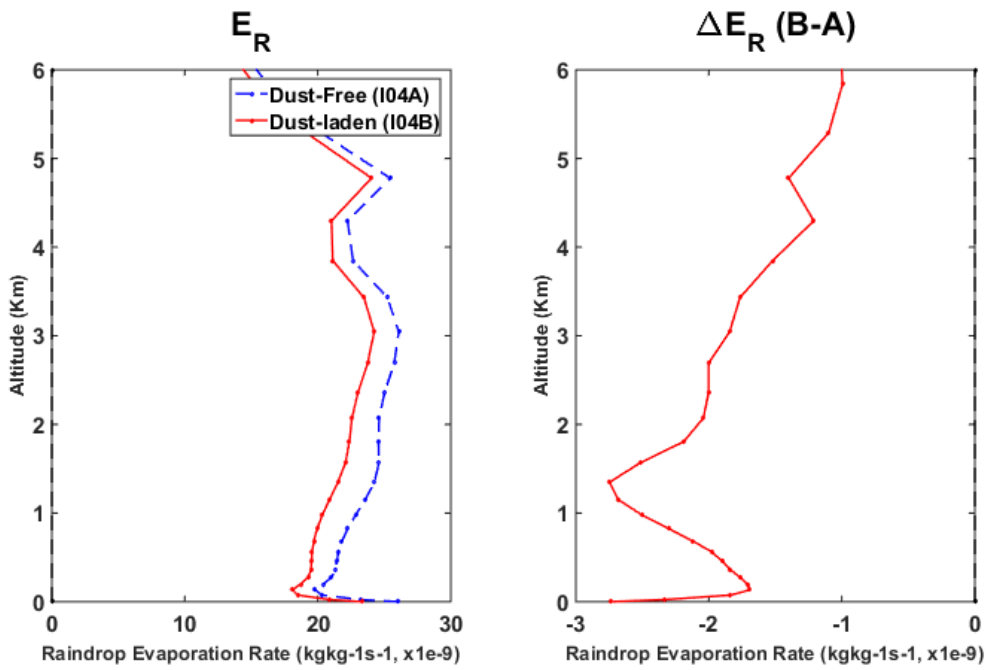

Figure 5.10 Mean vertical profiles (0Z July 06 to 18Z July 13, 2010, and 2.5-11.5°N, 30-40°W) of the a) raindrop evaporation rate ($E_R \times 10^{-9}$; kg kg^{-1}s^{-1}) from I04A and I04B, and b) their difference ($\Delta E_R \times 10^{-9}$; kg kg^{-1}s^{-1}).

Some of the previous studies on aerosol indirect effects have reported a delay in the beginning of the precipitation due to the inefficient collision coalescence process (auto conversion) of the cloud droplets that lead to longer cloud lifetime and suppressed precipitation [e.g., *Kaufeld and Nesbitt*, 2009; *Rosenfeld et al.*, 2001; *Givati and Rosenfeld*, 2004; *Lee et al.*, 2009]. This is known as the aerosol second indirect effect. In such a case, the time series of the total accumulated precipitation at the surface show a time lag in the presence of aerosols. We examine the time evolutions of the domain averaged conditional (only the grid cells with precipitation) accumulated precipitation rate at the surface from both I04A and I04B, as shown in figure 5.11. We see that there is a consistent and nearly monotonic trend in the precipitation rates from both 'A' and 'B'. However, we do not find any conclusive evidence of the time delay in the surface accumulated precipitation with the presence of dust (I04B). To investigate

this further, we have also conducted new sets of experiments with the same model configuration of I04 but for different time periods (July 1-3) and with more frequent outputs (30 minutes). Results of these tests (not shown) are consistent with the findings from I04 i.e. there is no delay in the onset of precipitation in the presence of dust. This could be due to the opposing effects of the precipitation suppression and the reduced rain evaporation. It should be noted that some studies also reported the increase of precipitation with increasing aerosol loading [*Lee and Yum*, 2012; *Zhou et al.*, 2017] and the detailed mechanism of the aerosol-precipitation interaction is not very clear yet.

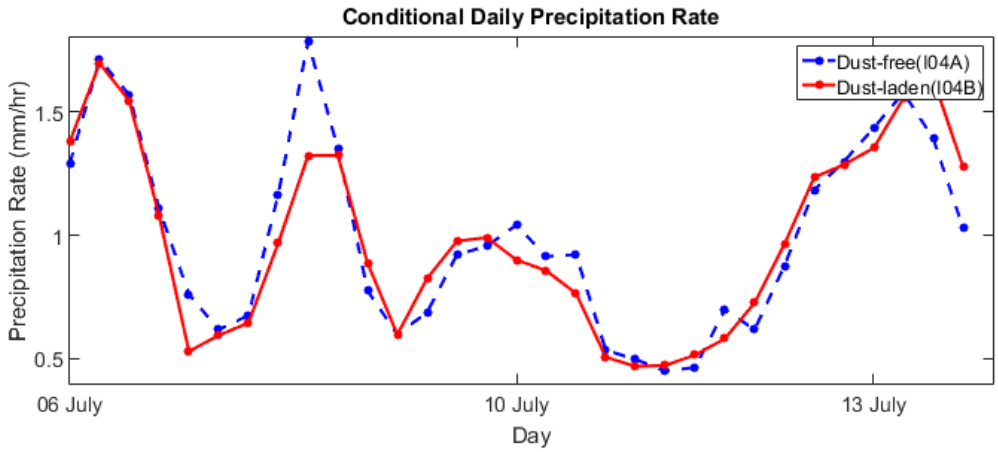

Figure 5.11 Conditionally averaged (considering only the precipitating grid cells over the domain: 2.5-11.5°N, 30-40°W) explicitly resolved precipitation rate time series. All the data correspond to the experiment I04.

On a regional scale, atmospheric moisture budget depends on the accumulated precipitation at the surface, water vapor evaporation from the surface, and the vertically integrated horizontal advection of the water vapor fluxes. Balancing water budget terms, especially in regional scale is very challenging [*Brown and Kummerow*, 2013]. Nevertheless, here we examine the dust influence on the individual moisture budget components. We assume that all the condensed water precipitate to the surface within the timescale of the simulation. In the

absence of dust, mean (spatially and temporally averaged) surface evaporation and precipitation rates over the domain are 4.5 mm/day, and 21.0 mm/day respectively (figures not shown here). The precipitation rate surpasses the evaporation rate significantly as the domain covers the ITCZ [e.g., *Wong and Dessler*, 2005]. Mean zonal and meridional water vapor divergence fluxes for the domain without the dust are 3.0 mm/day and 3.7 mm/day respectively (figures not shown here).

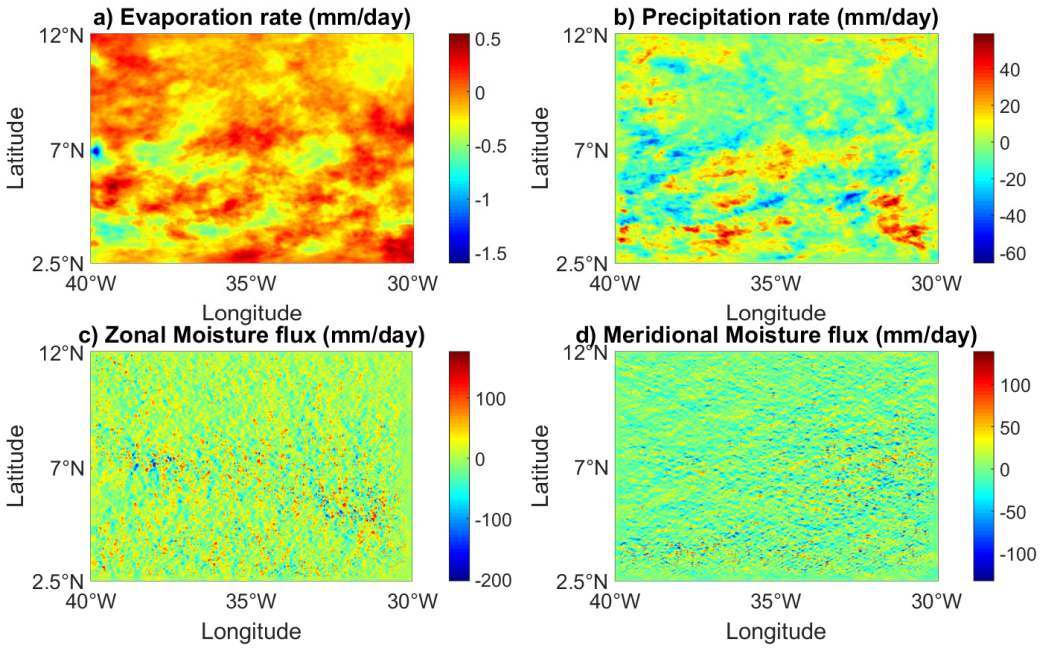

Figure 5.12 Time averaged (0Z July 06 to 18Z July 13, 2010) horizontal distributions of the dust induced changes (I04B-I04A) of the a) water vapor evaporation rate from the surface (mm/day), b) accumulated precipitation rate at the surface (mm/day), c) vertically integrated zonal moisture flux (mm/day), and d) vertically integrated meridional moisture flux (mm/day). All the data correspond to the experiment I04.

Dust induced perturbations (I04B-I04A) of the four individual moisture budget components are shown in figures 5.12a-d. All of the four components of the moisture budget show both increase and decrease with dust throughout the domain. However, mean changes are negligible in all cases. Domain averaged water vapor evaporation rate from the surface and

the accumulated precipitation rate both are reduced by only 1%. The mean zonal and meridional water vapor divergence fluxes also do not show any changes with the inclusion of dust. Therefore, it is clear that the moisture tendency terms are unaffected by dust effects for the small domain. However, the responses of all of these components are more significant over the larger domain where they are reduced in the presence of dust (results are summarized in the table 5.1 in the next section).

5.4 Dust Effects on the Surface Convergence and Buoyancy

As discussed in section 5.2, dust affects the convection and reduce (enhance) the cloud amount below (above) the dust layers. Here we investigate the possible pathways that lead to the modulation of convection. *Fan et al.* [2008] suggested that the reduction of the surface radiative fluxes reduce the surface heat fluxes which suppresses convection. However, as discussed in chapter 4, the dust induced changes of the surface heat fluxes in our domain are very mild, and therefore, cannot be the major factor suppressing the convection. *Saleeby et al.* [2015] attributed the changes in convection to the weaker conditional instability caused by the aerosol induced suppression of precipitation and reduced rain evaporation. They reported that the reduction of the surface convergence energize the low level cumulus clouds. Here, we examine the effects of dust in the surface convergence that may have influence on the convection and modulate the cloud fields in our experiments. Following the approach of *Wong and Dessler* [2005], the surface convergence is calculated from the difference between the vertical velocities of the two lowermost model half-levels. Therefore, the positive values represent low level convergence and an upward motion and vice versa. It should be noted that any sub-grid scale (< 4 km) convergence are not represented in the calculation. Given this limitation, we find that the fraction of the domain with the strong convergence ($>10^{-4}$ s^{-1}) is

reduced by 4% in the presence of dust implying that dust reduce the strength of the convergence in some of the grid cells (figures not shown here). However, the mean surface convergence of the domain (~10^{-5} s^{-1}) is reduced by only less than 1% with the dust. In addition, there are no notable correlations between the dust distributions and the changes in the convergence fields (figures not shown here). Hence, we argue that the surface convergence is not linked to the suppression of convection in lower levels. We suggest that the dust induced changes in convection is primarily related to the dust heating in the lower levels that modulates the instability. To verify this, we analyze the buoyancy contrast in two different vertical regimes. Figures 5.13a-b show the buoyancy from I04A and I04B for the model levels 1-10 (0 to 0.8 km) and 11-20 (0.8 km to 3.2 km) respectively. It is clear that the simulation with dust (I04B) have weaker buoyancy values in lower levels and stronger values in upper levels. These changes of buoyancy affects the net condensation and results the cloud reduction in lower levels and enhancement in the upper levels.

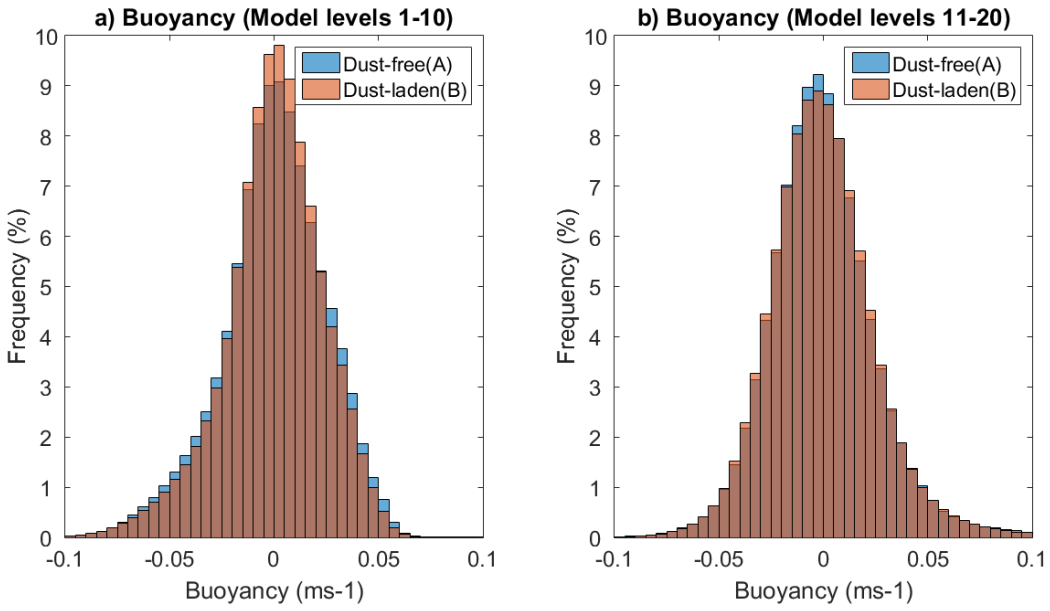

Figure 5.13 Histograms of the buoyancy (ms^{-1}) distributions for model levels a) 1-10 (0 – 0.8 km), and b) 11-20 (0.8 – 3.2 km). All the data correspond to the experiment I04.

We have also investigated other variables such as the latent heating, updraft and downdraft, but no significant dust induced changes of these variables are found. Table 5.1 summarizes the changes of these variables, as well as all the other variables analyzed in this chapter of the study. We also include the results from the coarser resolution runs (I36), which generally shows good consistency with the finer resolution runs (I04).

Table 5.1 Spatially and temporally averaged changes in atmospheric and surface variables by the Saharan dust aerosols, considering both dust direct and indirect effects. Results are averaged over 2.5-12°N, 30-40°W and 0Z July 06 -18Z July 13 for the finer resolution runs (I04), and over 0-25°N, 20-50°W and 0Z July 01 - 18Z July 31 for the coarser resolution runs (I36).

Variable	Results from I36	Results from I04
Cloud mass mixing ratio (C_M)	Decreased below dust layer, increased inside and above the dust layer Maximum: +26% at 1.7 km Minimum: -16% at 0.6 km	Decreased below dust layer, increased inside and above the dust layer Maximum: +13% at 1.5 km Minimum: -11%at 0.5 km
Cloud droplet number concentration (C_N)	Increased Maximum: 98% at 1.5 km	Increased Maximum:53% at 0.6 km
Cloud droplet radius (C_r)	Decreased A: 8.1 μm	Decreased A: 12.4 μm

	B: 7.3 μm, -10% reduction	B: 10.7 μm, -14% reduction
Cloud liquid water path (LWP)	Increased A: 0.063 mm, B: 0.068 mm +7.3% increase	Increased A: 0.061 mm, B: 0.066 mm +7.5% increase
Cloud Fraction (C_F)	Decreased below dust layer, increased inside and above the dust layer Maximum: +5% at 2.5 km Minimum: -9% at 0.5 km	Decreased below dust layer, increased inside and above the dust layer Maximum: +9% at 5.6 km Minimum: -17% at 0.4 km
Rain water mass mixing ratio (R_M)	Decreased Maximum: -9% at 1.5 km	Decreased Maximum: -11% at 0.9 km
Rainwater number concentration (R_N)	Decreased Maximum: -34% at 1.5 km	Decreased Maximum: -42% at 1.3 km
Raindrop radius (R_r)	No significant change A: 0.4288 mm B: 0.4333 mm, only ~1% increase	No significant change A: 0.45 mm B: 0.44mm, only ~2% decrease
Rain evaporation rate (E_R)	Decreased Maximum: -11% at 0.8 km	Decreased Maximum: -11% at 1.5 km
Precipitation rate (P)	No delay	No delay
Moisture budget	Water vapor evaporation from surface: -3%	Water vapor evaporation from surface: -1%

	Accumulated Precipitation rate: -4% Zonal moisture flux: -4% Meridional moisture flux: -9%	Accumulated Precipitation rate: -1% Zonal moisture flux: 0% Meridional moisture flux: 0%
Convergence	Decreased -5% with convergence stronger than 10^{-4} s^{-1}	Decreased -4% with convergence stronger than 10^{-4} s^{-1}
Buoyancy	Weaker in the lower levels, no change in upper levels	Weaker in the lower levels and stronger in the upper levels

5.5 Net Dust Radiative Forcing: Direct and Indirect Effects

It was discussed in chapter 4 that the direct effect of dust in cloud-free condition is positive inside the atmosphere (ATM), and negative at both the top of the atmosphere (TOA) and surface (SUR). The atmospheric warming reduce the cloud cover in lower levels, that significantly weakens the negative forcing at the TOA and SUR. In this chapter, we have explored the dust indirect effects and found that dust not only reduce cloud cover in lower levels but also enhances in the upper levels when both direct and indirect effects are considered together. In this section, we discuss the radiative forcing of dust caused by both direct and indirect effects.

As shown in table 5.1, the major features of the dust indirect effects are consistent between the coarser (I36) and finer (I04) resolution model runs. Therefore, to calculate the radiative forcing we choose the coarser resolution data that covers the larger domain. Figure 5.14 shows

the schematic diagrams of the quantitative comparison of the radiative flux components (averaged over the larger domain; d01) considering both dust direct and indirect effects.

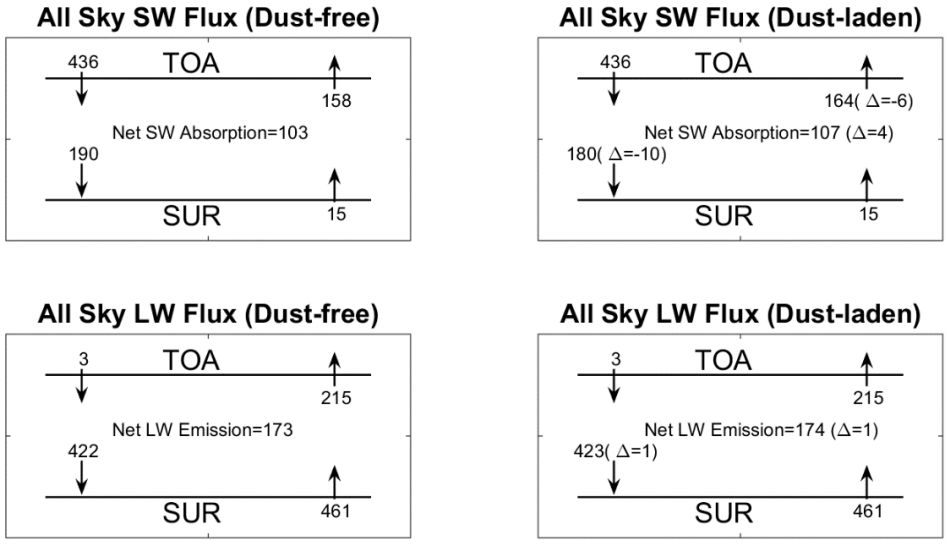

Figure 5.14 Schematic diagram of the time and domain averaged (0Z July 01 to 18Z July 31, 2010; 0-25°N, 20-50°W) radiative flux components (W/m^2) for direct + indirect effects in all sky condition. All the data correspond to the experiment I36.

When the dust indirect effects are included with the direct effect simulation, both cloud enhancement (inside and above the dust layer) and reduction (below the dust layer) are found. Hence, the cloud feedback to the radiative forcing in this case is very mild. Consequently, the pure radiative forcing of dust at the TOA and SUR are changed only slightly, while the radiative forcing inside the atmosphere remains the same (figure 5.14). Table 5.2 summarizes the magnitudes of the radiative forcing in different cases.

Table 5.2 Spatially and temporally averaged radiative forcing (W/m^2) of the Atmosphere, Surface, and top of the atmosphere with (All sky) and without the cloud feedback (Clear sky), considering both dust direct and indirect effects. Radiative forcing are calculated from the radiative fluxes averaged over 2.5-12°N, 30-40°W; 0Z July 06 -18Z July 13 for the finer resolution runs (I04), and over 0-25°N, 20-50°W; 0Z July 01 - 18Z July 31 for the coarser resolution runs (I36).

Radiative forcing	Clear Sky (I04)	All Sky (I04)	Clear Sky (I36)	All Sky (I36)
Atmosphere (RF_{ATM})	+3	+2	+2	+3
Surface (RF_{SUR})	-13	-13	-11	-9
Top of the Atmosphere (RF_{TOA})	-10	-8	-9	-6

Chapter 6: Conclusion

6.1 Summary

In this study, we have explored the direct and indirect effects of the Saharan dust aerosols on various weather and climate parameters. Both remote sensing and numerical simulation data are used to study the sensitivity of these parameters to the dust loading over the tropical east Atlantic Ocean. Observational data from various satellite measurements are used to analyze the dust climatology and its correlations with the tropospheric temperature and humidity anomalies spanning the period 2003-2012. Using AOD as a proxy to the dust loading, the climatology study based on the monthly mean data over the 10 year period shows that highest dust loading occur in July (AOD ~ 0.34) and lowest in November (AOD ~ 0.18). Interannual variations of the AOD in July during the study period indicates that the years 2003, 2007, and 2010 had high dust loadings with 10%, 8%, and 7% positive AOD anomalies respectively. High coarse mode to fine mode AOD ratio, and lower values of the Angstrom Exponent (AE) suggest that the tropical east Atlantic Ocean is mainly dominated by the dust aerosols. We also found that the dust-laden SAL is indeed associated with the warm and dry air anomalies. The eastern part of the domain where dust loading is highest, show the maximum warm anomaly (strongest ΔT ~ +0.7 K; at ~ 1.4 km) with respect to the domain mean. Likewise, the humidity profiles also show dry anomaly in the high dust region (strongest Δq ~ -0.9 g/kg; at ~ 0.8 km). To identify the potential role of the Saharan dust in generating and maintaining the warm and dry anomalies, coupled variations of these anomalies with the dust loading anomalies are examined using two statistical techniques: EOF and SVD. Results from these analyses show that the temperature variabilities over the tropical east Atlantic Ocean have no

statistically significant correlation with the variabilities of the dust transport. On the other hand, the variabilities of the dust loading have negative effect on the moisture field (correlation coefficient ~ -0.5) in the downstream of the SAL's trajectory. However, considering the entire domain these warm and dry anomalies do not show any significant coupled variations with the AOD anomalies throughout the study period (2003-2012). This indicates that either the Saharan dust has trivial contributions to these anomalies, or over longer timescale dust effects are overwhelmed by other potential contributing factors.

Numerical simulation experiments are carried out for one of the high dust loading month: July 2010, using the WRF-Chem model over two-way nested domains in the tropical east Atlantic Ocean. Prior to the analyses of the simulation data, model outputs are validated against satellite measurements and analyses data from several platforms. Compared to the AIRS measurements, model shows cold (up to ~ - 0.6 K at ~ 1.5 km) and wet bias [up to ~ 1.6 g/kg (14%) at ~ 1.5 km] in the lower troposphere. However, model temperature and moisture data are in very good agreement with the NCEP final analyses data. In the direct effect-only simulation (D36), the cloud LWP is overestimated with respect to the MODIS Aqua and Terra measurements, while the inclusion of indirect effects (I36) produce more realistic cloud LWP. This suggests that both direct and the indirect aerosol effects need to be considered together to represent the reasonable cloud amount. Precipitation amount is significantly overestimated in all runs, indicating the need of model tuning to better forecast the precipitation. In addition, the vertical extinction profile of dust (as a proxy to the dust mass loading) also shows some disagreements with the CALIPSO measurement. However, it should be noted that the model outputs used for the analysis are based on one month forecast, and therefore the discrepancies of the simulation data with the observation data are not unexpected.

Absorption and scattering properties of the Saharan dust at different shortwave (SW) and longwave (LW) spectral bands are explored, both including and excluding the moisture effects. Analyses of the model outputs of absorption and scattering efficiencies with and without dust show that the net contribution of dust to the total absorption and scattering of SW is significantly higher compared to the other aerosols. This suggests that the dust is the primary aerosol species contributing to the SW radiation budget in our domain. As expected, dust scattering efficiency dominates the absorption efficiency in the SW bands. Compared to the scattering efficiency, the absorption efficiency is more sensitive to the wavelengths of the spectral band. The absorption efficiency is strongest in the lower end of the spectral region (300 nm) and become weaker with increasing wavelengths which follows the findings from the field experiment on Saharan dust optical properties [*Petzold et al.*, 2009]. As the refractive indices of dust were held fixed in the model codes (for all wavelengths), this sensitivity of the absorption and scattering to different spectral bands can be attributed to the size distribution of dust and/or the variable moisture content of the dust. In the moisture free conditions, the geographical distributions of the absorption and scattering AODs in both shortwave and longwave follow the dust distribution pattern, i.e. higher in the eastern part of the domain where dust loading is higher, and become lower as one goes westward. However, in the presence of moisture fields, the SW scattering AOD peak is shifted westward, indicating the importance of the water vapor in the modulation of dust scattering property. In general, compared to the SW absorption AODs, the LW absorption AODs are small with the exception of the AOD at 1030 cm^{-1}, which is due to the quartz contained dust. This absorption peak falls within the infrared atmospheric window (8-12 μm) and plays a crucial role in regulating the longwave radiation budget [*Osborne et al.*, 2011].

Interactions of dust particles with the SW and LW radiations reduce the upwelling SW fluxes at the TOA, and downwelling SW fluxes at the SUR, and increase the downwelling LW fluxes at the SUR. Perturbations of these fluxes lead to net positive radiative forcing inside the ATM, and negative forcing at the, SUR, and TOA, which are discussed later in this section. Due to the shortwave absorption and longwave emission inside the dust layer, dust induced perturbations of the atmospheric heating rates are positive (warming) for SW, and negative (cooling) for the LW. In addition, similar to the greenhouse gases, dust layers absorb the longwave radiation emitted from the surface and then remit back towards the surface causing longwave warming in the lower levels. Therefore, the dust induced warming peak does not occur inside the maximum dust layer, but below it. Consequently, the mean temperature perturbation is maximum in the lower levels (~ +0.3 K; below ~ 1 km) over the eastern part of the domain. Although the approaches in the analysis of the observational and model data are slightly different we see that the model underestimates the dust warming compared to the AIRS (ΔT ~ +0.7 K; at ~ 1.4 km). We attribute this discrepancy to the coarser vertical resolution of the AIRS data and also to the inaccurate vertical representation of the dust profiles supplied by the MOZART model. In addition, the moisture field in the model data do not show any sensitivity to the dust which clearly conflicts the dry anomalies identified from the observation data. We attribute this to the constant SST in the model simulations. Nevertheless, dust induced warming increases the conditional instability in lower levels that inhibits convection and reduces the cloud cover in lower levels. The cloud reduction is strongest (maximum ~ 9%) in the eastern part of the domain (20°W-30°W) where the dust loading is highest, confirming that the dust heating is mainly responsible for the convection inhibition. Unlike the other studies, we found that the surface heat fluxes show very little

sensitivity to the surface dimming which can be attributed to the constant SST during the simulations.

We have also explored the dust effects on cloud microphysical properties. Despite the low hygroscopicity of dust, sensitivity tests show that both cloud water mass and number concentration are most sensitive to the presence of dust aerosols. This can be attributed to dust particle aging through the deposition of water soluble materials on dust particles' surface as they travel across the Atlantic Ocean. Therefore, we found that dust is not only the major aerosol influencing the radiation but also the primary CCN in our domain. Presence of dust as a CCN increases the cloud droplet number concentrations with reduced droplet sizes, which is consistent with the first indirect effect. The overall cloud LWP is increased by 7.3% while we see a shift of the LWP distribution from thinner cloud (LWP ~ 0.05 mm) to relatively thicker cloud (LWP > 0.07 mm) in the presence dust. The mean droplet radius over the smaller domain is reduced from 12.4 μm to 10.7 μm (14% reduction). While the droplet size becomes smaller, collision coalescence process among the droplets becomes slower, which reduces the cloud droplet autoconversion rate, i.e. the rain production rate. As a result, both the rainwater mass and number concentration are decreased. However, this does not suppress the accumulated precipitation amount at the surface because of the reduced rain evaporation in the presence of dust. Therefore, there is no indication of dust influence on the cloud lifetime (aerosol second indirect effect) found by other studies on different aerosol types. Similar to the accumulated precipitation on the surface, other moisture budget components including the moisture evaporation from the surface, zonal, and meridional moisture fluxes also show very little sensitivity to the dust concentration.

Dust induced changes to the atmospheric heating reduces the instability at ~ 1 km that affects the buoyancy and modulates the convection. We find that the simulation with dust has weaker buoyancy values in lower levels and stronger values in upper levels. These changes of buoyancy inhibit the convection below the dust layers and strengthen it inside and above the dust layer. While dust is considered as a CCN, more CCN are available for the moisture condensation. As a result, when both direct and indirect effects of dust are considered together, the cloud cover is not only reduced in the lower levels but also enhanced in the upper levels. It should be noted that in the direct effect-only case, the cloud enhancement in the upper levels was negligible.

We found that the climate forcing of dust over the tropical Atlantic Ocean not only depends on the type of the dust effects we consider but also depends on the radiative feedback from the modified cloud field. Perturbations of the radiation budget by dust can be estimated in three different cases: 1) pure direct radiative forcing in cloud free condition, 2) direct radiative forcing with the feedback from the modified cloud field, and 3) both direct and indirect radiative forcing together with cloud feedback. Results show that the net radiative forcing of Saharan dust averaged over the larger domain (d01), and the one month period (July 2010) is positive inside the ATM, and negative at the SUR, and TOA. The radiative forcing of dust inside the atmosphere is same (+3 W/m^2) in all three cases. In cloud free condition, the radiative forcing of the dust are -14, and -11 W/m^2 at the SUR and TOA respectively (case 1). The direct effect of dust leads to the reduction of the cloud cover below the dust layer, giving positive radiative forcing feedback from the cloud. In addition, the vertical position of the cloud layer with respect to the dust layer strengthens the positive cloud radiative forcing feedback. This significantly compensates the dust negative radiative forcing at the SUR and

TOA, which are reduced to -5, and -3 W/m^2 respectively (case 2). When the dust indirect effects are included with the direct effect, both cloud enhancement (inside and above the dust layer) and reduction (below the dust layer) are found. Hence, the cloud feedback to the pure radiative forcing in this case is relatively weaker. Consequently, the net negative radiative forcing of dust become -9, and -6 W/m^2 at the SUR and TOA respectively (case 3).

It is evident that dust induced perturbations of most of the model outputs are small in magnitude (e.g., ~ +0.3 K warming; below the peak dust layer). Nevertheless, we suggest that these perturbations are indeed due to the dust induced changes of physical processes of the atmosphere rather than the model uncertainty. This is because some of our findings are consistent with different parameterization schemes (e.g., reduction of lower level cloud using Lin microphysics scheme instead of the Morrison scheme), and also agree well with the literature [e.g., RF at TOA and SUR are consistent with *Zhu et al.*, 2007].

6.2 Future Work

Our future work following the completion of this dissertation include the refinement of the model configurations to better forecast the simulation outputs, as well as taking different approaches to identify the dust effects. In this study, mostly spatial and temporal average of the model output data are analyzed to explore the dust effects. In future, we plan to analyze the model outputs by focusing on specific grid cells with unique characteristics such as the enhanced convective activities, anomalous latent heating etc. In addition, we will further examine the moisture effects on dust scattering, identify the possible mechanisms of the production of thicker clouds, and enhanced rain evaporation in the presence of dust.

Bibliography

Ackerman, A. S., M. P. Kirkpatrick, D. E. Stevens, and O. B. Toon (2004), The impact of humidity above stratiform clouds on indirect aerosol climate forcing, *Nature*, *432*(7020), 1014–1017, doi:10.1038/nature03174.

Ackermann, I. J., H. Hass, M. Memmesheimer, A. Ebel, F. S. Binkowski, and U. Shankar (1998), Modal Aerosol Dynamics model for Europe: Development and first applications, *Atmos. Environ.*, *32*(17), 2981–2999, doi:10.1016/S1352-2310(98)00006-5.

Albrecht, B. A. (1989), Aerosols, Cloud Microphysics, and Fractional Cloudiness, *Science*, *245*(4923), 1227–1230, doi:10.1126/science.245.4923.1227.

Altaratz, O., I. Koren, T. Reisin, A. Kostinski, G. Feingold, Z. Levin, and Y. Yin (2008), Aerosols' influence on the interplay between condensation, evaporation and rain in warm cumulus cloud, *Atmos Chem Phys*, *8*(1), 15–24, doi:10.5194/acp-8-15-2008.

Ångström, A. (1964), The parameters of atmospheric turbidity, *Tellus*, *16*(1), 64–75, doi:10.1111/j.2153-3490.1964.tb00144.x.

Barnard, J. C., J. D. Fast, G. Paredes-Miranda, W. P. Arnott, and A. Laskin (2010), Technical Note: Evaluation of the WRF-Chem "Aerosol Chemical to Aerosol Optical Properties" Module using data from the MILAGRO campaign, *Atmos Chem Phys*, *10*(15), 7325–7340, doi:10.5194/acp-10-7325-2010.

Berg, W., T. L'Ecuyer, and S. van den Heever (2008), Evidence for the impact of aerosols on the onset and microphysical properties of rainfall from a combination of satellite observations and cloud-resolving model simulations, *J. Geophys. Res. Atmospheres*, *113*(D14), D14S23, doi:10.1029/2007JD009649.

Binkowski, F. S., and U. Shankar (1995), The Regional Particulate Matter Model: 1. Model description and preliminary results, *J. Geophys. Res. Atmospheres*, *100*(D12), 26191–26209, doi:10.1029/95JD02093.

Bjornsson, H., and S. A. Venegas (1997), *A Manual for EOF and SVD Analyses of Climatic Data, CCGCR Rep. 97-1, 52 pp., Cent. for Clim. and Global Change Res., McGill Univ., Montreal, Que., Canada*.

Boucher, O. et al. (1998), Intercomparison of models representing direct shortwave radiative forcing by sulfate aerosols, *J. Geophys. Res. Atmospheres*, *103*(D14), 16979–16998, doi:10.1029/98JD00997.

Braun, S. A. (2010), Reevaluating the Role of the Saharan Air Layer in Atlantic Tropical Cyclogenesis and Evolution, *Mon. Weather Rev.*, *138*(6), 2007–2037, doi:10.1175/2009MWR3135.1.

Bréon, F.-M., and S. Colzy (2000), Global distribution of cloud droplet effective radius from POLDER polarization measurements, *Geophys. Res. Lett.*, *27*(24), 4065–4068, doi:10.1029/2000GL011691.

Bretherton, C. S., C. Smith, and J. M. Wallace (1992), An Intercomparison of Methods for Finding Coupled Patterns in Climate Data, *J. Clim.*, *5*(6), 541–560, doi:10.1175/1520-0442(1992)005<0541:AIOMFF>2.0.CO;2.

Brown, P. J., and C. D. Kummerow (2013), An Assessment of Atmospheric Water Budget Components over Tropical Oceans, *J. Clim.*, *27*(5), 2054–2071, doi:10.1175/JCLI-D-13-00385.1.

Buseck, P. R., and M. Pósfai (1999), Airborne minerals and related aerosol particles: Effects on climate and the environment, *Proc. Natl. Acad. Sci.*, *96*(7), 3372–3379, doi:10.1073/pnas.96.7.3372.

Cai, Q., T. Zhou, and Z. Guo (2016), Impacts of shallow convection on the simulation of the tropical precipitation diurnal cycle, *Int. J. Climatol.*, *36*(15), 4885–4902, doi:10.1002/joc.4676.

Chen, F., and J. Dudhia (2001), Coupling an Advanced Land Surface–Hydrology Model with the Penn State–NCAR MM5 Modeling System. Part I: Model Implementation and Sensitivity, *Mon. Weather Rev.*, *129*(4), 569–585, doi:10.1175/1520-0493(2001)129<0569:CAALSH>2.0.CO;2.

Choobari, O. A., P. Zawar-Reza, and A. Sturman (2014), The global distribution of mineral dust and its impacts on the climate system: A review, *Atmospheric Res.*, *138*, 152–165, doi:10.1016/j.atmosres.2013.11.007.

Christopher, S. A., and T. Jones (2007), Satellite-based assessment of cloud-free net radiative effect of dust aerosols over the Atlantic Ocean, *Geophys. Res. Lett.*, *34*(2), L02810, doi:10.1029/2006GL027783.

Denjean, C., S. Caquineau, K. Desboeufs, B. Laurent, M. Quiñones Rosado, P. Vallejo, O. Mayol-Bracero, and P. Formenti (2015), Does the long-range transport of African mineral dust across the Atlantic enhance their hygroscopicity?, vol. 17, p. 7790.

Dubovik, O., B. Holben, T. F. Eck, A. Smirnov, Y. J. Kaufman, M. D. King, D. Tanré, and I. Slutsker (2002), Variability of Absorption and Optical Properties of Key Aerosol Types Observed in Worldwide Locations, *J. Atmospheric Sci.*, *59*(3), 590–608, doi:10.1175/1520-0469(2002)059<0590:VOAAOP>2.0.CO;2.

Dunion, J. P., and C. S. Velden (2004), The Impact of the Saharan Air Layer on Atlantic Tropical Cyclone Activity, *Bull. Am. Meteorol. Soc.*, *85*(3), 353–365, doi:10.1175/BAMS-85-3-353.

Easter, R. C., S. J. Ghan, Y. Zhang, R. D. Saylor, E. G. Chapman, N. S. Laulainen, H. Abdul-Razzak, L. R. Leung, X. Bian, and R. A. Zaveri (2004), MIRAGE: Model

description and evaluation of aerosols and trace gases, *J. Geophys. Res. Atmospheres*, *109*(D20), D20210, doi:10.1029/2004JD004571.

Eck, T. F., B. N. Holben, J. S. Reid, O. Dubovik, A. Smirnov, N. T. O'Neill, I. Slutsker, and S. Kinne (1999), Wavelength dependence of the optical depth of biomass burning, urban, and desert dust aerosols, *J. Geophys. Res.*, *104*, 31, doi:10.1029/1999JD900923.

Evan, A. T., J. Dunion, J. A. Foley, A. K. Heidinger, and C. S. Velden (2006), New evidence for a relationship between Atlantic tropical cyclone activity and African dust outbreaks, *Geophys. Res. Lett.*, *33*(19), L19813, doi:10.1029/2006GL026408.

Evan, A. T., A. K. Heidinger, R. Bennartz, V. Bennington, N. M. Mahowald, H. Corrada-Bravo, C. S. Velden, G. Myhre, and J. P. Kossin (2008), Ocean temperature forcing by aerosols across the Atlantic tropical cyclone development region, *Geochem. Geophys. Geosystems*, *9*(5), Q05V04, doi:10.1029/2007GC001774.

Fan, J., R. Zhang, W.-K. Tao, and K. I. Mohr (2008), Effects of aerosol optical properties on deep convective clouds and radiative forcing, *J. Geophys. Res. Atmospheres*, *113*(D8), D08209, doi:10.1029/2007JD009257.

Fast, J. D., W. I. Gustafson, R. C. Easter, R. A. Zaveri, J. C. Barnard, E. G. Chapman, G. A. Grell, and S. E. Peckham (2006), Evolution of ozone, particulates, and aerosol direct radiative forcing in the vicinity of Houston using a fully coupled meteorology-chemistry-aerosol model, *J. Geophys. Res. Atmospheres*, *111*(D21), D21305, doi:10.1029/2005JD006721.

Foltz, G. R., and M. J. McPhaden (2008), Impact of Saharan Dust on Tropical North Atlantic SST, *J. Clim.*, *21*(19), 5048–5060, doi:10.1175/2008JCLI2232.1.

Formenti, P., L. Schütz, Y. Balkanski, K. Desboeufs, M. Ebert, K. Kandler, A. Petzold, D. Scheuvens, S. Weinbruch, and D. Zhang (2011), Recent progress in understanding physical and chemical properties of African and Asian mineral dust, *Atmos Chem Phys*, *11*(16), 8231–8256, doi:10.5194/acp-11-8231-2011.

Forster, P. et al. (2007), Changes in Atmospheric Constituents and in Radiative Forcing. Chapter 2,

Fu, Q., P. Yang, and W. B. Sun (1998), An Accurate Parameterization of the Infrared Radiative Properties of Cirrus Clouds for Climate Models, *J. Clim.*, *11*(9), 2223–2237, doi:10.1175/1520-0442(1998)011<2223:AAPOTI>2.0.CO;2.

García, M. I., B. L. van Drooge, S. Rodríguez, and A. Alastuey (2017), Speciation of organic aerosols in the Saharan Air Layer and in the free troposphere westerlies, *Atmos Chem Phys Discuss*, *2017*, 1–33, doi:10.5194/acp-2017-108.

Givati, A., and D. Rosenfeld (2004), Quantifying Precipitation Suppression Due to Air Pollution, *J. Appl. Meteorol.*, *43*(7), 1038–1056, doi:10.1175/1520-0450(2004)043<1038:QPSDTA>2.0.CO;2.

Grell, G. A., and D. Dévényi (2002), A generalized approach to parameterizing convection combining ensemble and data assimilation techniques, *Geophys. Res. Lett.*, *29*(14), 38–1, doi:10.1029/2002GL015311.

Grell, G. A., S. E. Peckham, R. Schmitz, S. A. McKeen, G. Frost, W. C. Skamarock, and B. Eder (2005), Fully coupled "online" chemistry within the WRF model, *Atmos. Environ.*, *39*, 6957–6975, doi:10.1016/j.atmosenv.2005.04.027.

Grogan, D. F. P., T. R. Nathan, and S.-H. Chen (2015), Effects of Saharan Dust on the Linear Dynamics of African Easterly Waves, *J. Atmospheric Sci.*, *73*(2), 891–911, doi:10.1175/JAS-D-15-0143.1.

Grogan, D. F. P., T. R. Nathan, and S.-H. Chen (2016), Saharan Dust and the Nonlinear Evolution of the African Easterly Jet–African Easterly Wave System, *J. Atmospheric Sci.*, *74*(1), 27–47, doi:10.1175/JAS-D-16-0118.1.

Han, Q., W. B. Rossow, J. Zeng, and R. Welch (2002), Three Different Behaviors of Liquid Water Path of Water Clouds in Aerosol-Cloud Interactions., *J. Atmospheric Sci.*, *59*, 726–735, doi:10.1175/1520-0469(2002)059<0726:TDBOLW>2.0.CO;2.

Haywood, J. M., R. P. Allan, I. Culverwell, T. Slingo, S. Milton, J. Edwards, and N. Clerbaux (2005), Can desert dust explain the outgoing longwave radiation anomaly over the Sahara during July 2003?, *J. Geophys. Res. Atmospheres*, *110*(D5), D05105, doi:10.1029/2004JD005232.

Highwood, E. J., J. M. Haywood, M. D. Silverstone, S. M. Newman, and J. P. Taylor (2003), Radiative properties and direct effect of Saharan dust measured by the C-130 aircraft during Saharan Dust Experiment (SHADE): 2. Terrestrial spectrum, *J. Geophys. Res. Atmospheres*, *108*(D18), 8578, doi:10.1029/2002JD002552.

Hsieh, W. C., H. Jonsson, L.-P. Wang, G. Buzorius, R. C. Flagan, J. H. Seinfeld, and A. Nenes (2009), On the representation of droplet coalescence and autoconversion: Evaluation using ambient cloud droplet size distributions, *J. Geophys. Res. Atmospheres*, *114*(D7), D07201, doi:10.1029/2008JD010502.

Hu, Y. X., and K. Stamnes (1993), An Accurate Parameterization of the Radiative Properties of Water Clouds Suitable for Use in Climate Models, *J. Clim.*, *6*(4), 728–742, doi:10.1175/1520-0442(1993)006<0728:AAPOTR>2.0.CO;2.

Huang, J., C. Zhang, and J. M. Prospero (2010), African dust outbreaks: A satellite perspective of temporal and spatial variability over the tropical Atlantic Ocean, *J. Geophys. Res. Atmospheres*, *115*(D5), D05202, doi:10.1029/2009JD012516.

Huneeus, N. et al. (2011), Global dust model intercomparison in AeroCom phase I, *Atmos Chem Phys*, *11*(15), 7781–7816, doi:10.5194/acp-11-7781-2011.

Iacono, M. J., J. S. Delamere, E. J. Mlawer, M. W. Shephard, S. A. Clough, and W. D. Collins (2008), Radiative forcing by long-lived greenhouse gases: Calculations with the AER radiative transfer models, *J. Geophys. Res. Atmospheres*, *113*(D13), D13103, doi:10.1029/2008JD009944.

Jones, C., N. Mahowald, and C. Luo (2004), Observational evidence of African desert dust intensification of easterly waves, *Geophys. Res. Lett.*, *31*(17), L17208, doi:10.1029/2004GL020107.

Jury, M. R., and M. J. Santiago (2010), Composite analysis of dust impacts on African easterly waves in the Moderate Resolution Imaging Spectrometer era, *J. Geophys. Res. Atmospheres*, *115*(D16), D16213, doi:10.1029/2009JD013612.

Kaufeld, W. J., and S. W. Nesbitt (n.d.), *Jp2.5 Toward Assessing the Effect of Aerosols on Deep Convection: A Numerical Study Using the Wrf-Chemistry Model*.

Kaufman, Y. J., I. Koren, L. A. Remer, D. Rosenfeld, and Y. Rudich (2005), The effect of smoke, dust, and pollution aerosol on shallow cloud development over the Atlantic Ocean, *Proc. Natl. Acad. Sci. U. S. A.*, *102*(32), 11207–11212, doi:10.1073/pnas.0505191102.

Lau, K. M., and K. M. Kim (2007), Cooling of the Atlantic by Saharan dust, *Geophys. Res. Lett.*, *34*(23), L23811, doi:10.1029/2007GL031538.

Lee, H., and S. S. Yum (2012), Aerosol-induced enhancement of precipitation in mixed phase convective clouds: a modeling study, *AGU Fall Meet. Abstr.*, *23*.

Lee, S. S., J. E. Penner, and S. M. Saleeby (2009), Aerosol effects on liquid-water path of thin stratocumulus clouds, *J. Geophys. Res. Atmospheres*, *114*(D7), D07204, doi:10.1029/2008JD010513.

Li, F., A. M. Vogelmann, and V. Ramanathan (2004), Saharan Dust Aerosol Radiative Forcing Measured from Space, *J. Clim.*, *17*(13), 2558–2571, doi:10.1175/1520-0442(2004)017<2558:SDARFM>2.0.CO;2.

Liao, H., and J. H. Seinfeld (1998), Radiative forcing by mineral dust aerosols: Sensitivity to key variables, *J. Geophys. Res. Atmospheres*, *103*(D24), 31637–31645, doi:10.1029/1998JD200036.

Lin, Y.-L., R. D. Farley, and H. D. Orville (1983), Bulk Parameterization of the Snow Field in a Cloud Model, *J. Clim. Appl. Meteorol.*, *22*(6), 1065–1092, doi:10.1175/1520-0450(1983)022<1065:BPOTSF>2.0.CO;2.

Mahowald, N., S. Albani, J. F. Kok, S. Engelstaeder, R. Scanza, D. S. Ward, and M. G. Flanner (2014), The size distribution of desert dust aerosols and its impact on the Earth system, *Aeolian Res.*, *15*, 53–71, doi:10.1016/j.aeolia.2013.09.002.

Mallet, M., P. Tulet, D. Serça, F. Solmon, O. Dubovik, J. Pelon, V. Pont, and O. Thouron (2009), Impact of dust aerosols on the radiative budget, surface heat fluxes, heating rate profiles and convective activity over West Africa during March 2006, *Atmos Chem Phys*, *9*(18), 7143–7160, doi:10.5194/acp-9-7143-2009.

Martin, G. M., D. W. Johnson, and A. Spice (1994), The Measurement and Parameterization of Effective Radius of Droplets in Warm Stratocumulus Clouds, *J. Atmospheric Sci.*, *51*(13), 1823–1842, doi:10.1175/1520-0469(1994)051<1823:TMAPOE>2.0.CO;2.

Miller, R. L., I. Tegen, and J. Perlwitz (2004), Surface radiative forcing by soil dust aerosols and the hydrologic cycle, *J. Geophys. Res. Atmospheres*, *109*(D4), D04203, doi:10.1029/2003JD004085.

Morrison, H., J. A. Curry, and V. I. Khvorostyanov (2005), A New Double-Moment Microphysics Parameterization for Application in Cloud and Climate Models. Part I: Description, *J. Atmospheric Sci.*, *62*(6), 1665–1677, doi:10.1175/JAS3446.1.

Morrison, H., G. Thompson, and V. Tatarskii (2009), Impact of Cloud Microphysics on the Development of Trailing Stratiform Precipitation in a Simulated Squall Line: Comparison of One- and Two-Moment Schemes, *Mon. Weather Rev.*, *137*(3), 991–1007, doi:10.1175/2008MWR2556.1.

Naeger, A. R., S. A. Christopher, and B. T. Johnson (2013), Multiplatform analysis of the radiative effects and heating rates for an intense dust storm on 21 June 2007, *J. Geophys. Res. Atmospheres*, *118*(16), 9316–9329, doi:10.1002/jgrd.50713.

Nakanishi, M., and H. Niino (2006), An Improved Mellor–Yamada Level-3 Model: Its Numerical Stability and Application to a Regional Prediction of Advection Fog, *Bound.-Layer Meteorol.*, *119*(2), 397–407, doi:10.1007/s10546-005-9030-8.

Nousiainen, T. (2009), Optical modeling of mineral dust particles: A review, *J. Quant. Spectrosc. Radiat. Transf.*, *110*(14–16), 1261–1279, doi:10.1016/j.jqsrt.2009.03.002.

Osborne, S. R., A. J. Baran, B. T. Johnson, J. M. Haywood, E. Hesse, and S. Newman (2011), Short-wave and long-wave radiative properties of Saharan dust aerosol, *Q. J. R. Meteorol. Soc.*, *137*(658), 1149–1167, doi:10.1002/qj.771.

Otto, S., M. de Reus, T. Trautmann, A. Thomas, M. Wendisch, and S. Borrmann (2007), Atmospheric radiative effects of an in situ measured Saharan dust plume and the role of large particles, *Atmos Chem Phys*, *7*(18), 4887–4903, doi:10.5194/acp-7-4887-2007.

Ou, S. C., K. N. Liou, N. C. Hsu, and S. C. Tsay (2012), Satellite remote sensing of dust aerosol indirect effects on cloud formation over Eastern Asia, *Int. J. Remote Sens.*, *33*(22), 7257–7272, doi:10.1080/01431161.2012.700135.

Perrone, M. R., A. M. Tafuro, and S. Kinne (2012), Dust layer effects on the atmospheric radiative budget and heating rate profiles, *Atmos. Environ.*, *59*, 344–354, doi:10.1016/j.atmosenv.2012.06.012.

Petzold, A. et al. (2009), Saharan dust absorption and refractive index from aircraft-based observations during SAMUM 2006, *Tellus B*, *61*(1), 118–130, doi:10.1111/j.1600-0889.2008.00383.x.

Prospero, J. M., and T. N. Carlson (1972), Vertical and areal distribution of Saharan dust over the western equatorial north Atlantic Ocean, *J. Geophys. Res.*, *77*(27), 5255–5265, doi:10.1029/JC077i027p05255.

Ramanathan, V., P. J. Crutzen, J. T. Kiehl, and D. Rosenfeld (2001), Aerosols, Climate, and the Hydrological Cycle, *Science*, *294*(5549), 2119–2124, doi:10.1126/science.1064034.

Rodríguez, S., A. Alastuey, S. Alonso-Pérez, X. Querol, E. Cuevas, J. Abreu-Afonso, M. Viana, N. Pérez, M. Pandolfi, and J. de la Rosa (2011), Transport of desert dust mixed with North African industrial pollutants in the subtropical Saharan Air Layer, *Atmos Chem Phys*, *11*(13), 6663–6685, doi:10.5194/acp-11-6663-2011.

Rosenfeld, D., Y. Rudich, and R. Lahav (2001), Desert dust suppressing precipitation: A possible desertification feedback loop, *Proc. Natl. Acad. Sci. U. S. A.*, *98*(11), 5975–5980, doi:10.1073/pnas.101122798.

Rosenfeld, D. et al. (2014), Global observations of aerosol-cloud-precipitation-climate interactions, *Rev. Geophys.*, *52*(4), 2013RG000441, doi:10.1002/2013RG000441.

Saleeby, S. M., S. R. Herbener, S. C. van den Heever, and T. L'Ecuyer (2015), Impacts of Cloud Droplet–Nucleating Aerosols on Shallow Tropical Convection, *J. Atmospheric Sci.*, *72*(4), 1369–1385, doi:10.1175/JAS-D-14-0153.1.

Schell, B., I. J. Ackermann, H. Hass, F. S. Binkowski, and A. Ebel (2001), Modeling the formation of secondary organic aerosol within a comprehensive air quality model system, *J. Geophys. Res. Atmospheres*, *106*(D22), 28275–28293, doi:10.1029/2001JD000384.

Schuster, G. L., O. Dubovik, and B. N. Holben (2006), Angstrom exponent and bimodal aerosol size distributions, *J. Geophys. Res. Atmospheres*, *111*(D7), D07207, doi:10.1029/2005JD006328.

Shell, K. M., and R. C. J. Somerville (2007), Direct radiative effect of mineral dust and volcanic aerosols in a simple aerosol climate model, *J. Geophys. Res. Atmospheres*, *112*(D3), D03205, doi:10.1029/2006JD007197.

Skamarock, W., J. Klemp, J. Dudhia, D. Gill, M. Barker, K. Duda, -Y Huang, W. Wang, and J. Powers (2008), *A description of the Advanced Research WRF Version 3*.

Smith, R. K. (2013), *The Physics and Parameterization of Moist Atmospheric Convection*, Springer Science & Business Media.

Sokolik, I. N., D. M. Winker, G. Bergametti, D. A. Gillette, G. Carmichael, Y. J. Kaufman, L. Gomes, L. Schuetz, and J. E. Penner (2001), Introduction to special section: Outstanding problems in quantifying the radiative impacts of mineral dust, *J. Geophys. Res. Atmospheres*, *106*(D16), 18015–18027, doi:10.1029/2000JD900498.

Solomos, S., G. Kallos, J. Kushta, M. Astitha, C. Tremback, A. Nenes, and Z. Levin (2011), An integrated modeling study on the effects of mineral dust and sea salt particles on clouds and precipitation, *Atmos Chem Phys*, *11*(2), 873–892, doi:10.5194/acp-11-873-2011.

Stephens, G. L., N. B. Wood, and L. A. Pakula (2004), On the radiative effects of dust on tropical convection, *Geophys. Res. Lett.*, *31*(23), L23112, doi:10.1029/2004GL021342.

Stevens, B., W. R. Cotton, G. Feingold, and C.-H. Moeng (1998), Large-Eddy Simulations of Strongly Precipitating, Shallow, Stratocumulus-Topped Boundary Layers, *J. Atmospheric Sci.*, *55*(24), 3616–3638, doi:10.1175/1520-0469(1998)055<3616:LESOSP>2.0.CO;2.

Stockwell, W. R., P. Middleton, J. S. Chang, and X. Tang (1990), The second generation regional acid deposition model chemical mechanism for regional air quality modeling, *J. Geophys. Res. Atmospheres*, *95*(D10), 16343–16367, doi:10.1029/JD095iD10p16343.

Sun, D., W. K. M. Lau, M. Kafatos, Z. Boybeyi, G. Leptoukh, C. Yang, and R. Yang (2009), Numerical Simulations of the Impacts of the Saharan Air Layer on Atlantic Tropical Cyclone Development, *J. Clim.*, *22*(23), 6230–6250, doi:10.1175/2009JCLI2738.1.

Talbot, R. W., R. C. Harriss, E. V. Browell, G. L. Gregory, D. I. Sebacher, and S. M. Beck (1986), Distribution and geochemistry of aerosols in the tropical north Atlantic troposphere: Relationship to Saharan dust, *J. Geophys. Res. Atmospheres*, *91*(D4), 5173–5182, doi:10.1029/JD091iD04p05173.

Tang, M. J., J. Whitehead, N. M. Davidson, F. D. Pope, M. R. Alfarra, G. McFiggans, and M. Kalberer (2015), Cloud condensation nucleation activities of calcium carbonate and its atmospheric ageing products, *Phys. Chem. Chem. Phys. PCCP*, *17*(48), 32194–32203, doi:10.1039/c5cp03795f.

Tao, W.-K., J.-P. Chen, Z. Li, C. Wang, and C. Zhang (2012), Impact of aerosols on convective clouds and precipitation, *Rev. Geophys.*, *50*(2), RG2001, doi:10.1029/2011RG000369.

Tegen, I., P. Hollrig, M. Chin, I. Fung, D. Jacob, and J. Penner (1997), Contribution of different aerosol species to the global aerosol extinction optical thickness: Estimates from model results, *J. Geophys. Res. Atmospheres*, *102*(D20), 23895–23915, doi:10.1029/97JD01864.

Teller, A., L. Xue, and Z. Levin (2012), The effects of mineral dust particles, aerosol regeneration and ice nucleation parameterizations on clouds and precipitation, *Atmos Chem Phys*, *12*(19), 9303–9320, doi:10.5194/acp-12-9303-2012.

Textor, C. et al. (2006), Analysis and quantification of the diversities of aerosol life cycles within AeroCom, *Atmos Chem Phys*, *6*(7), 1777–1813, doi:10.5194/acp-6-1777-2006.

Twomey, S. (1977), The Influence of Pollution on the Shortwave Albedo of Clouds, *J. Atmospheric Sci.*, *34*(7), 1149–1152, doi:10.1175/1520-0469(1977)034<1149:TIOPOT>2.0.CO;2.

Vinoj, V., P. J. Rasch, H. Wang, J.-H. Yoon, P.-L. Ma, K. Landu, and B. Singh (2014), Short-term modulation of Indian summer monsoon rainfall by West Asian dust, *Nat. Geosci.*, *7*(4), 308–313, doi:10.1038/ngeo2107.

Wang, K., and C. Liu (2014), Transport of the Saharan dust air plumes over the tropical North Atlantic from FORMOSAT–3/COSMIC observation, *Atmospheric Pollut. Res.*, *5*(3), 539–553, doi:10.5094/APR.2014.063.

Wong, S., and A. E. Dessler (2005), Suppression of deep convection over the tropical North Atlantic by the Saharan Air Layer, *Geophys. Res. Lett.*, *32*(9), L09808, doi:10.1029/2004GL022295.

Wong, S., A. E. Dessler, N. M. Mahowald, P. Yang, and Q. Feng (2009), Maintenance of Lower Tropospheric Temperature Inversion in the Saharan Air Layer by Dust and Dry Anomaly, *J. Clim.*, *22*, 5149–5162, doi:10.1175/2009JCLI2847.1.

Woodward, S. (2001), Modeling the atmospheric life cycle and radiative impact of mineral dust in the Hadley Centre climate model, *J. Geophys. Res. Atmospheres*, *106*(D16), 18155–18166, doi:10.1029/2000JD900795.

Wurzler, S., T. G. Reisin, and Z. Levin (2000), Modification of mineral dust particles by cloud processing and subsequent effects on drop size distributions, *J. Geophys. Res. Atmospheres*, *105*(D4), 4501–4512, doi:10.1029/1999JD900980.

Xue, H., G. Feingold, and B. Stevens (2008), Aerosol Effects on Clouds, Precipitation, and the Organization of Shallow Cumulus Convection, *J. Atmospheric Sci.*, *65*(2), 392–406, doi:10.1175/2007JAS2428.1.

Zhang, J., and S. A. Christopher (2003), Longwave radiative forcing of Saharan dust aerosols estimated from MODIS, MISR, and CERES observations on Terra, *Geophys. Res. Lett.*, *30*(23), 2188, doi:10.1029/2003GL018479.

Zhao, C., X. Liu, L. R. Leung, B. Johnson, S. A. McFarlane, W. I. Gustafson Jr., J. D. Fast, and R. Easter (2010), The spatial distribution of mineral dust and its shortwave radiative forcing over North Africa: modeling sensitivities to dust emissions and aerosol size treatments, *Atmos Chem Phys*, *10*(18), 8821–8838, doi:10.5194/acp-10-8821-2010.

Zhao, C., S. Chen, L. R. Leung, Y. Qian, J. F. Kok, R. A. Zaveri, and J. Huang (2013), Uncertainty in modeling dust mass balance and radiative forcing from size parameterization, *Atmospheric Chem. Phys.*, *13*(21), doi:10.5194/acp-13-10733-2013.

Zhou, X., N. Bei, H. Liu, J. Cao, L. Xing, W. Lei, L. T. Molina, and G. Li (2017), Aerosol effects on the development of cumulus clouds over the Tibetan Plateau, *Atmos Chem Phys*, *17*(12), 7423–7434, doi:10.5194/acp-17-7423-2017.

Zhu, A., V. Ramanathan, F. Li, and D. Kim (2007), Dust plumes over the Pacific, Indian, and Atlantic oceans: Climatology and radiative impact, *J. Geophys. Res. Atmospheres*, *112*(D16), D16208, doi:10.1029/2007JD008427.